THE EFFECT OF GEOTHERMAL HEAT PUMPS ON SUBSURFACE FLOW AND CONTAMINANT TRANSPORT

IMAN ROOHIDEHKORDI

A THESIS SUBMITTED TO THE FACULTY OF GRADUATE STUDIES IN PARTIAL FULFILLMENT OF THE REQUIREMENTS FOR THE DEGREE OF MASTER OF APPLIED SCIENCE

GRADUATE PROGRAM IN CIVIL ENGINEERING

YORK UNIVERSITY

TORONTO, ONTARIO

JUNE 2020

Abstract

Geothermal or ground source heat pumps (GSHPs) are among the growing renewable energy technologies used for heating and cooling of buildings. However, little work has been done to investigate their geo-environmental effects within the subsurface. This research uses FEFLOW software, to simulate heat and mass transport for a vertical closed-loop GSHP system. Steady and transient flow and heat transport results for a multiple borehole system are presented which indicate long-term effects on ground temperature. Moreover, the impact of heat exchanged with the subsurface on contaminant transport and biodegradation processes is studied to evaluate the possibility of utilizing this heat as a remediation strategy. The results reveal that temperature changes caused by GSHP operation can significantly enhance biodegradation of hydrocarbon contaminants. For instance, elevated subsurface temperature resulted in 96% reduction in benzene concentration, from 0.306 to 0.011 $mg.L^{-1}$, after one year of GSHP operation for an office building in Toronto.

Keywords: Ground source heat pumps, Heat and contaminant transport in porous medium, Groundwater bioremediation, biodegradation kinetics, FEFLOW simulation

Dedication

With special thanks to all my family members for their support, I dedicate this thesis to my beloved wife, Arezoo Khalili. Without her help, care and understanding during the past two years, it would not possible for me to complete this chapter of my life.

Acknowledgments

First, I would like to express my gratitude to my academic advisor, Dr. Magdalena Krol, for her insights, supports, patience and understanding during my graduate studies. Beside my advisor, I am very grateful to my thesis committee members, Dr. Matthew Perras and Dr. Satinder Brar for their help and contribution to my achievement.

Secondly, I would like to thank my parents for their love, encouragement and unwavering support through my whole life.

Moreover, I would like to thank my in-laws for their help, enthusiasm, encouragement and morale support.

Last, but not least, I express my gratitude to the Natural Science and Engineering Research Council of Canada (NSERC) which supported this research through Discovery Grant.

Table of Contents

List of Tables

List of Figures

Nomenclature

Symbols

α_L	longitudinal thermodispersivity
α_T	transverse thermodispersivity
β	thermal expansion coefficient
β_L	longitudinal dispersivity
β_T	transverse dispersivity
Δ	nodal distance in the immediate vicinity of the borehole
Λ	thermal hydrodynamic dispersion tensor
ε	Porosity or volume fraction
λ	thermal conductivity
μ	microbial growth rate
μ_m	maximum specific growth rate
ρ	density
ρ_b	Bulk density
ϑ	first-order decay rate constant
χ	sorption isotherm
b	microbial decay rate
B_c	biomass concentration
C	building heating and cooling loads
C	Concentration of the dissolved species
C^s	Sorbed mass

D	hydrodynamic dispersion tensor
D_d	diffusion coefficient
D_b	Borehole depth
E_a	activation energy for cell growth
E_b	activation energy for thermal denaturation processes
f_μ	viscosity dependency to temperature
f_{oc}	soil organic carbon content
G	ground thermal load
h	Hydraulic head
H	building heating load
H_e	thermal sink/source
i	Hydraulic gradient
k	dimensionless sorption coefficient
k_d	distribution coefficient
k_{oc}	organic carbon partition coefficient
k_s	half saturation constant
K	hydraulic conductivity tensor
M	total contaminant mass
q	Darcy flux vector
q_b	specific heat extraction rate
Q	general source/sink function
Q_d	non-reactive bulk production rate
Q_{gr}	ground load

Q_r	Refrigerant flowrate
Q_{EOB}	extended Oberbeck-Boussinesq function
r_b	borehole physical radius
r_{hom}^f	fluid phase homogeneous reaction rate
r_{hom}^s	solid phase homogeneous reaction rate
R	retardation factor
R_u	universal gas constant
S	concentration of the substrate
S_s	specific storage coefficient
S_w	solubility
T	Absolute temperature
$v_{\max}$	maximum substrate utilization rate
v	seepage velocity
Y	biomass yield

Subscripts

0	reference value
b	borehole
C	cooling
H	heating
i	inlet
o	outlet
r	refrigerant

w	water

Superscripts

f	fluid
g	grout
r	refrigerant
s	solid

Abbreviations

1U	single U-tube
2U	double U-tube
ASHP	Air-Sourced Heat Pump
ASHRAE	American Society of Heating, Refrigerating and Air-conditioning Engineers
ATES	Aquifer Thermal Energy Storage
BHE	Borehole Heat Exchanger
BTES	Borehole Thermal Energy Storage
BTEX	Benzene, Toluene, Ethylbenzene and Xylene
COP	Coefficient Of Performance
CXA	Coaxial with Annular inlet tube
CXC	Coaxial with Centered inlet tube
DOC	Dissolved Organic Carbon
ERH	Electrical Resistance Heating
FD3DM	Fully Discretized 3D Model

FEM	Finite Element Method
GCHP	Ground Coupled Heat Pump
GSHP	Ground-Sourced Heat Pump
GWHP	Ground Water Heat Pump
HDPE	high-density polyethylene
HVAC	Heating, Ventilation and Air Conditioning
MBGS	Meter Below Ground Surface
NAPL	Non-Aqueous Phase Liquid
ORC	Organic Rankine Cycle
SCW	Standing Column Well
SWHP	Surface Water Heat Pump
TAZ	Thermal Affected Zone
TRCM	Thermal Resistance and Capacity Model
TRT	Thermal Response Test
VOC	Volatile Organic Compound

Chapter 1 - Introduction

Despite the widespread use of fossil fuels during the past century, energy framework is experiencing a gradual shift toward more energy conserving strategies due to the decline in availability and reliability of fossil fuels and their increasing costs. Environmental concerns like global warming and air pollution are also contributing to this paradigm shift (Self et al., 2013).

It is estimated that about 40% of world total energy consumption is dedicated to lighting, heating, cooling and air conditioning in the building sector (Lucia et al., 2017). Moreover, energy required for cooling and heating generally accounts for 40–60% of total building energy consumption (Yuan et al., 2017). This leads to utilization of about 20% of world total energy solely for heating and cooling which represents a considerable potential for energy saving if more efficient heating/cooling methods are employed. Using geothermal energy to heat and cool buildings is a promising way to increase the use of renewable energy in the building sector. Geothermal or ground source heat pumps (GSHPs) are among the top growing energy technologies used for heating and cooling from shallow geothermal energy sources (Lund & Boyd, 2016), and have the ability to be extensively implemented worldwide.

Moreover, with more than 30,000 brownfield sites in Canada requiring cleanup (De Sousa et al., 2018), rejected heat from geothermal heat pumps could be utilized as a thermal remediation strategy to remove contaminants that are susceptible to heat treatments (e.g. petroleum hydrocarbons or volatile organic compounds). However, despite being commercially used for many years, little research has been performed on the environmental impacts of geothermal heating, especially their potential for enhanced remediation. Therefore, evaluation of the effect of heat extracted or stored in the subsurface on groundwater flow and contaminants transport is valuable information in utilization and optimization of geothermal heating systems as a possible remediation strategy.

1.1. Geothermal heat pumps

Geothermal energy is often categorized according to application and temperature range as follows (Self et al., 2013):

1. High temperature (deep geothermal) for electricity generation purpose through steam.
2. Intermediate temperature for direct heating.
3. Low temperature (shallow geothermal) for indirect heating and cooling by a heat pump, where *low temperature* generally means less than 30°C and *shallow* means less than 200 mbgs.

However, the term *geothermal energy* is used to refer to the high and intermediate temperature energy utilized from deep subsurface, while the relatively new term *thermogeology* represents the study of low temperature heat in relatively shallow geosphere specially for heating, ventilating, and air conditioning (HVAC) applications (Banks, 2012). This ground source heating/cooling which is the focus of this research, is becoming more inviting because unlike high and intermediate temperature geothermal energy, it is accessible almost everywhere and can be implemented worldwide.

Geothermal energy can be utilized in different ways such as geothermal heat pumps, direct space heating, agricultural drying, greenhouse heating and swimming pools and baths application. In Figure 1.1, geothermal worldwide utilization ($TJ.yr^{-1}$) in 2015 is depicted. As seen in Figure 1.1, heat pump applications account for about 55% of worldwide utilization of geothermal energy (Lund & Boyd, 2016).

More importantly, Figure 1.2 presents a comparison of worldwide heating-use of geothermal energy in different applications from 1995 until 2015. The graph reveals a significant rise in utilization of geothermal heat pumps starting at about 15,000 ($TJ.yr^{-1}$) in 1995 and reaching 325,000 ($TJ.yr^{-1}$) at the end of a 20-year period in 2015. The increasing usage of geothermal heat pumps indicates a promising market for this type of sustainable energy generation.

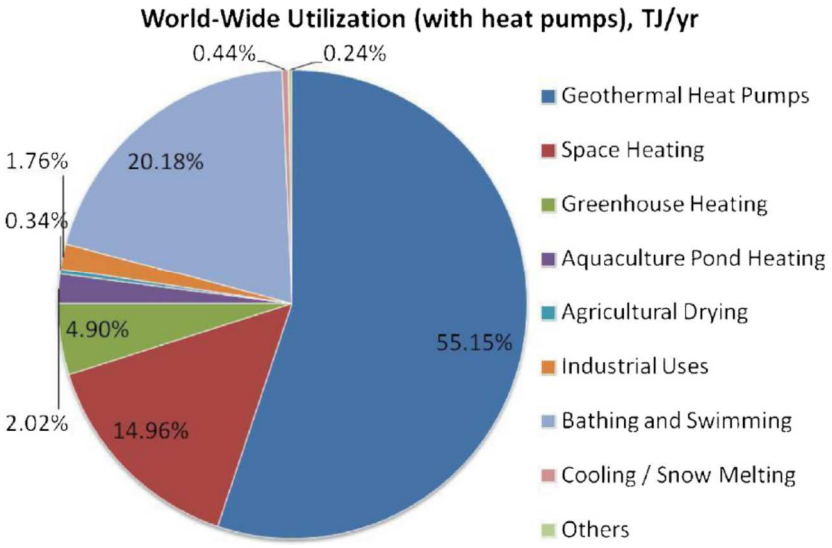

Figure 1.1. Use of geothermal energy worldwide in 2015 (Lund & Boyd, 2016)

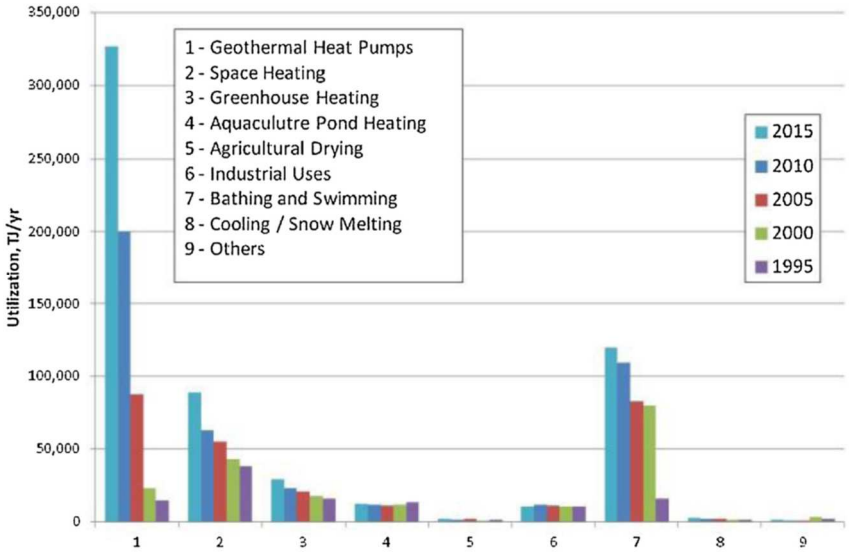

Figure 1.2. Comparison of worldwide heating-use geothermal energy in different applications (Lund & Boyd, 2016)

Two factors contribute to ground source heat: (1) solar energy absorbed and stored by earth surface and (2) heat flux from earth crust resulted mostly from decay of radioactive nuclides like uranium, potassium and thorium (Banks, 2012). While solar radiation changes and seasonal temperature fluctuations impact surface temperature, it only penetrates a few meters into the ground. Therefore, below a few meters, ground temperatures are almost independent of the

seasonal air temperature fluctuations as shown in Figure 1.3 for Ottawa, Canada (Self et al., 2013). This depth varies in different places, but it is reported to be less than 20m below surface all-over Canada (Majorowicz et al., 2009). This characteristic of subsurface is related to high *thermal storage* and relatively modest *thermal conductivity* of silicate-based ground. The latter is responsible for movement of stored heat and high values would result in immediate dissipation of the heat to unreachable depths, while low values could lead to difficulties in extracting heat via designed heat exchangers. This constant temperature leads to the concept of ground as heat source/sink in a heat pump system.

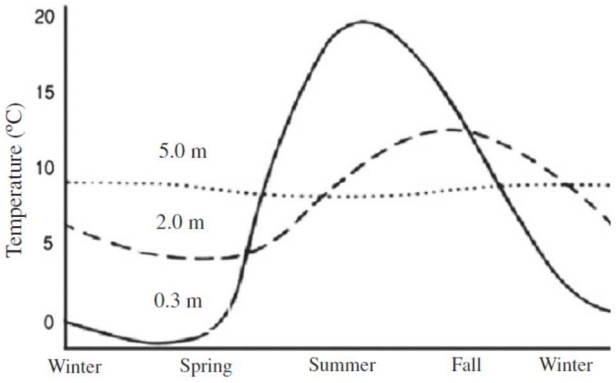

Figure 1.3. Variation of ground temperature at different depths in Ottawa, Canada (Self et al., 2013)

A heat pump is a device that uses a ground loop system to absorb heat from a colder environment and transfer it to a warmer space by applying external work with a compressor, thus keeping the warmer space heated (see Figure 1.4). Alternatively, this cycle can be reversed allowing for absorbing of heat from a space (e.g. building) and subsequently rejecting it to the environment. This is referred to as the cooling mode. Therefore, dual mode utilization of a single heat pump is possible by using a simple 4-way reversing valve, which controls the direction of refrigerant flow in the summer and winter seasons, which swaps the evaporator and condenser heat exchanger roles.

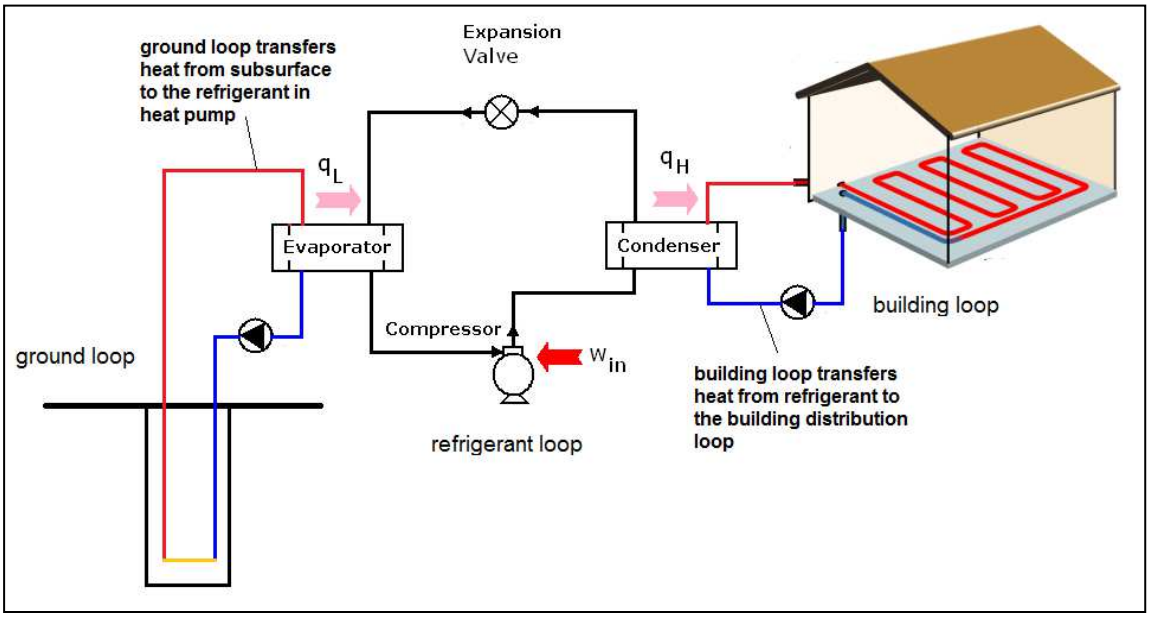

Figure 1.4. Schematic diagram of a GSHP used for space heating

Conventionally, heat pumps use outside air as source/sink and are called air source heat pumps (ASHPs). However, since the temperature of the ground is higher than ambient air in winter, and lower than air in summer, implementation of ground source heat pumps (GSHPs) is more efficient using the subsurface as the heat source/sink (Staffell et al., 2012).

Figure 1.5 represents the comparison between ASHP and GSHP coefficient of performance (COP) as the efficiency indicator for heat pumps. COP is defined as the ratio of extracted or rejected heat to the consumed work. As can be seen by Figure 1.5, COP varies with temperature difference between the building and ground loops. By assuming 40°C as the temperature required for space heating and 10°C as temperature within ground (i.e. temperature difference of 30°C), the ASHP COP is around 3.5 while a COP of 5 could be achieved for GSHP. Both concepts are more effective than conventional methods such as electric heaters or fuel powered boilers with COP of less than 1 (Staffell et al., 2012).

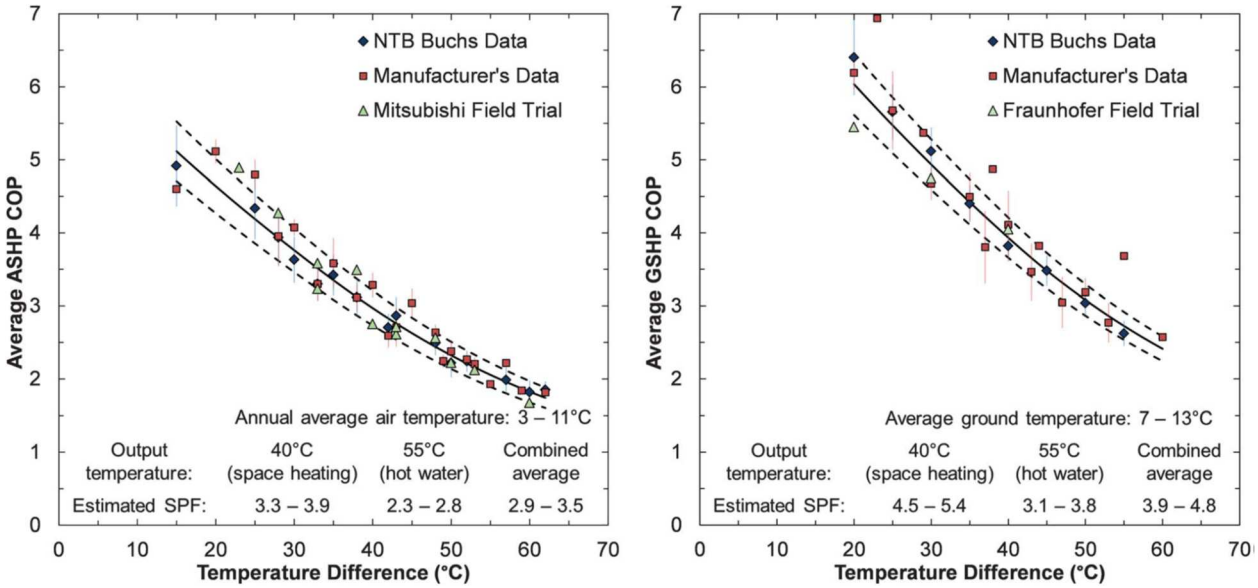

Figure 1.5. A comparison between ASHP and GSHP coefficient of performance (COP) (Staffell et al., 2012)

1.2. Geothermal heat pump types

Geothermal heat pumps can be divided in two main categories as open-loop and closed-loop systems. In open-loop systems, groundwater is pumped from wells, drilled boreholes or flooded mines and its thermal energy is extracted and transferred to the space for heating purpose. Subsequently, the water is injected to the ground (see Figure 1.6). In cooling mode, heat from the space is absorbed by the groundwater, causing water temperature to rise. This system is also known as a groundwater heat pump (GWHP).

A related category to GWHP is called geothermal standing column well (SCW) in which the extracted water is re-injected to the same abstraction well (see Figure 1.7). Note that it takes some time for the cooled re-injected water to be mixed with new groundwater entering the well and to equilibrate with groundwater temperature. As a result, SCW wells need deeper drilling up to 450 m and therefore have significant installation costs (Lucia et al., 2017).

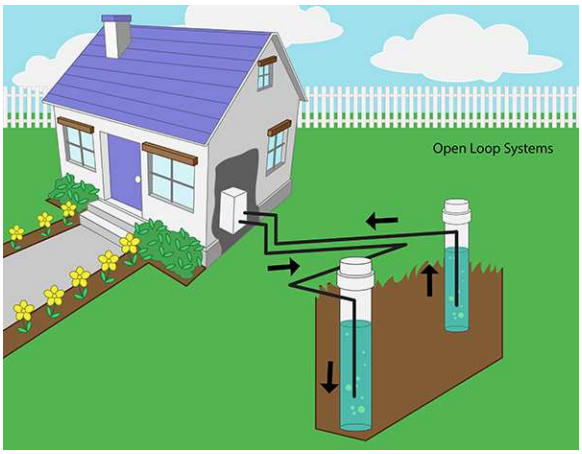

Figure 1.6. Schematic diagram of an open-loop groundwater heat pump (*Remodeling Calculator*, 2020)

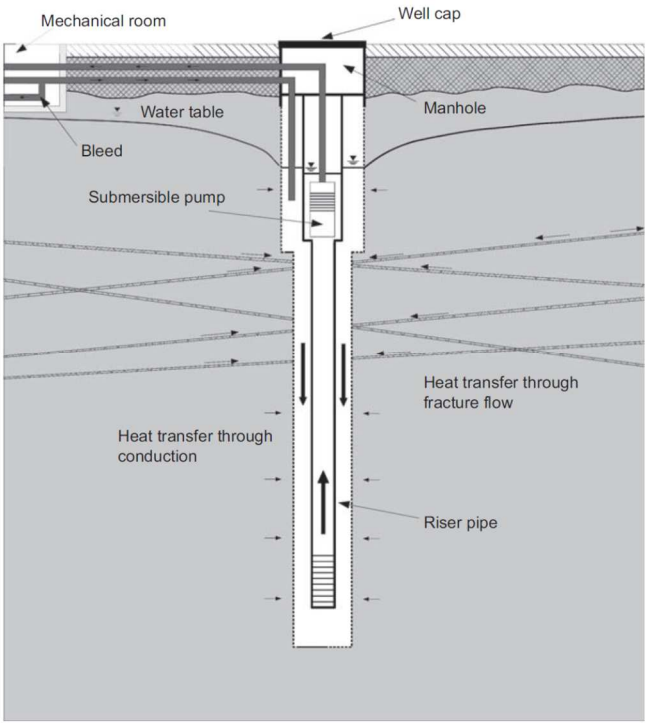

Figure 1.7. Schematic diagram of standing column well (SCW) heat pump (Rees, 2016)

In general, open-loop systems are considered to have higher efficiency (Lucia et al., 2017). The fact that open-loop systems use forced convection, in contrast to closed-loop systems which utilize conduction or natural convection, dictates that they transfer more heat per unit area of dug well or borehole. The main drawback of an open-loop GWHP system is its dependence to the

existence of an aquifer with proper yield of water flux (Banks, 2012). Water chemistry and quality is also important since it can lead to corrosion or fouling problem within the heat pump (Omer, 2013). Furthermore, there are some concerns about technical, legal and environmental aspects of disposal of used water such as:

- If wastewater is supposed to dispose to sewer, it should be permitted by utility management to ensure system has the capacity to accept the waste flow.
- In case of disposal to surface water like ponds or rivers, compatibility of the wastewater with surface water ecology should be analyzed to ensure that temperature difference or chemical composition of the wastewater would not jeopardize the ecosystem.
- In case of re-injection to the abstracted aquifer, it should be dumped in proper distance to the abstraction well to avoid *short circuiting*.

Closed-loop systems rely on heat transfer with ground without the need for extraction and re-injection of groundwater and thus they can be built almost everywhere. In this scheme which is also known as ground-coupled heat pump (GCHP), a carrier fluid is sent to the ground via tubes installed in boreholes or trenches to absorb thermal energy and then it is circulated back to the surface to release the heat. Main categories of closed-loop systems are:

1. Horizontal
2. Pond/lake loops
3. Vertical

Horizontal closed loops are the simplest and cheapest technology and are installed in shallow trenches at 1 to 2 meters depth. The low depth is selected to achieve sufficient thermal storage capacity and adequate soil moisture while protecting piping system from freezing. Low depth installation also helps the ground to absorb solar and atmospheric heat in summer thus enhancing the potential to harvest thermal energy. To reduce the area needed for installation of a long piping system, tubes can be coiled to shape a *Slinky* (see Figure 1.8). The main problem associated with horizontal GCHPs is that air temperature changes during cold season affect

shallow installations and loop temperature fluctuations occur accordingly. As a result, they might experience a less stable heat source and a decline in system COP (Lucia et al., 2017).

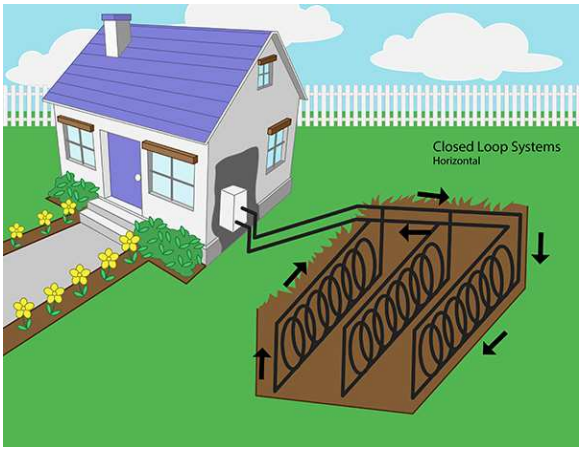

Figure 1.8. Schematic diagram of a horizontal closed-loop heat pump (*Remodeling Calculator*, 2020)

In case there is a pond or lake, heat exchanger coils can be submerged in water to exploit higher heat transfer coefficients of water compared to soil (see Figure 1.9). This scheme is also referred to as surface water heat pump (SWHP) and the main environmental concern about that is water source should be large enough (ideally with at least 3 m depth) so that the extracted or injected heat does not affect its temperature. This is due to the sensitivity of the ecosystem to the temperature and level of dissolved oxygen in the water (Banks, 2012).

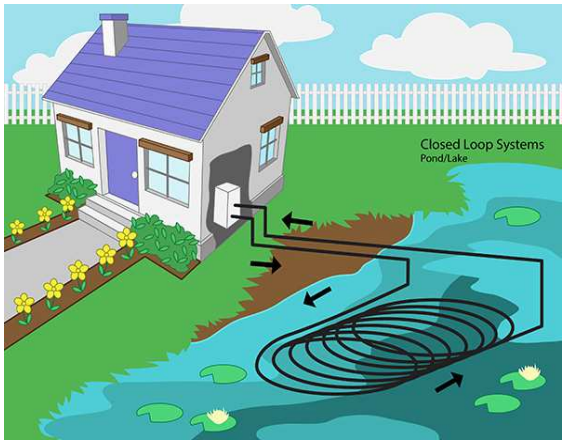

Figure 1.9. Schematic diagram of a pond/lake type closed-loop heat pump (*Remodeling Calculator*, 2020)

Vertical closed loops as shown in Figure 1.10, are alternative of horizontal schemes in case the available area is limited. In this scenario, a vertical borehole is drilled to the ground and the upper section is supported with casing to prevent surface contamination entering the subsurface. The needed depth of borehole is proportional to the heating/cooling load required while deeper drillings demand more costs (Banks, 2012)

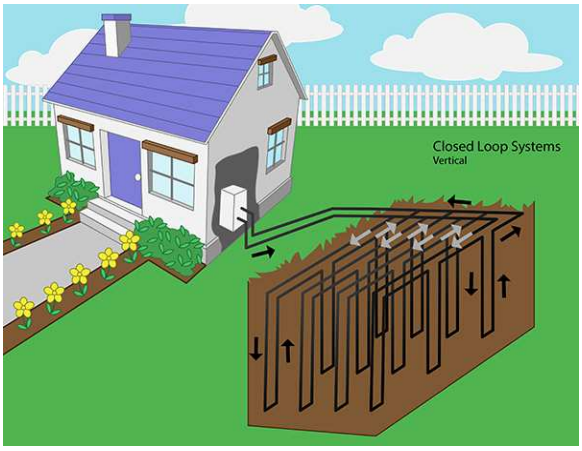

Figure 1.10. Schematic diagram of a vertical closed-loop heat pump (*Remodeling Calculator*, 2020)

1.3. Cost considerations

Although geothermal heat pumps are better in terms of efficiency and pollution emission, the main drawback is their higher installations costs (Raymond et al., 2010). The cost heavily depends on capacity and type of the geothermal heat pump system as shown in Figure 1.11. Open-loop systems are preferred for capacities above 100 kW. Horizontal (or slinky) closed-loop systems have the lowest cost but they are limited to around30 kW because they require vast surface area. Closed-loop borehole systems are competitive for medium to large capacity installations (above 50 kW) and they are the most widely used shallow geothermal systems for this range (Banks, 2008).

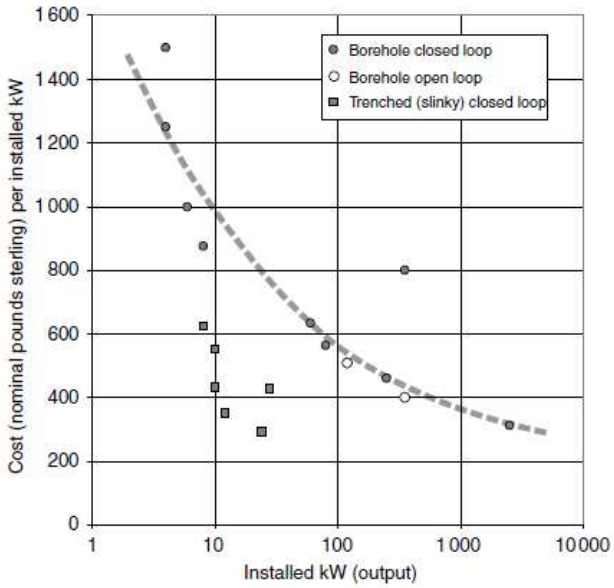

Figure 1.11. Capital cost per installed kW of different types of geothermal heat pumps (Banks, 2008)

1.4. Multiple borehole heat exchanger (BHE) systems

For closed-loop borehole systems, common heat absorption rate from the ground per drilled meter is 35-73 $W.m^{-1}$ (Banks, 2012). Since the depth of boreholes is limited to about 200 m, average capacity of a single borehole is around 10 kW. However, at this low capacity, a single borehole is not economically feasible. Thereby, multiple borehole systems are considered as the most prevailing shallow geothermal energy concept, which in turn leads to concerns about layout and spacing of boreholes (Dehkordi et al., 2015).

With the added complexity of having multiple boreholes, the importance of flow and transport modeling for designing a geothermal heat pump system is enhanced due the fact that thermal interference between boreholes could lead to loss of efficiency since some boreholes experience non-uniform temperature changes. To alleviate the thermal interference, borehole spacing and arrangement should be considered. Spacing of the boreholes has a bigger impact on thermal interference Even though a minimum distance of 10 m is proposed to decouple the borehole heat exchangers, different groundwater flow velocity, soil porosity or heat demands might render this

preliminary distance value ineffective. In addition, layout and arrangement is another factor that can diminish thermal interference between boreholes. It is shown that rectangular layout reduces negative effects compared to in-line arrangement where groundwater flow is parallel to the axis that connects the boreholes (Dehkordi et al., 2015).

1.5. Domestic hot water challenge

Sometimes, GSHPs can be used to also heat domestic hot water which poses some challenges. In order to heat a space, a warm water at temperatures of up to 50°C is sufficient which is common for a ground source heat pump. Reaching higher temperatures with a GSHP is possible but at the cost of reduced efficiency. Domestic hot water (DHW) for kitchen and bathroom use is, however, regulated to be stored at least at 60°C because of the risk of Legionnaires' disease, caused by the proliferation of Legionella bacteria in warm (20–45°C) water systems (Banks, 2012). Therefore, extracting domestic hot water from a GSHP requires some additional arrangements such as:

- Desuperheater heat exchanger
- Two-stage approach
- Preheating DHW

A desuperheater is a heat exchanger that takes heat from the hot refrigerant gas after it leaves the compressor and transfers it to the produced warm water to further elevates its temperature (see Figure 1.12). The scheme is effective only if the amount of needed DHW is not significant.

In a two-stage approach, the main GSHP transfers heat from ground loop to building loop at say, 45°C, while a second and yet small capacity heat pump absorbs heat from building loop at 45°C and deliver it to DHW circuit at 60°C (see Figure 1.13). It should be noted that in the second heat pump cycle, the appropriate refrigerant selection is required to be compatible with relatively high temperature in the evaporator.

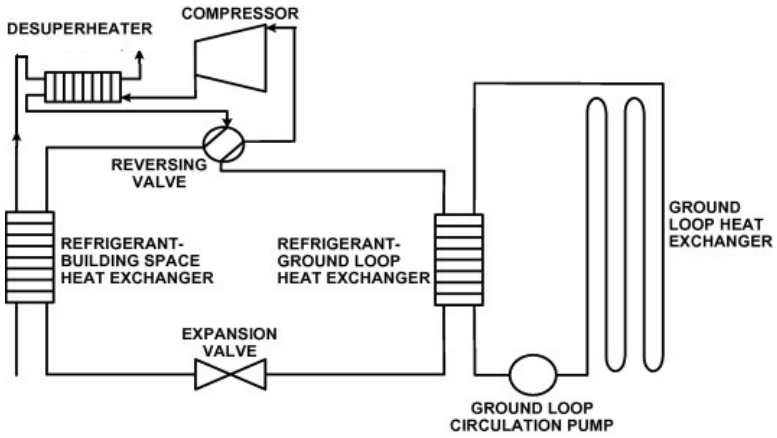

Figure 1.12. Schematic diagram of a GSHP with despuerheater heat exchanger (Self et al., 2013)

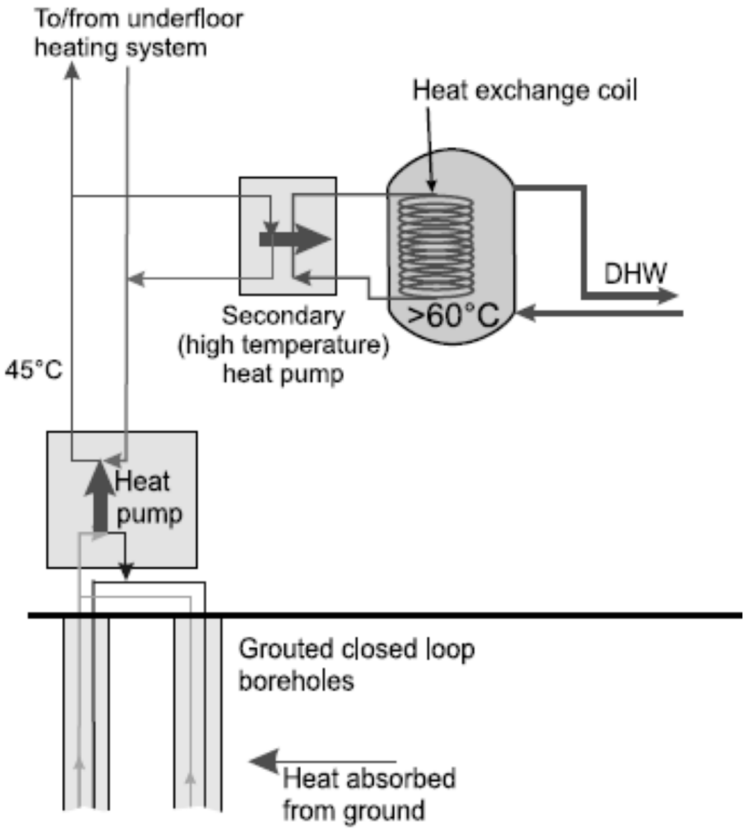

Figure 1.13. Schematic diagram of a two stage GSHP (Banks, 2012)

Finally, in a preheating DHW scheme, warm water at 45°C is extracted from heat pump's building loop and sent to a conventional water heater such as an electric heater or a gas boiler to further raise the temperature to 60°C (see Figure 1.14). Although in this plan auxiliary heating from

conventional sources is needed, advantage of utilizing ground source energy for preheating DHW is still available.

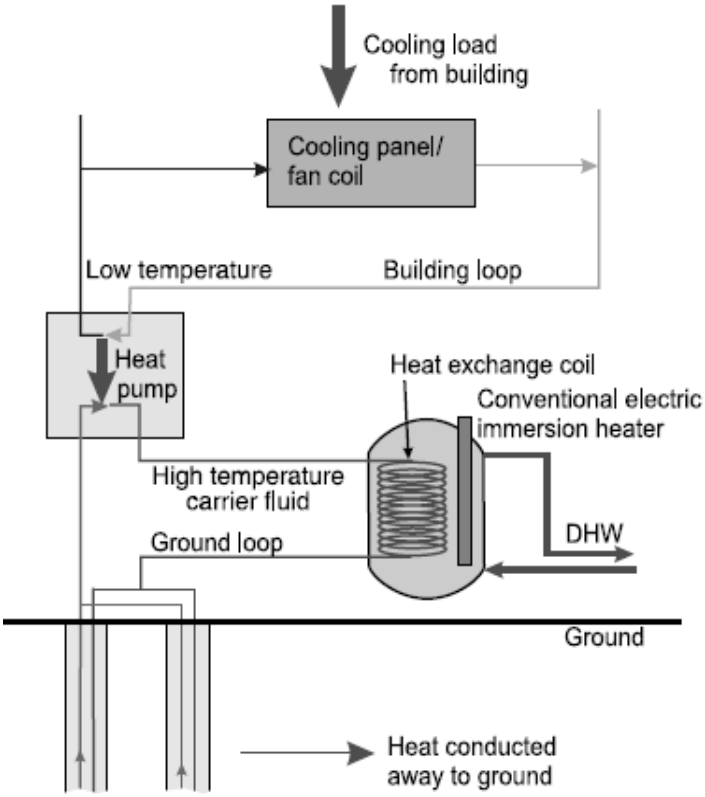

Figure 1.14. Schematic diagram of preheating DHW from ground source heat (Banks, 2012)

1.6. Thermal and environmental aspects

Heating and cooling loads of a building are not necessarily balanced. Although climate has an undeniable role, the heating demand in residential buildings often exceeds the cooling load, whereas most of the commercial and institutional buildings are cooling dominated due to respiration and equipment heat loads (Cory et al., 2011). In a heating dominated building, heat extracted for heating purpose in winter is more than the heat injected into the ground in summer, thus allowing for a gradual decline in ground temperature. In a cooling dominated building, however, the ground temperature starts to rise.

Operation of geothermal heat pumps transferring heat with the subsurface, disturbs ground temperature in the vicinity of the boreholes and temperature isolines around the boreholes, called thermal plumes or thermal fronts, are formed (Dehkordi and Schincariol, 2014; Tolooiyan and Hemmingway, 2014; Daemi and Krol, 2019). For unbalanced load scenarios, the situation greatly intensifies. Therefore, a significant change in subsurface temperature might occur even with a modest groundwater flow and the thermal plume moving in downgradient, might interfere with other boreholes. Hence, some boreholes might experience efficiency loss in lifetime operation (Dehkordi et al., 2015). The resulting plume might travel far and even effect neighboring facilities.

In addition to thermodynamic impacts, there are long-term environmental consequences associated with thermal plume spread and soil temperature changes. For instance, if a thermal front reaches the capture zone of a groundwater well, the impacted reaction kinetics might change the chemistry and quality of water or even cause well clogging which must be avoided (Bonte, 2013).

Additionally, there are microbiological impacts of changes in soil temperature due to the microbial temperature preference, since various microorganisms need different temperatures to proliferate and grow. As can be seen in Figure 1.15, there are 4 types of microorganisms as psychrophiles (with temperature preference range of 0 to 20°C), mesophiles (with temperature preference range of 15 to 45°C), thermophiles (with temperature preference range of 45 to 80°C) and hyperthermophiles (Parker et al., 2016). Therefore, a more favorable temperature for a certain microorganism responsible for biodegradation of a contaminant might enhance bioremediation process and vice versa (Beyer et al., 2016; Bonte et al., 2013).

Furthermore, elevated subsurface temperature resulting from heat injection from a heat pump, can have various impacts on chemical properties. For example, temperature increases the solubility of non-aqueous phase liquids (NAPLs), can decrease hydrocarbon sorption and increase

diffusion of various compounds. These changes can lead to spread of the contamination but can also make contaminants more susceptible to biodegradation (Beyer et al., 2016; Hiller et al., 2008). Temperature rise also can change the prevailing electron acceptor in a reduction process, i.e., shifting iron reducing to sulfate reducing or methanogenic conditions. Lastly, it has claimed that methanogenic conditions can promote reductive dechlorination of contaminants like PCE (Bonte et al., 2013).

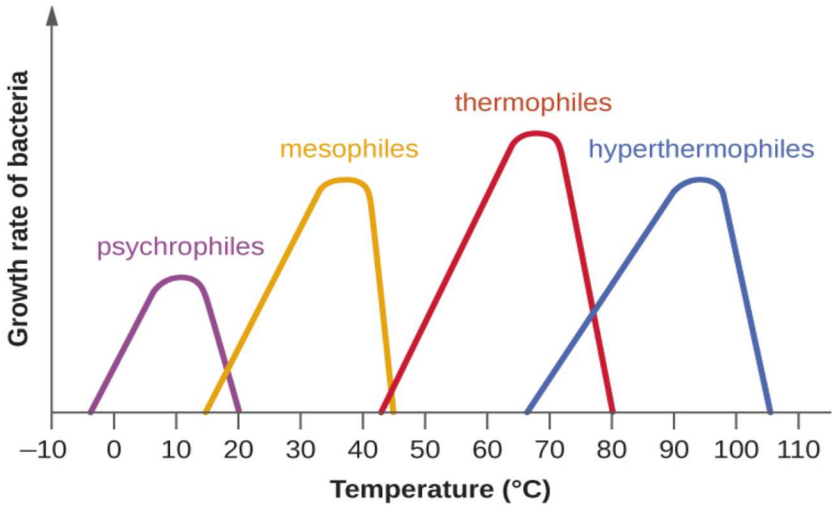

Figure 1.15. Growth rate for different bacteria as function of temperature (Parker et al., 2016)

1.7. Thesis objectives

In this chapter, geothermal heat pump systems are briefly described in terms of different types, advantages and drawbacks, potential and cost, and an introduction to thermal plume spread and environmental aspects is given. Closed loop GHSPs are the most common technology in geothermal heating application, however, little work has been done on the possible impacts of thermal loads on contaminants' fate and transport, especially its potential for bioremediation of hydrocarbon contaminants in urban areas.

Main objectives of this research are as follows:

1. Development, validation and verification of a vertical closed-loop geothermal heat pump model using FEFLOW software.
2. Study of long-term effects of geothermal heat pumps on ground temperature and development of thermal plumes in the subsurface, based on a 3-storey building located in Toronto, Canada.
3. Investigation of the impact of temperature changes resulting from geothermal heating on contaminants' fate and transport through temperature-dependent sorption and biodegradation.

Implementation of these objectives would lead to the evaluation of the effect of heat extracted or stored in subsurface on groundwater flow and contaminant transport which is valuable in utilization and optimization of sustainable geothermal heating systems as a possible remediation strategy.

Chapter 2 is dedicated to a literature review on GSHPs and borehole heat exchangers with emphasis on numerical modeling in FEFLOW, effect of load imbalance and thermal plume development, environmental impacts of geothermal heating, and the effect of temperature on biodegradation and sorption. In chapter 3, model development, validation and verification in FEFLOW is presented (Objective 1). In this regard, governing equations are introduced and effect of heat on flow and contaminant transport is described in terms of change in various parameters like density and viscosity, solubility, sorption and biodegradation kinetics which leads to deriving temperature-dependent parameters used in contaminant transport modeling. Chapter 4 present results and discussion (Objectives 2 and 3). Finally, summary and conclusions are presented in chapter 5.

Chapter 2 - Literature review

Since the beginning of open-loop ground water heat pump systems (GWHPs) in late 1940s and closed-loop ground coupled heat pumps (GCHPs) in 1970s, a lot of advancement has been made to the technologies (Soltani et al., 2019). This chapter gives an overview of the technologies and describes background studies, with the emphasis on vertical closed loop systems coupled with borehole heat exchangers (BHEs). Thermal, chemical and microbiological impacts of geothermal heat pumps are explained and some important challenges like load imbalance and thermal plumes are outlined. Moreover, governing equations for fluid flow and heat and mass transport within porous media in FEFLOW are described. Finally, microorganisms capable of petroleum hydrocarbon biodegradation are introduced along with a literature review on the effect of temperature on microbial growth, biodegradation, reaction kinetics and sorption.

2.1. Geothermal heat pumps and subsurface interactions

Due to the maturity of the geothermal heat pump technology, there have been much research done on different aspects of the technology ranging from various analytical and numerical modeling techniques, application of computational software codes, impact of hydrogeological parameters, thermo-economic analysis and the effect of building load on the environment.

Effect of ground stratification on ground temperature distribution is one of the aspects which has been investigated by numerical models with variable and constant heat transfer rates in borehole's axial direction (Wenxin Li et al., 2019). The results demonstrated that constant heat transfer rate assumption imposes remarkable error in prediction of ground temperatures within a layered ground.

The importance of ground thermo-physical parameters on design and planning of GSHPs is discussed in the work of Luo et al., (2016). They have estimated heat transfer rates for different geological setting and their results show that saturated gravel or sand generally yield more heat

than other unconsolidated materials or different rock types. The heat extraction rate is reported in the range of 55-65 $W.m^{-1}$ for saturated sand and 80-100 $W.m^{-1}$ for sand in the presence of strong groundwater flows. Obtaining correlation between geological parameters and conductive heat transfer rates for smaller designs in which financial feasibility restricts expensive tests is a common practice. To achieve more accurate results in larger projects, however, the ground thermal conductivity is commonly measured by laboratory or field tests.

For optimized planning of shallow geothermal heating, Schelenz et al., (2017) studied the advantages of accurate site-specific characterization compared to desktop-based approach for a residential area with 53 single family houses in the city of Taucha, Germany. Here, site-specific characterization implies achieving hydrogeological data by minimally invasive ground exploration tests whereas desktop-based approach refers to derivation of important hydrogeological parameters such as thermal and hydraulic conductivities, heat capacity, and porosity from available general geological maps which usually leads to a range in selection. Their study showed the potential for a moderate saving in total cost of GSHP with utilization of site-specific characterization.

Owing to high initial capital costs of vertical closed-loop GSHPs, techno-economic analysis of such systems is another area that caught the attention of some researchers. Blum et al., (2011) studied more than 1100 small scale heat pumps (less than 30 kW) for correlation among parameters like depth and length of boreholes, heat loads, heated areas and capital costs of GSHPs. They reported the mean capital cost for an average GSHP system for a single household with 11 ± 3 kW heat demand as 23,500 ± 6800 € (equal to 35000 ± 10000 CDN$), in which borehole drilling cost and heat pump price contribution to the total cost is almost 50%. The distribution of the data, however, showed a weak fit between capital costs and heat demands, which indicates uncertainty in cost prediction.

Using geothermal heating for sustainable development in both energy production and urban development by brownfield utilization is another aspect which has drawn attention. Donaldson

and Lord, (2018) considered potentials of using geothermal heat pumps and other renewable sources for redevelopment of brownfields in Glasgow, Scotland to overcome fuel poverty problem. Their results showed potential energy harvesting rates for vertical and horizontal GSHPs as 56 $W.m^{-2}$ and 15 $W.m^{-2}$, respectively, which is slightly higher than 50 $W.m^{-2}$ and 11 $W.m^{-2}$ for solar heating and solar photovoltaic schemes. Based on these values, they claimed that implementation of horizontal GSHPs, as the worst-case scenario, could compensate for 47% of the cases prone to fuel poverty in Glasgow. This study, however, neglects the environmental impact of temperature drift in the ground and potential subsurface contaminants.

Another interesting aspect with significant room for further investigation is the effect of temperature on groundwater flow and transport phenomena due to geothermal heat pump use. In the work done by Beyer et al., (2016), the effect of temperature rise due to the excess heat rejection from BHEs to the subsurface is investigated. They considered the dependency of groundwater flow, solute transport and biodegradation with temperature with the focus on chlorinated hydrocarbon contaminants like TCE in a residual non-aqueous phase liquid (NAPL) source zone. Since solubility of NAPLs increases with temperature, TCE release from source zone can cause contaminant spread. However, elevated temperatures can increase microbial activity thus allowing for better biodegradation potential. Similarly, Sommer et al., (2013) presented the results of monitoring an aquifer thermal energy storage (ATES) system build in a site in Netherlands contaminated with chlorinated hydrocarbons. They claimed that combining an ATES with in situ remediation showed promising results by means of reductive dechlorination as the prevailing degradation mechanism. They also conducted lab experiments with groundwater from contaminated ATES with introduction of dechlorinating bacteria and reached complete degradation of some chlorinated hydrocarbons. However, they proposed field tests to demonstrate the validation of their result.

The use of borehole thermal energy storage systems (BTES) as a bioremediation assisting technique in the unsaturated zone has also been studied by Moradi et al., (2018), using COMSOL Multiphysics software. They modeled boreholes as line heat source with constant temperature

of 40°C which brought the domain to the temperature range of 20-30°C, desirable for mesophilic bacteria (bioremediation phase). By achieving the remediation goal at the end of first phase, the borehole temperature was raised to 80°C for energy storage phase. Their result showed that combining borehole thermal energy storage systems with thermally enhanced bioremediation can bring the ground to the desired temperature and moisture conditions thus allowing for increase in microbial growth and activity.

2.2. Load imbalance and hybrid systems

Heat pumps can be used in dual season mode for heating and cooling by a simple 4-way reversing valve which reverses the flow of refrigerant in the system and causes the evaporator and condenser heat exchanger to switch roles and hence a single device is utilized for both heating and cooling. Since heating and cooling demands of a building are not generally equal, exchange of heat with ground can cause a thermal drift in the form of a gradual rise in ground temperature for cooling dominated cases or a decline for heating dominated buildings. The decrease in ground temperature could build up over the entire lifespan of the system especially in multiple borehole systems as shown in Figure 2.1, although it is claimed that flow of groundwater could alleviate this decrease in ground temperatures (Dehkordi et al., 2015). Utilization of the GSHP in load imbalance state, might cause issues such as:

1. excessive temperature anomalies in the ground, which in turn can lead to deviation from the design point and a gradual decrease in system COP and an increase in operation costs (Dehkordi et al., 2015). Severe ground temperature increase/decrease is called *ground fouling* because it can render the GSHP ineffective (Sagia et al., 2012).
2. excessive capital costs for the dominated load which is utilized for only a short period of time (Omer, 2013).

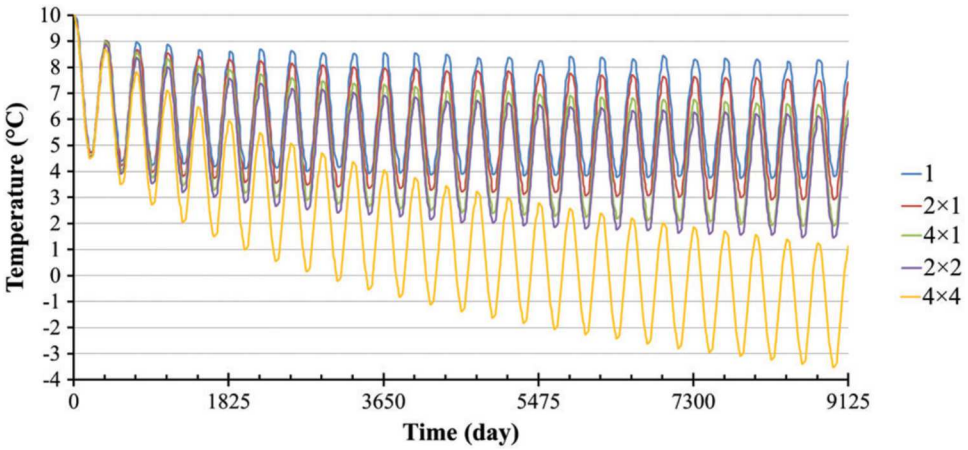

Figure 2.1. Average ground temperatures in various BHE array types under the imbalanced energy load and no groundwater over 25 years (Dehkordi et al., 2015)

The above-mentioned issues have given rise to the concept of hybrid GSHP systems. Hybrid systems incorporate supplemental flow loops and facilities, such as solar heating devices, auxiliary boilers, organic Rankine cycles (OCRs), cooling towers and dry coolers, to balance the load or reduce ground heat exchanger length (Allaerts et al., 2015; Weiyi Li et al., 2018; Sagia et al., 2012; Soltani et al., 2019; Yang et al., 2010; Yuan et al., 2017). In some applications, the excess heat that would otherwise build up in the ground may be used for domestic hot water heaters or pavement heating systems.

Figure 2.2 depicts a hybrid GSHP combined with a cooling tower for a cooling dominated office building. The GSHP is responsible for base load while the cooling tower and plate heat exchanger cover the peak load. 3-way valves are utilized to isolate supplementary cooling tower when not needed.

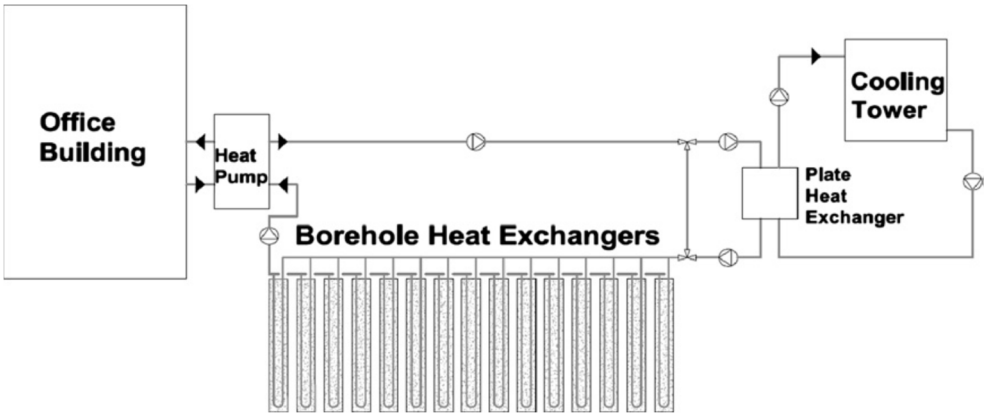

Figure 2.2. A hybrid GSHP combined with cooling tower for a cooling dominated building (Sagia et al., 2012)

Hybrid GSHPs are employed in different flow loop configurations, such as hybrid systems with serial configuration and systems with parallel arrangement depicted in Figure 2.3 (J. S. Lee et al., 2015). It is claimed that implementation of serial configuration, compared to parallel one, leads to more enhancement in heat pump's COP. Lee *et al.*, (2015) reported the COP of typical serial and parallel configurations to be 15% and 7% higher than the basic system for a cooling dominated load scenario.

Allaerts et al., (2015) studied a novel hybrid GSHP with active air-source regeneration by a dry cooler for a cooling dominated office building in Belgium, resulting from using two warm and cold borefields thus allowing for seasonal thermal energy storage. In this scenario, the heat pump extracts heat from warm borefiled in winter and the dry cooler absorbs thermal energy from the cold borefield, resulting in regenerative energy saving. In summer, however, the dry cooler absorbs heat from hot ambient and rejects it into the warm borefield. Consequently, the cold borefield could be utilized for free cooling with bypassing the heat pump device. Their results demonstrated that a significant reduction in system size could be achieved compared to conventional GSHPs working with a single borefield.

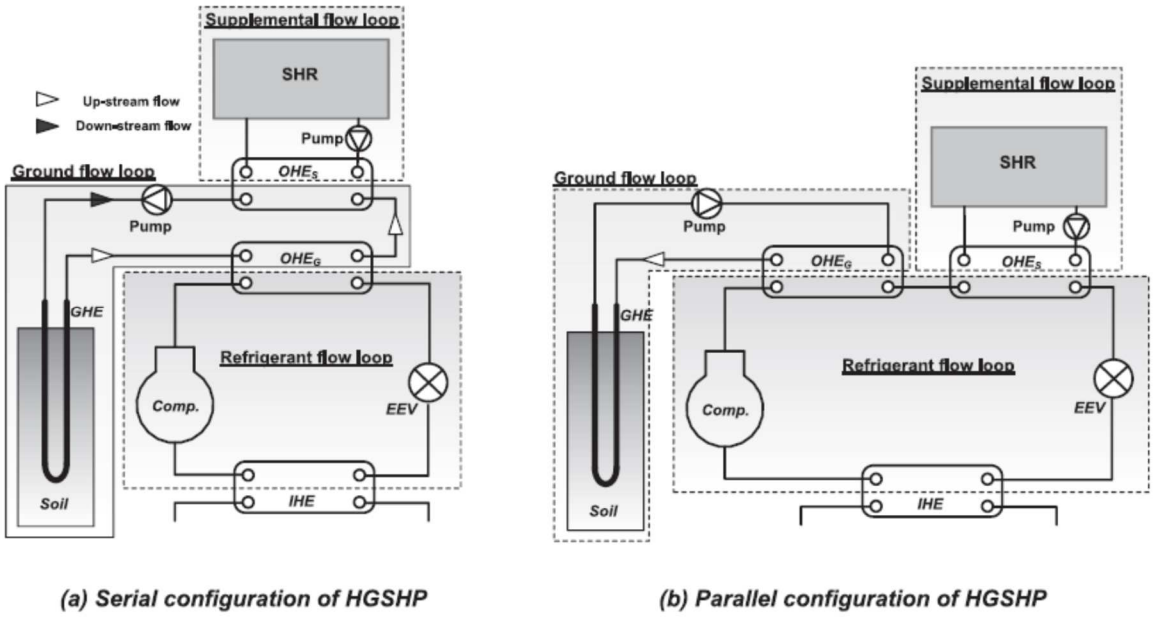

Figure 2.3. hybrid GSHPs with serial and parallel configurations (J. S. Lee et al., 2015)

2.3. Thermal plume development

Although hybridization is introduced as a method to balance the heating and cooling loads in a GSHP system, implementation of a hybrid system increases the system complexity since another fluid loop is required. As shown in Figure 2.2, cooling tower and plate heat exchanger are combined with GSHP and a control system is required to decide on using cooling tower and regulate system flow rate in accordance to the daily and seasonal load changes. As a result, a hybrid system might be ignored in a practical installation. In this situation, the reliance on groundwater flow to counteract load imbalance might be crucial on system performance, especially for multiple borehole systems.

Subsurface temperature around a borehole is affected by the thermal gradient between loop temperature and the ground. The formation of isotherm lines around a borehole is symmetrical if groundwater flow is neglected. In the presence of groundwater flow, however, advection is combined with conductive heat transfer and a more complex thermal plume or thermal front is observed in the thermal affected zone (Tolooiyan & Hemmingway, 2014).

A recent research showed that this thermal plume is almost independent of groundwater flow in the case of balanced loads in contrast to the imbalanced loads where even a modest groundwater flow causes significant change in subsurface temperatures as shown in Figure 2.4 (Dehkordi et al., 2015). The resulting temperature changes might interfere with other boreholes and hence, the system might experience efficiency loss in lifetime operation.

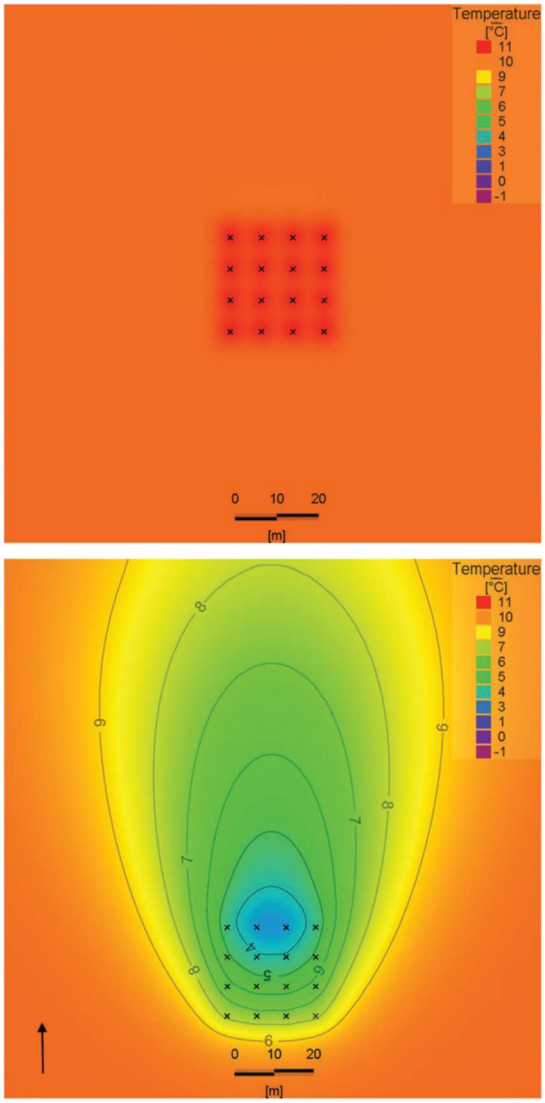

Figure 2.4. Thermal plume around a multiple borehole GSHP in 25th heating season with 10^{-7} m.s^{-1} groundwater flux under balanced (top) and imbalanced load (bottom) from (Dehkordi et al., 2015).

Additionally, a comprehensive sensitivity analysis was performed by Dehkordi and Schincariol, (2014) to evaluate the impact of system parameters on heat pump's heat exchange rates. The impact of parameters like groundwater flux, soil's thermal conductivity, heat capacity and porosity, thermal dispersivity, grout thermal conductivity, ground loop inlet temperature and undisturbed temperature of subsurface was examined on thermal plume development and outlet temperature profile of the boreholes over 25 years. They showed that groundwater flux and loop inlet temperature are the two parameters with the most impact on system's heat extraction rate. Their results also demonstrated the facilitating effect of groundwater flux greater than 10^{-8} $m.s^{-1}$ on subsurface thermal recovery.

Luo *et al.*, (2015) studied the impact of imbalanced load on a GSHP system performance for an office building in Germany in which the heating demand of 17 MWh heavily exceeded the cooling load of 8 MWh. Their results showed that the system had a higher efficiency for cooling purpose. Owing to a thermal plume formation and the gradual temperature drop within the ground, the heating COP degraded after a few years of operation whereas the cooling COP tends to rise. For this case, heating COP showed a 4% annual decline during a 4-year test period, keeping in mind that GSHPs are designed for a lifetime of 20 to 25 years.

2.4. Geothermal heat pump modeling studies

To model a geothermal heating system, both analytical (Diao et al., 2004; Ghoreishi-madiseh et al., 2019; Pophillat et al., 2020) and numerical (Diersch et al., 2011a, 2011b; Mensah et al., 2017) approaches have been considered to solve heat transfer equations within the subsurface. Different analytical models such as infinite line source, cylindrical source and finite length line source have been utilized by many to achieve solution to the heat transfer equation (M. Li & Lai, 2015). These analytical models are preferred due to their small computational times and great flexibility in parametric designs. Yet their practicality to actual systems is limited since it is difficult to incorporate real challenges such as complex geometries, ground heterogeneity, and borehole thermal interactions (Lucia et al., 2017).

Diao, Li and Fang, (2004) successfully established an analytical transient solution for combined advection-conduction transport equation in porous medium to simulate the effect of groundwater on the performance of GSHP systems. Their results emphasized the noticeable impact of groundwater flow on conductive temperature distribution within the ground and the resulting heat transfer rate. In some studies, however, a semi-analytical approach that couples a solution to the temperature field within the boreholes with a surrounding model outside the boreholes was proposed which utilized a computer numerical code for time integration (Koohi-Fayegh & Rosen, 2014).

Many researchers opted to use commercial software packages to simulate geothermal heating systems (Daemi & Krol, 2019; Hecht-Mendez et al., 2010; Hein et al., 2016; Mensah et al., 2017; Ozudogru et al., 2014). For instance, COMSOL Multiphysics was utilized to model transient heat and mass transport processes within borehole heat exchangers and energy piles (Ozudogru et al., 2014). To reduce the computation time, 1D linear elements along the pipes within boreholes were combined with a 3D finite element model in the surrounding subsurface. The temperature on the pipes exterior surface is then used as coupling parameter for two different models. The results have been validated with analytical solutions and showed satisfactory accuracy with reasonable computational effort. This practice of combining two different dimensional models is called dual-continuum approach and adopted by many researches (Daemi & Krol, 2019; Hein et al., 2016; Ozudogru et al., 2014) and is available in commercial packages like FEFLOW (Diersch et al., 2011a, 2011b).

Diersch *et al.*, (2011a, 2011b) provided a comprehensive review for finite element modeling of BHE systems including BHE types, governing equations, heat transfer coefficients, thermal resistances, model discretization and optimal meshing for a BHE. They also offered steady-state and transient model verification cases simulated in FEFLOW -a well-known finite element package- to illustrate functionality and capability of the FEFLOW BHE module. Daemi and Krol, (2019) also successfully used FEFLOW to simulate a multiple borehole GSHP system for an office

building in three Canadian cities with different climates and captured the impact of building thermal load in development of thermal plumes within subsurface.

Besides FEFLOW, various other software packages and codes have been utilized for BHE simulations. For instance, Mensah et al., (2017) used Ground Loop Design program (GLD) as a commercial software to optimal design of a vertical closed-loop geothermal heat pump system for a large residential apartment building and also presented experimental results to validate their data. Moreover, they investigated the impact of including a thermal storage tank in the system and claimed that such provision could result in remarkable decrease in peak load demand and the required heat exchanger length. Hein *et al.*, (2016) investigated GSHPs coupled with BHEs with a comprehensive numerical model in the open source finite element code OpenGeoSys. They considered dynamic load changes for a single BHE with site-specific conditions for the region of Leipzig, Germany. They reported that dual-season use of a GSHP with cyclic heating and cooling loads, in contrast to heating-only scenario with remarkable thermal imbalance, leads to less disturbance in ground temperatures thus allowing for better subsurface thermal recovery and higher heat transfer rates. However, the economic feasibility and advantage of such practice should be evaluated with balancing the saving in energy bill and extra cost associated with active cooling especially for small scale systems.

In addition to the aforementioned finite element software packages, finite difference code MT3DMS, which is a multi-species transport model, has been used to simulate heat transport in a single borehole GSHP for conduction and advection dominated scenarios (Hecht-Mendez et al., 2010). They compared their results with analytical solutions as well as the results obtained from finite difference code SEAWAT and finite element package FEFLOW. However, application of MT3DMS for heat transport modeling should be employed with care since unlike FEFLOW and SEAWAT, MT3DMS code does not account for coupling of flow and temperature fields. Thereby, changes in ground temperature in MT3DMS does not affect water viscosity, density and hydraulic conductivity. Nevertheless, temperature variations for shallow geothermal application is supposed to be small in general, and constant viscosity and density assumption claimed

acceptable. Moreover, the computational time and effort with finite element method in FEFLOW was reported to be lower than finite difference codes of MT3DMS and SEAWAT.

2.5. Environmental impact of geothermal heating

Reuse and redevelopment of brownfield sites is an efficient way of utilizing existing infrastructures to promote sustainable urban development. However, any potential health hazards should be addressed since brownfields are often contaminated with different compounds including petroleum products. Since these contaminants are susceptible to thermal treatment, employment of ground source heat pumps in brownfields might be a promising way to help in cleanup of such areas, as shown by Beyer et al., (2016) and Sommer *et al.*, (2013) for VOCs. In order to evaluate the impacts of shallow geothermal energy systems on subsurface and groundwater quality, environmental consequences of ground source heating should be understood. Table 2.1 lists four groups of environmental risks associated with shallow geothermal energy systems as follows (Bonte, 2013):

1. Hydrological impacts
2. Thermal impacts
3. Chemical impacts
4. Microbiological impacts

2.5.1. Hydrological impacts

The main hydrological risks of ground source heating are related to open-loop systems such as change of groundwater levels and the capture zone of water wells, especially if wells are used for public water supply. Since open-loop systems re-inject water in the same aquifer, perturbations in the groundwater flow pattern can be noticeable to a distance of up to several kilometres (Bonte, 2013). Moreover, since the capture zone of a public water supply well is legally protected, planning of GSHP systems should be done carefully to avoid negative consequences on groundwater level and quality. Furthermore, if boreholes are constructed in different aquifers, groundwater flow patterns may be influenced due to improper grout sealing around the

boreholes even in closed-loop systems. This in turn might lead to cross-aquifer flows and contaminants transport (Hähnlein et al., 2013).

Table 2.1. Different impacts and risks associated with low temperature shallow geothermal energy usage on groundwater systems, reproduced from Bonte, (2013)

Effects	Probability∞	Consequence‡	Risk§
Hydrological impacts			
Changing water levels and fluxes	++	Desiccation, water logging, settlements	±
Changing of other well's capture zone	++	Increasing vulnerability, pollutions	++
Poorly sealed boreholes	+	Cross aquifer flow	++
Thermal impacts			
Changing water temperature	++	Temperature, reaction kinetics	+
Chemical impacts			
Mixing processes	++	Salinity, IMIPO, OMIPO	++
Mobilization of groundwater pollution plumes	±	IMIPO, OMIPO	++
Oxidation of organic matter	±	Nutrients, DOC, color	+
Oxidation of iron-sulfides	±	Fe, SO4, As, Ni, Co, Zn	+
Dissolution/precipitation carbonates	±	Ca, HCO3, Sr	±
Dissolution/precipitation of silicates	±	SiO2	±
Leaching from installation materials	±	Cd, Cu, Cr, Ni, Pb, VC	+
Leaking anti-freeze fluids or additives	±	Glycol, biocides & corrosion inhibitors	++
Microbiological impacts			
Introduction of pathogens	-	Pathogens	±
Changing biodegradation rate	±	Nutrients, IMIPO, OMIPO	+ or -
Changing microbiological population	+	Unknown	?

Footnotes: **∞:** - small probability, ± medium probability, + large probability, ++ will always occur;
‡: IMIPO: Inorganic micro pollutants; OMIPO: Organic micro pollutants; DOC: Dissolved Organic Carbon; VC: Vinyl chloride.
§: - negative risk (opportunity), ± no apparent risk, + small risk, ++ high risk.

2.5.2. Thermal impacts

As stated in previous sections, the surplus heat extracted from or injected to the ground due to load imbalance as well as seasonal thermal storage system in which excess heat is deliberately stored in the subsurface, leads to gradual change in ground temperature. This temperature change could result in GSHP efficiency loss or in the severe cases, termination of heat transfer in the system if the temperature difference between subsurface and the refrigerant vanishes. For instance, a study in Winnipeg, Canada, demonstrated that using the aquifer solely for cooling

purposes was not sustainable due to long-term rising groundwater temperatures and short circuiting of warm and cold wells for an open-loop groundwater heat pump facility (Ferguson & Woodbury, 2006). In case of surface water heat pumps, if the capacity of water body is not properly selected, the resulting temperature increase might impact oxygen level and hence, aquatic life.

More importantly, the temperature difference induced by heat pumps in the subsurface, affects groundwater flux due to the changes in water viscosity and density. For example, formation of density-driven flows might change the direction of groundwater flow as seen in thermal remediation activities. For instance, the effects of low-temperature (50°C) electrical resistance heating (ERH) as a thermal remediation treatment on subsurface flow and solute transport was performed by Krol et al., (2011). Their results showed the emergence of strong buoyant flows with ground temperature rise resulted in significant changes in mass transport.

Krol et al., (2014) also investigated the impact of ERH with higher temperature (80°C) on subsurface flow and transport by means of the buoyancy ratio for soils with different permeability. Their result emphasized that thermal remediation can lead to unexpected transport of the contaminants due to strong buoyancy-driven flows. Moreover, applying heat to the subsurface might result in bubble formation and mobilization for volatile compounds which in turn can lead to movement and eventual collapse of bubbles when reaching cooler zones, thus spreading the contamination (Krol, Mumford, et al., 2011). However, it should be noted that the increase in temperature by ERH usually exceeds the temperature range resulted from geothermal heat pump applications.

In addition to thermal plume development and change in groundwater flow direction, deviation from undisturbed temperature could impact sorption of the contaminants and therefore, reaction kinetics (Ngueleu et al., 2018; Sleep & Mcclure, 2001). A more in-depth study on the impact of temperature on sorption is provided in section 2.6

2.5.3. Chemical impacts

Most of the research in the field of chemical impacts of shallow geothermal energy relates to open-loop system effects (Hähnlein et al., 2013). It has been shown that these systems might change groundwater chemistry due to mixing of different groundwater types. For instance, when fresh and saline groundwater are in proximity, an improper well screen setting of an open-loop heat pump might lead to fresh groundwater getting salinized. Furthermore, well-clogging might occur due to mineral precipitation in the systems with temperatures higher than 25^{o}C (Bonte, 2013).

Groundwater quality is also prone to impacts from the temperature changes resulting from closed-loop GSHP operation. Saito *et al.*, (2017) sampled groundwater from a geothermal heating site in Tokyo, Japan which had experienced 13 months of heating followed by 14 months of cooling period. The samples were gathered at two different monitoring wells located near U-tubes (within thermally affected zone) and far from the facilities (non-affected reference well) and analyzed for inorganic ions like Na^{+}, K^{+}, Mg^{2+}, and NH_4^{+} as well as heavy metals like B, Si and Li and dissolved organic carbon. Their results showed changes in concentrations from 4% to 31% for about 7^{o}C increase in subsurface temperature.

Closed-loop systems might also cause chemical influences on the groundwater if the antifreeze agents, biocides or corrosion inhibitors present in the ground loop piping system leak to the ground. It is reported that the addition of corrosion inhibitors or biocides in closed-loop systems can inhibit biodegradation of antifreeze agents such as ethylene glycol, propylene glycol and betaine, even though these agents are considered biodegradable in both aerobic and anaerobic environments (Klotzbucher et al., 2007).

The impact of geothermal heating can also be significant if contaminated aquifers are involved. Research has shown that even small temperature changes might result in alteration in redox reactions which play an important role in the biodegradation process. For instance, the

dominance of nitrate reduction at 10°C shifts to iron reduction at 25°C in groundwater (Jesußek et al., 2013). Moreover, under increased temperature caused by GSHPs, mobilization of dissolved organic carbon (DOC) grows which in turn can lead to coloration of water and subsequent call for treatment (Brons et al., 1991). This increase in mobilization might also lead to contaminant's spread in the aquifer which can impact remediation process. The favorable impact of elevated temperatures on biodegradation of organic contaminants has been studied by several researchers in the past decades (Alagappan & Cowan, 2004; Beyer et al., 2016; Chang et al., 2011; Stempvoort & Biggar, 2008) which will be described in detail in section 2.8.

2.5.4. Microbiological impacts

Groundwater can contain microorganisms such as bacteria, fungi and protozoa. Biodegradation is defined as decomposition of compounds by these microorganisms. Subsequently, bioremediation is the process that decreases contamination in soil and water by providing favorable biological conditions to allow microbes to degrade the pollutants.

Bioremediation involves redox processes where an electron acceptor is added to cause oxidation of a reduced contaminant like hydrocarbons. Microorganisms collect energy in this electron transfer process, so they rely on natural biodegradation of organic contaminants for their existence and reproduction (*National Research Council - In Situ Bioremediation: When Does It Work?*, 1993). Common electron donors in bioremediation are hydrocarbons (oils), Polycyclic Aromatic Hydrocarbons (PAHs), Poly-Chlorinated Biphenyls (PCBs), less chlorinated solvents like Vinyl Chloride (VC), and soil organic matter while frequent electron acceptors are oxygen, nitrate, sulfate and iron. The process which uses oxygen as electron acceptor is called *aerobic oxidation* while the involvement of other electron acceptors make the process *anaerobic oxidation* (*National Research Council - In Situ Bioremediation: When Does It Work?*, 1993).

Although there are various factors that can affect biodegradation, temperature plays a crucial role in facilitating biodegradation due the temperature preference of each microorganism type

for proliferation, as discussed in section 1.6. Therefore, temperature variation resulted from geothermal heating application can significantly change the biodegradation rates. Additionally, it has shown that with decrease in temperature toward the freezing point, the mass transport in cell membrane which allows for contaminants' access to the cell enzymes, tends to cease and the biodegradation is diminished (Si-zhong et al., 2009).

Owing to the sensitivity of the microbiological activity level to temperature, biodegradation of the organic pollutants in groundwater is significantly dependent upon aquifer temperature changes (Beyer et al., 2016). Moreover, removal of nutrients by biodegradation process is essential for groundwater quality as it reduces the growth of pathogens in drinking water infrastructure. In this regard, thermal plumes resulting from geothermal heat pump applications might enhance or hinder biodegradation depending on the temperature range, contaminant type, and microorganism's temperature preference. Thereby, assessment of geothermal heat pump as a bioremediation technology couples different fields of fluid dynamics, heat transfer, contaminant transport and biological science which adds to the complexity of the interdisciplinary problem. As the complexity rises, it is more difficult to address the problem without a thorough investigation for each specific case, since many unknown consequences and risks are involved as indicated by Table 2.1. A more in-depth study on the impact of temperature on microorganisms and biodegradation kinetics is provided in section 2.8.

2.6. Effect of temperature on sorption

Impact of temperature on adsorption/desorption process is another aspect of the research which is linked to bioremediation assessment. By defining “bioavailability” as the hydrocarbon’s inclination to interact with microorganisms, it is inferred that contaminants sorbed onto the soil or aquifer organic matter will be less bioavailable for biodegradation (Si-zhong et al., 2009).

Finizio and Guardo, (2001) studied the impact of temperature on solubility and octanol-water partition coefficient for different organic compounds and showed solubility increases with

temperature for the range of 15 to 35°C for benzene and toluene. Thereby, increasing the temperature could lead to lower partition coefficients thus allowing for less tendency for adsorption of the contaminant. Therefore, increased temperature could lead to more bioavailability for biodegradation process. Ngueleu *et al.*, (2018) also studied the dependency of sorption of benzene and naphthalene to temperature and salinity for semi-arid coastal soil and verified that an increase in temperature would lead to a decline in sorption coefficient.

Furthermore, a series of column experiments were conducted to study the effect of temperature on adsorption of some organic contaminants onto the soil by Sleep and Mcclure, (2001). Their results demonstrated that by increasing the temperature from 22 to 92°C, sorption coefficients declined by 35%, 40% and 60% for toluene, perchloroethylene (PCE) and naphthalene, respectively. This in turn can be interpreted as facilitating the impact of the increased temperature on desorption of organic contamination from the soil and achieving accelerated remediation.

Sorption can be described by sorption isotherms including linear, Freundlich and Langmuir. Isotherms show the correlation between solute and sorbed concentration at constant temperature. The simplest model is linear (Henry) sorption isotherm which assumes a linear relationship between sorbed and solute concentrations with a sorption coefficient that is often referred to as the distribution coefficient. Freundlich and Langmuir, on the other hand, assume more complex nonlinear correlations (Fetter, 2008). The distribution coefficient is a function of organic carbon partition coefficient $\left(k_{oc}\right)$ which inversely correlates to contaminant solubility in water $\left(S_w\right)$ and the relationship is typically described by empirical correlation equations available for different contaminants. A relevant equation for aromatic hydrocarbons like benzene and toluene is presented in chapter 3.

2.7. First-order and Michaelis-Menten (Monod) kinetics model for biodegradation

Two models which are commonly used to describe biodegradation kinetics are first-order decay and Michaelis-Menten (Monod) kinetics. First order kinetics describes substrate (contaminant) biodegradation velocity as proportional to substrate concentration (Bekins et al., 1998):

$$\frac{dS}{dt} = -\vartheta S \tag{2-1}$$

where, S is concentration of the substrate (mg.L^{-1}), and ϑ is first order decay rate (h^{-1}).

Monod kinetics, on the other hand, describes microbial growth on a limiting substrate by a pure culture of microorganism with a hyperbolic equation (Bekins et al., 1998):

$$\mu = \mu_m \frac{S}{S + k_s} - b \tag{2-2}$$

$$\frac{dS}{dt} = -\frac{\mu_m}{Y} B_c \left[\frac{S}{S + k_s}\right] \Rightarrow v = -v_{\max}\left[\frac{S}{S + k_s}\right] \tag{2-3}$$

where, μ is microbial growth rate (h^{-1}), $\mu_m$is maximum specific growth rate (h^{-1}), Y is biomass yield (mg of biomass per mg of substrate), B_c is biomass concentration (mg of biomass per L), b is microbial decay rate (h^{-1}) and k_s (called half saturation constant) is the substrate concentration at which the reaction velocity is half of the maximum velocity (mg.L^{-1}). Combining these three parameters: μ_m, Y and B_c, yields $v_{\max}$, which is the maximum degradation velocity or maximum substrate utilization rate (mg.L^{-1}.h^{-1}) (Equation 2-3). Thereby, Monod equation states that substrate utilization rate $\left(dS/dt \text{ or } v\right)$ approaches an asymptote for high values of substrate concentration (see Figure 2.5).

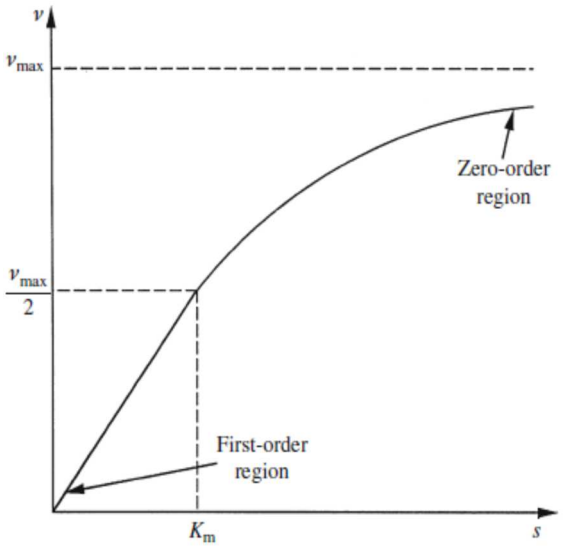

Figure 2.5. A sample Michaelis-Menten plot (Doran, 2013)

If the initial substrate concentration is significantly lower than the half saturation constant, equation (2-3) can be approximated by (2-4), which is the same as first order decay equation:

$$\frac{dS}{dt} = -\frac{v_{max}}{k_s} S = -\vartheta S \qquad (2\text{-}4)$$

Thereby, a first-order biodegradation kinetics is only valid when half saturation constant is much greater than substrate's concentration $\left(k_s \gg \mathrm{S\ in\ Figure\ 2.5}\right)$. A comparison of Monod and first order kinetics by Wang, Qin and Witarsa, (2018) showed that Monod kinetics is slower at the beginning so it is capable of modeling the acclimation phase as the lag time from introduction of microorganism to the contaminant to actual biodegradation process. Although first-order biodegradation kinetics have been extensively used for a wide range of substrate concentrations (Suarez & Rifai, 1999), it is reported to be invalid in many case when dealing with BTEX contaminants (Bekins et al., 1998) since the assumption of substrate's concentration, S, being much less than half saturation constant, K_s, was not verified in some cases.

2.8. Microbial growth, biodegradation kinetics and the effect of temperature

Since the aim of this study is the assessment of geothermal heating as a thermal bioremediation of contaminants in brownfields, petroleum hydrocarbons like benzene, toluene, ethylbenzene and xylene (BTEX), were chosen as the target contaminants since they are common brownfield contaminants and are susceptible to heat treatments. In this regard, a literature review was performed on biodegradation of BTEX compounds with respect to biodegradation kinetics models, microorganism involved, and the impact of temperature. Moreover, since BTEX compounds are typically degraded in aerobic environments (Alagappan & Cowan, 2004), the focus was on aerobic biodegradation.

Applicability of bioremediation techniques for petroleum-contaminated groundwater in cold climates, where groundwater temperature is less than 10°C, was the subject of a few studies in the past decades (Stempvoort & Biggar, 2008). It was claimed that hydrocarbon biodegradation can even occur at temperature as low as -6°C within seasonally frozen ground by psychrophile (cold loving) or psychrotroph (cold tolerant) microorganisms. Their rate of degradation, however, is not comparable to mesophilic microorganisms which prefer moderate temperatures. Stempvoort and Biggar, (2008) also reported common BTEX first order biodegradation rate constants at the sites in cold regions of western Canada (Alberta) in the range of 0.001 to 0.005 (day^{-1}) which in turn led to estimation of half-life of BTEX components as 1 to 2 years. These values, although slightly lower, are in agreement with rate constants reported at warmer sites in United States (Stempvoort & Biggar, 2008). It was suggested that the relatively lower biodegradation rates in Canadian sites were the result of lower temperatures and possible existence of co-contaminants common in oil and gas facilities in western Canada.

Biodegradation of petroleum hydrocarbons at variable site temperatures from 1 to 10°C, representing summer temperature fluctuations at Nunavut, Canada, was studied and compared with results from constant 6°C temperature (Chang et al., 2011). Their results showed significant increased biodegradation rates for variable temperature conditions which can be linked to

nonlinear growth of psychrotrophic microorganisms between 4.7 to 10°C. Therefore, even small and periodic changes in temperature can lead to remarkable enhancement in biodegradation rates.

A comprehensive study by El-naas, Acio and Telib, (2014) identified various microorganism involved in aerobic biodegradation of BTEX hydrocarbons as well as kinetics and mathematical modeling. Among many microorganisms reported in Table 2.2, Pseudomonas putida (P. putida) was identified as one of the most common bacterial genera with the ability to degrade BTEX compounds individually and in a mixture.

Moreover, Table 2.3 presents summary of growth kinetics parameters from the comprehensive review performed by (El-naas et al., 2014). As can be seen, Monod parameters are reported for a certain temperature. Hence, implementing temperature-dependent biodegradation in FEFLOW simulation is applicable via Monod parameters (such as specific growth rate or half saturation constant) only if the correlations with temperature for a certain microorganism are known.

Table 2.2. Examples of different aerobic degraders for BTEX, reproduced from El-naas et al., (2014)

Microorganism	**Substrate**
Bacteria	
Rhodococcus rhodochrous	BTEX
Alcaligenes xylosoxidans Y234	Benzene, Toluene and Phenol
Rhodococcus sp. DK17	BTE, phenol, isopropylbenzene, and other alkylbenzene isomers
Pseudomonas putida	BTEX
Pseudomonas putida	BTE(o-)X
Pseudomonas fluorescens	BTE(o-)X
Pseudomonas aeruginosa	Benzene
Pseudomonas putida F1 ATCC 700007	BT, phenol
Pseudomonas putida F1	BT
Burkholderia (Ralstonia) pickettii PKO1	BT
Rhodococcus pyridinovorans PYJ-1	Benzene, toluene, and m-xylene
Pseudomonas putida CCMI 852	BTX
Achromobacter xylosoxidans	BTEX
Pseudomonas spp.	BTX
Pseudoxanthomonas spadix BD-a59	Benzene, toluene, ethylbenzene, o-, m-, p-xylene
Alcaligenes (Achromobacter) xylosoxidas	BTX
Pseudomonas putida YNS1	BTEX
Bacillus sphaericus (MTCC 8103)	BTEX
Mycobacterium cosmeticum byf-4	BTE(o-)X
Fungi	
Phanerochaete chrysosporium	BTEX
Cladophialophora sp. T1	TEX
Paecilomyces variotii CBS115145	BTE (o-, m-, p) X
Cladophialophora psammophila	TEX

Table 2.3. Summary of biodegradation kinetics for BTEX, reproduced from El-naas et al., (2014)

Microorganism	Concentration range $(mg.L^{-1})$	Model type	Compounds	μ_m (h^{-1})	k_s $(mg.L^{-1})$	k_i $(mg.L^{-1})$	Temp. $(^{\circ}C)$
P. putida	10-400	Monod	B T	0.1631 0.1722	71.18 62.56	- -	30
P. putida F1	15-30-60-90	Monod	B T	0.5 0.58	10.11 10.8	- -	30
P. putida F1	2-250	Andrews	T	0.78	5	753	32
P. putida	10-400	Han-Levenspiel	B	0.3626	-	64.12	30
Rhodococcus pyridinovorans	25-30-50	competitive	T T-B T-m-X B-T m-x-T	0.3003 0.13 0.12 0.080 0.035	- 6.2 6.2 4.8 4.7	57.40 12.4 17.2 6.7 9.6	32
P. putida F1	90	Andrews	B T	0.62 0.61	1.65 6.47	180 88	30
Pesudomonas aeruginosa	46-274	Andrews	B T E X	0.0194 0.0064 0.0340 0.0060	8.349 9.851 211.791 1.427	191.89 48.48 310.56 153.55	30
Planococcus sp. strain zd22	0–11 mM	Luong	B	0.34	0.041	-	20
Planococcus sp. strain zd22	0–11 mM	Luong	B	0.34	0.041	-	20
Rhodococcus rhodochrous	0–80	SKIP	B T E X	0.41 0.42 0.45 0.05	1.11 1.24 1.75 20		35
P. putida DSM 921T	39.5 ± 5.9	SKIP, unspecific interaction	B T p-X	0.88 1.91 0.1	0.3 0.5 -	-	30

Since aromatic hydrocarbons are commonly present in a mixture, contaminant interaction is important for dealing with contamination problem and choosing a cleanup strategy. Interaction of different contaminants can have negative outcomes such as inhibition and competition or positive result like co-metabolism in a biological treatment plan. Experimental investigations reported significant difference in biodegradation patterns for individual contaminants and mixtures (Deeb & Alvarez-cohen, 1999). As a single contaminant, toluene showed the highest rate of degradation. Benzene, ethylbenzene, and the xylenes were identified as having the next highest rates, respectively, if examined as individual compounds. In a BTEX mixture, however, ethylbenzene took first place followed by toluene, benzene, xylenes In fact, ethylbenzene

showed inhibitory impact on other compounds (Deeb & Alvarez-cohen, 1999). Moreover, it has been shown that toluene outcompetes benzene in a mixture in the presence of P. putida bacteria (Littlejohns & Daugulis, 2008; Reardon et al., 2000). Another study on the biodegradation of BTEX mixtures demonstrated that while Stenotrophomonas maltophilia T3-c microorganism could not grow solely on xylene, the presence of toluene assisted co-metabolic degradation of xylene (E. Y. Lee et al., 2002). This interaction of contaminants adds to the complexity of the fuel hydrocarbon's biodegradation and makes predicting the behavior of BTEX in mixtures more difficult.

Suarez and Rifai, (1999) presented Monod parameters for BTEX compounds gathered from 18 laboratory studies in aerobic conditions. They reported half saturation constants for benzene in the range of 0.31 to 20.31 ($mg.L^{-1}$) while maximum specific degradation rate $\left(\mu_m /Y\right)$ varied from 0.78 and 25.07 ($mg.mg^{-1}.day^{-1}$). This wide range shows significant dependency of results to experimental conditions such as temperature, sorption phenomena, different electron acceptors, availability of inorganic nutrients, nature of studied culture (i.e., pure or mixed), competition of microorganisms, etc. In fact, Monod equation is empirical and biodegradation parameters are strongly site-specific and hence, such values are not universally applicable. Moreover, Monod equation does not account for toxicity of contaminants and inhibitory effects and therefore can overestimate the biodegradation coefficients of compounds at high concentrations.

Furthermore, Suarez and Rifai, (1999) presented a comparative study between laboratory and field results which showed lower biodegradation constants in field studies. Not surprisingly, their study also shows that degradation rates for aerobic metabolism of BTEX compounds exceeds anaerobic biodegradation by orders of magnitudes. The range minimum 90th percentile of benzene first-order rate constant was reported to be between 0 to 0.445 (day^{-1}) with a mean value of 0.335 (day^{-1}) for aerobic condition, indicating moderate degradability in the presence of oxygen. In comparison, the minimum 90th percentile range for anaerobic biodegradation of

benzene is reported between 0 to 0.024 (day^{-1}) with mean value of 0.008 (day^{-1}) (Suarez & Rifai, 1999).

To address the effect of temperature on biodegradation rates, Alagappan and Cowan, (2004) conducted batch experiments examining temperature and dissolved oxygen concentration effects on benzene and toluene degradation by P. putida F1 strain as a mesophile in the range of 15 and 35°C. The Monod kinetics parameters for benzene at 20°C were reported as $\mu_m = 8.64$ (day^{-1}), K_s=2.45 ($mg.L^{-1}$), Y=0.69, B=2.7 ($mg.L^{-1}$). To couple the temperature effect, Arrhenius function presented in equation (2-5) was used, as one of the common models to represent exponential microorganism growth based on temperature change. The Arrhenius equation, however, fails to predict decline in microbial growth rate at higher temperatures when enzyme thermal denaturation process is activated (Alagappan & Cowan, 2004). To quantify temperature effects and overcome limitations in Arrhenius equation, the Topiwala-Sinclair model in equation (2-6) was proposed (Alagappan & Cowan, 2004):

$$\mu_m = A\, e^{-E_a/(R_u T)} \tag{2-5}$$

$$\mu_m = A\, e^{-E_a/(R_u T)} - B\, e^{-E_b/(R_u T)} \tag{2-6}$$

where μ_m is temperature dependent maximum specific growth rate (day^{-1}), A and B are exponential factors (day^{-1}), E_a is the activation energy for cell growth ($kJ.mol^{-1}$), R_u is the universal gas constant ($kJ.mol^{-1}$), T is the absolute temperature (K), and E_b is the activation energy for thermal denaturation processes ($kJ.mol^{-1}$) which represent the decline in microbial activity at high temperatures.

2.9. Effective solubility and inhibitory concentration for biodegradation

Since benzene and toluene originate from petroleum fuel spills where they only constitute a small fraction of the fuel, actual aqueous benzene and toluene concentrations are typically far less than their reported water solubility. In fact, effective solubility of any compound can be achieved by

multiplying its mole fraction by its solubility (*How To Evaluate Alternative Cleanup Technologies For Underground Storage Tank Sites*, 2004). Thereby, though solubility of benzene and toluene in water is reported to be about 1780 $mg.L^{-1}$ and 515 $mg.L^{-1}$, typical concentration of benzene and toluene in groundwater has been commonly reported in the range of 24-95 $mg.L^{-1}$ and 12-60 $mg.L^{-1}$, respectively (*How To Evaluate Alternative Cleanup Technologies For Underground Storage Tank Sites*, 2004). In addition, a comparison of BTEX concentration in different geographic areas in the world, showed typical concentrations from a few micrograms to the maximum of 117 $mg.L^{-1}$ for benzene and 47 $mg.L^{-1}$ for toluene which is still an order of magnitude smaller than their solubility (Logeshwaran et al., 2018). Moreover, in an extensive research study by Suarez & Rifai, (1999) for aerobic biodegradation, initial concentrations from 18 laboratory studies are reported in the range of 6-110 $mg.L^{-1}$ for benzene and 2-100 $mg.L^{-1}$ for toluene. However, the acceptable limits for benzene in groundwater is 5 $\mu g.L^{-1}$ based on Health Canada's guideline (*Guidelines for Canadian Drinking Water Quality: Guideline Technical Document Benzene*, 2009) and for toluene, the limit is 60 $\mu g.L^{-1}$ (*Guidelines for Canadian Drinking Water Quality Guideline Technical Document Toluene, Ethylbenzene and Xylenes*, 2014).

Moreover, BTEX in high concentration are toxic to the microorganism involved in disintegration process thus hinder biodegradation. As an example, toxicity threshold of benzene for P. putida bacteria as a common BTEX degrader, is reported as 92 $mg.L^{-1}$ by Powers et al., (2001). Another study claimed inhibitory effect of concentrations higher than 100 $mg.L^{-1}$ and no degradation for benzene or toluene was observed with initial concentration of 250 $mg.L^{-1}$ (Alvarez et al., 1991). Similar results were obtained by Junfeng, Xiang and Zhifeng, (2008) who showed significant reduction in BTEX removal rate in case of initial concentration higher than 100 $mg.kg^{-1}$ in soil in an anaerobic environment.

Lastly, different strains of the microorganism could have greater tolerance range for the contaminant. For instance, Pseudomonas sp. BTEX-30 bacteria have been incorporated in biodegradation of BTEX in batch experiments with initial concentration of 250 $mg.L^{-1}$ (Khodaei et al., 2017). Nevertheless, most reported concentration values where bioremediation was

occurring are far less than solubility limits of the compounds suggesting that high concentrations are toxic for the degrading microorganisms.

Chapter 3 - Model development

3.1. Governing equations

The governing equations for groundwater flow, heat and mass transport equations for BHE systems, taken from the FEFLOW reference book and manual, are presented in this chapter (Diersch, 2009a, 2014; Diersch et al., 2010). These equations are based on conservation of mass, momentum and energy combined with some constitutive relations. The flow equation in saturated porous media is described by equation (3-1):

$$S_s \frac{\partial h}{\partial t} + \nabla . q = Q + Q_{EOB} \tag{3-1}$$

where S_s is specific storage coefficient, h is head, q represents Darcy flux vector and Q is a general source/sink function and Q_{EOB} is called extended Oberbeck-Boussinesq function. The standard Boussinesq approximation is a simplification that neglects all density dependencies except for buoyancy terms and is considered valid for small to moderate density changes. With extended Oberbeck-Boussinesq assumption, which will be described in section 3.7, additional terms are considered as density dependent. Therefore, if the standard Boussinesq approximation is assumed, the extended Oberbeck-Boussinesq function $\left(Q_{EOB}\right)$ is neglected (Diersch, 2009b).

Momentum balance equation for groundwater flow in subsurface is described by the temperature-dependent Darcy law (Diersch, 2009a; Diersch et al., 2010):

$$q = -Kf_\mu \left(\nabla h + \frac{\rho^f - \rho_0^f}{\rho_0^f} e \right) \qquad e = -\frac{g}{\|g\|} \tag{3-2}$$

$$\rho^f = \rho_0^f \left[1 - \beta \left(T - T_0 \right) \right] \tag{3-3}$$

$$f_\mu = \frac{\mu_0^f}{\mu^f} \qquad \mu^f = \mu^f \left(T \right) \tag{3-4}$$

where K represents hydraulic conductivity tensor, f_μ represents viscosity dependency to temperature, ρ^f and ρ_0^f are fluid density at current and reference temperatures and e is gravitational unit vector. β is thermal expansion coefficient and T and T_0 are subsurface temperature at current and reference states. Finally, μ^f and μ_0^f are dynamic viscosity at current and reference temperatures. In all of the equations superscript f and s denote fluid and solid phase, respectively.

Equation (3-5) describes the thermal energy balance equation for saturated domain (Diersch, 2009a; Diersch et al., 2010):

$$\frac{\partial}{\partial t}\left[\left(\varepsilon\rho^f c^f + (1-\varepsilon)\rho^s c^s\right)(T-T_0)\right] + \nabla.\left(\rho^f c^f q\,(T-T_0)\right) - \nabla.\left(\Lambda.\nabla T\right) = H_e \qquad (3\text{-}5)$$

in which $\rho^s c^s$ and $\rho^f c^f$ represent volumetric heat capacity of solid and fluid, ε corresponds to porosity, and H_e represents the thermal sink/source. Λ in the above mentioned equation is thermal hydrodynamic dispersion tensor given by constitutive relation (3-6):

$$\Lambda = \left[\varepsilon\lambda^f + (1-\varepsilon)\lambda^s\right] I + \rho^f c^f \left[\alpha_T \|q\| I + (\alpha_L - \alpha_T)\frac{q \otimes q}{\|q\|}\right] \qquad (3\text{-}6)$$

where λ is thermal conductivity, α_L and α_T are longitudinal and transverse thermodispersivity, respectively, while I represents identity matrix.

Moreover, the balance of contaminant mass for a reactive single-species solute transport in the fluid phase is given by equations (3-7) (Diersch, 2009a):

$$\frac{\partial}{\partial t}\left(\varepsilon_f R C\right) + \nabla.\left(qC\right) - \nabla.\left(D.\nabla C\right) = Q_d + \varepsilon_f r_{\hom}^f + \varepsilon_s r_{\hom}^s \qquad (3\text{-}7)$$

In the above equations, C is concentration, R is retardation factor, Q_d is non-reactive bulk production rate, ε_f is fluid volume fraction, ε_s is solid volume fraction, r^f_{hom} is fluid phase homogeneous reaction rate and r^s_{hom} represents homogeneous reaction rate for solid phase. For saturated media, volume fraction of solid and fluid phase can be rewritten as a function of porosity (Diersch, 2009b):

$$\varepsilon_f = \varepsilon \quad , \quad \varepsilon_s = (1-\varepsilon) \tag{3-8}$$

Moreover, D in equation (3-7) represents hydrodynamic dispersion tensor which can be described by equation (3-9):

$$D = (\varepsilon D_d) I + \left[\beta_T \|q\| I + (\beta_L - \beta_T) \frac{q \otimes q}{\|q\|} \right] \tag{3-9}$$

Where D_d is diffusion coefficient and β_L and β_T are longitudinal and transverse dispersivity, respectively.

The sorption isotherm function explains the correlation between the sorbed mass (C^s) and the dissolved species concentration (C) (Diersch, 2009a):

$$C^s = \chi C \tag{3-10}$$

where χ is sorption isotherm which can be described by different models such as linear (Henry), Langmuir and Freundlich. The simplest model is linear (Henry), which assumes the sorption function as constant:

$$\chi = k = \rho_s k_d \tag{3-11}$$

in which ρ_s and k_d are solid particle density and distribution coefficient, respectively, and k is dimensionless sorption coefficient which is used in FEFLOW software to assign linear sorption.

Furthermore, retardation factor can be described by equation (3-12):

$$R = 1 + \frac{(1-\varepsilon)}{\varepsilon}\chi \tag{3-12}$$

By substitution of (3-11) into (3-12), it is reduced to equations (3-13) and (3-14) which link retardation factor to solid particle density, porous medium bulk density and distribution coefficient as follows:

$$R = 1 + \frac{(1-\varepsilon)}{\varepsilon}\rho_s k_d \tag{3-13}$$

$$R = 1 + \frac{\rho_b k_d}{\varepsilon} \tag{3-14}$$

Note that bulk density can be calculated from the following equation:

$$\rho_b = (1-\varepsilon)\rho_s \tag{3-15}$$

For first-order decay, the homogenous reaction rates for fluid and solid phase can be described by:

$$r^f_{\text{hom}} = -\vartheta C \tag{3-16}$$

$$r^s_{\text{hom}} = -\vartheta C^s = -\chi\vartheta C \tag{3-17}$$

where ϑ is first-order decay rate constant.

Therefore, by substitution of equations (3-11), (3-12), (3-16) and (3-17) into equation (3-7), the mass balance equation for first-order kinetics and linear sorption can be written as:

$$\frac{\partial}{\partial t}\left(\varepsilon RC\right)+\nabla.\left(qC\right)-\nabla.\left(D.\nabla C\right)=Q_d-\varepsilon R\vartheta C \tag{3-18}$$

Similarly, for Monod biodegradation kinetics, the homogenous reaction rates for fluid and solid phase can be described by:

$$r_{\hom}^{f}=\frac{-\nu_{\max}C}{k_s+C} \tag{3-19}$$

$$r_{\hom}^{s}=\frac{-\nu_{\max}C^{s}}{k_s+C^{s}}=\frac{-\nu_{\max}\chi C}{k_s+\chi C} \tag{3-20}$$

where $\nu_{\max}$ and k_s are Monod (Michaelis-Menten) constants which were introduced in chapter 2 with equations (2-2) and (2-3). The reader is referred to (Diersch, 2009a; Diersch et al., 2010) for further information.

3.2. Borehole heat exchanger types and modeling remarks

Closed-loop BHEs are often categorized by their tube configurations as single U-tube (1U), double U-tube (2U) and coaxial as shown in Figure 3.1, in which the coaxial type could be coaxial with annular (CXA) and centered (CXC) inlet (Diersch, 2014). For pipes, high-density polyethylene (HDPE) is the most common material due to its lower cost and resistance to corrosion. Thermal conductivity of HPDE pipes (0.45 $W.m^{-1}.K^{-1}$) is not comparable to copper (390 $W.m^{-1}.K^{-1}$) but owing to the cost-saving and resilience, HPDE is preferred (Banks, 2012). The gap between the pipes and borehole wall is usually filled with bentonite-based grout which in turn reduces the risk of leakage and enhances the heat transfer with subsurface. Due to the common size and spacing required to prevent thermal short circuiting between the pipes, the U-tube typical width is about 90–100 mm and borehole diameter is in the range of 125-130 mm (Banks, 2012).

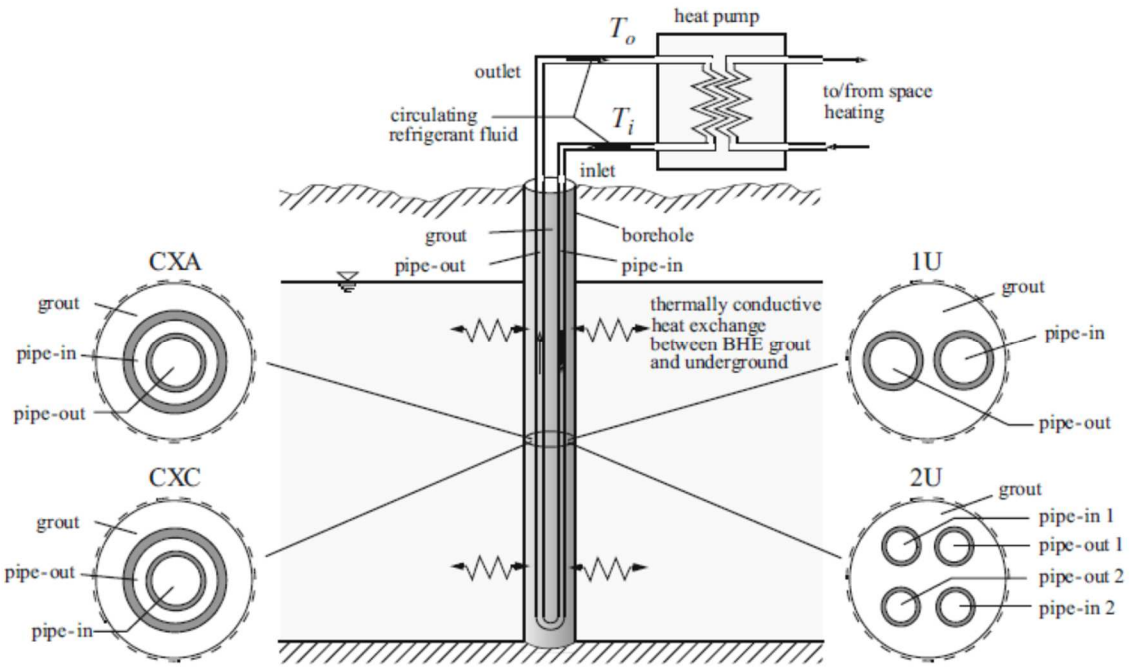

Figure 3.1. Different BHE configurations (Diersch, 2014) – T_i and T_o are refrigerant inlet and outlet temperature

An important modeling aspect is dealing with the unique geometry of the boreholes in FEFLOW. Boreholes have a unique slender body considering typical diameter of 0.13 m and typical length of 100 m (Banks, 2012). Combining this slender geometry with large temperature gradients in the vicinity of the boreholes demands a high-density mesh around the body of a borehole in finite element modeling to achieve reasonable results. Considering the long simulation periods of a geothermal heating systems, typically from 10 to 25 years, and relatively vast modeling domain with hundreds of meters, dealing with high density mesh calls for great computational efforts. Therefore, a common practice is to reduce the BHE body to a line and couple it with a 3D finite element model representing the subsurface known as dual-continuum approach (Diersch et al., 2011a, 2011b). In this practice, which is available in FEFLOW, BHEs are dealt with as an internal boundary condition and borehole wall temperature is utilized as a coupling parameter for two geometrically different domains. The dual-continuum approach results in two sets of global and local problems within subsurface and inside boreholes, respectively.

In FEFLOW, a borehole is discretized by 1D vertical pipe elements with N_{BHE} nodes inside a 3D domain with prism or tetrahedron elements as shown in Figure 3.2. Therefore, each BHE is considered a non-standard internal boundary condition known as well-type *singular point condition* (SPC). A mathematical model called *thermal resistance and capacity model* (TRCM) is then utilized to approximate the heat exchange between pipe and grout with thermal resistance and capacity elements to simulate transient heat transfer more accurately. As described in Figure 3.1, a 2U borehole has 4 pipes (2 inlets and 2 outlets) and 4 grout zones (one zone associated with each pipe). Therefore, each 2U element, has a total of 8 internal lines (4 pipes and 4 grouts) and 16 points as depicted in Figure 3.2. Note that i, o and g represent inlet, outlet and grout, respectively. FEFLOW solves the energy equation inside the boreholes (referred to as the local problem) to achieve boreholes surface temperature. This surface temperature is then imposed along the borehole line as an internal boundary condition for the rest of the subsurface (referred to as global problem).

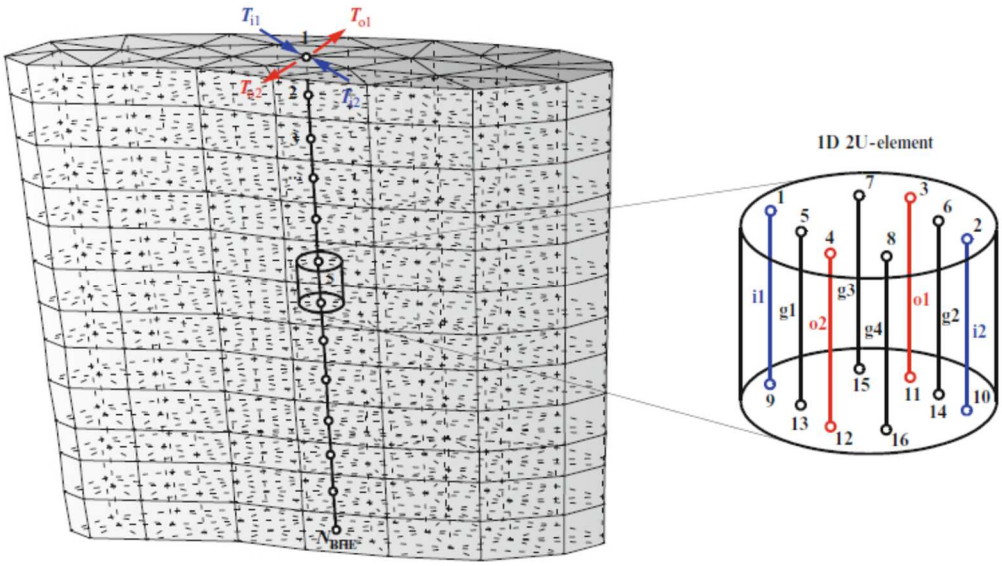

Figure 3.2. Discretized model of a 2U borehole heat exchanger (Diersch, 2014)

Solution to the local problem for such slender geometry of BHEs demands efficient numerical schemes. This can be performed in FEFLOW by two ways (Diersch, 2014):

- Analytical method (Eskilson and Claesson's solution)
- Numerical method (Al-Khoury et al.'s solution)

In analytical method, local steady-state conditions are assumed for inside the boreholes and thermal equilibrium is considered between inlet and outlet pipes. This method is proven to be accurate and robust but fails to predict short-term results. Al-Khoury et al.'s numerical method, on the other hand, is more complicated and is suitable for short-term and long-term simulations while it requires more computational effort (Diersch, 2014).

3.3. Case study

The case study for this project is an office building located in Toronto, Canada based on the model previously developed by (Daemi, 2017; Daemi & Krol, 2019). Specification of this building, called the "reference building", is presented in Table 3.1.

3.3.1. Thermal load calculation

To calculate the building heating and cooling loads, the yearly outdoor air temperature is needed which is shown in Table 3.2.

Table 3.1. Specification of case study building (Bhatia, 2014; Daemi, 2017)

Specification	Value
Type of building	Office
Number of floors (story)	3
Floor area	64 ft × 80 ft=5120 ft^2
Floor to floor height	12 ft
Wall Construction	
Face brick	4 in
Styrofoam insulation	2 in
Concrete block	8 in
Air space	1.5 in

Plaster board	0.5 in
Wall U-value	0.09 Btu/(hr.ft^2.°F)
North and South Facing Walls Area	2160 ft^2
East and West Facing Walls Area	1728 ft^2
Walls Area	7776 ft^2
Roof construction	
Tar and gravel (built-up)	0.375 in
Rigid insulation	2 in
Concrete	8 in
Air space	4 in
Acoustic tile	0.5 in
Roof U-value	0.04 Btu/(hr.ft^2.°F)
Roof Area	5120 ft^2
Windows	
Type	Double glazed
Windows U-value	0.7 Btu/(hr.ft^2.°F)
Windows Area (25% of wall)	2592 ft^2

Table 3.2. Average outdoor air temperature for Toronto in °C (*Canadian Climate Normals 1981-2010 Station Data*, 2020)

Month	**Jan**	**Feb**	**Mar**	**Apr**	**May**	**Jun**	**Jul**	**Aug**	**Sep**	**Oct**	**Nov**	**Dec**
Average Temperature	-5.5	-4.5	0.1	7.1	13.1	18.6	21.5	20.6	16.2	9.5	3.7	-2.2

Based on building specifications and outdoor air temperatures, total heating and cooling loads of the building is calculated and presented in Tables 3.3 and Figure 3.3. Note that the negative sign indicates a heating load. Details of load calculation can be found in (Daemi, 2017) based on the method proposed by American Society of Heating, Refrigerating and Air-Conditioning Engineers (ASHRAE).

Table 3.3. Total building thermal load in kW (Daemi, 2017)

Month	Jan	Feb	Mar	Apr	May	Jun	Jul	Aug	Sep	Oct	Nov	Dec
Thermal load	-84.3	-81	-64	-39.1	-17.6	69.9	91.5	84.6	-6.5	-30.5	-51.3	-72.4

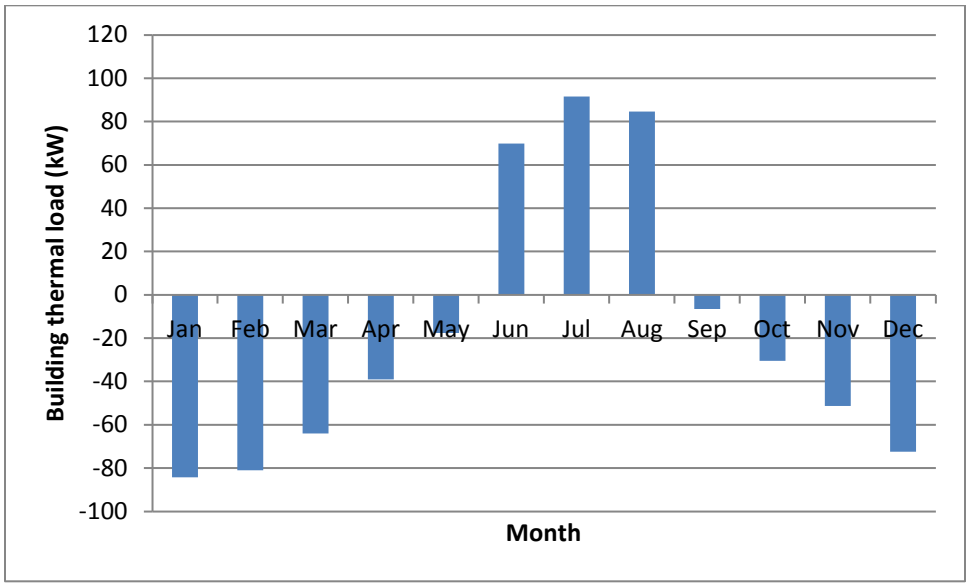

Figure 3.3. Building thermal load of the case study

The ground thermal load is calculated using the building load and entered as the load characteristic of BHEs in the FEFLOW simulation. This can be done by using equations (3-21) and (3-22) which correlate ground and building loads by coefficient of performance (COP) of the heat pump system (Banks, 2012).

$$G_H = H\left(1-\frac{1}{COP_H}\right) \tag{3-21}$$

$$G_C = C\left(1+\frac{1}{COP_C}\right) \tag{3-22}$$

where H and C are the building heating and cooling loads, respectively; G represents the ground thermal load and the subscript H and C denote heating and cooling, respectively. By assuming a

constant COP value of 4 as a common COP for both heating and cooling scenarios (Banks, 2012), we have:

$$G_H = \frac{3}{4}H \tag{3-23}$$

$$G_C = \frac{5}{4}C \tag{3-24}$$

Consequently, the ground thermal load is calculated from values of building thermal load using (3-23) and (3-24) and presented in Table 3.4 and Figure 3.4. As can be seen by Figure 3.4, five months of heating from January to May is followed by three months of cooling till August and finally another four months of heating from September to December.

Table 3.4. Total ground thermal load in kW (Daemi, 2017)

Month	Jan	Feb	Mar	Apr	May	Jun	Jul	Aug	Sep	Oct	Nov	Dec
Thermal load	-63.2	-60.5	-48.2	-29.3	-13.2	87.4	114.4	105.7	-4.8	-22.9	-38.5	-54.3

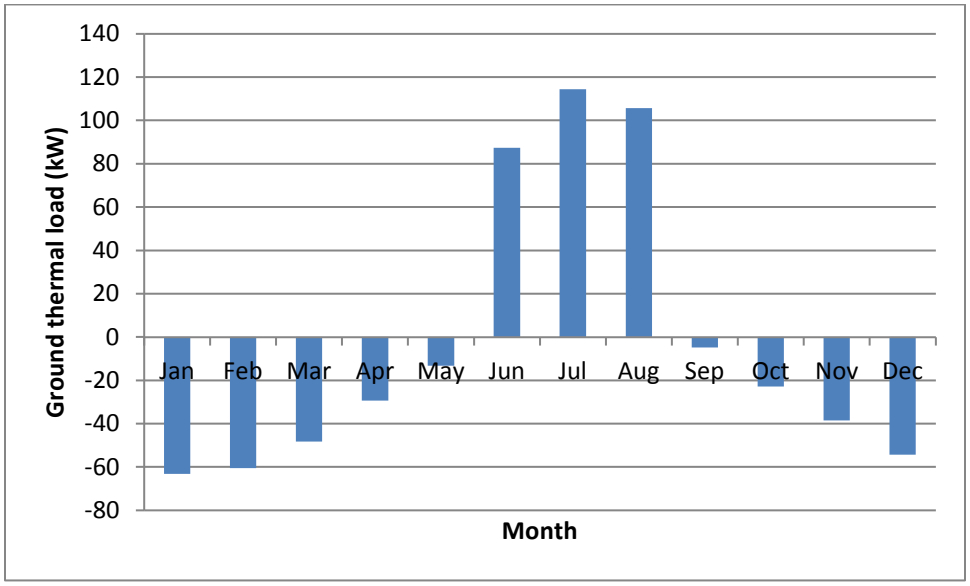

Figure 3.4. Ground thermal load for the case study

3.3.2. Sizing of the BHE system

The process of sizing of geothermal heating system in terms of borehole heat exchangers includes determination of borehole depth, number of BHEs, and the arrangement and spacing based on the calculated ground load. For closed-loop vertical systems, the common range for depth is between 40 to 200 m (Banks, 2012). The number of required boreholes can be evaluated from equation (3-25) with Q_{gr} as ground load (heating or cooling), q_b as specific heat extraction rate per drilled meter of borehole and D_b as borehole depth.

$$N = \frac{Q_{gr}}{q_b \times D_b} \tag{3-25}$$

Specific heat extraction rate is the amount of thermal energy abstracted from ground per drilled meter of a borehole which is dependent on the geology of the site. For medium conductivity strata with thermal conductivity between 1.5 and 3 $W.m^{-1}.K^{-1}$, the average specific heat extraction rate of 50 $W.m^{-1}$ is assumed based on the rule of thumb (Banks, 2012).

According to Table 3.4, peak ground load for Toronto is 114.4 kW for cooling in July and with addition of about 15% safety factor, a 130 kW load is used. By assuming 150 m as borehole depth, substitution of these values in (3-25) yields the number of required boreholes:

$$N = \frac{130 \times 1000}{50 \times 150} \approx 18 \tag{3-26}$$

The distance between boreholes are assumed to be 10 m to minimize the thermal interaction of the boreholes as suggested by others (Banks, 2012; Dehkordi et al., 2015; Hecht-méndez et al., 2013). Among many configurations available such as in-line, L-shape and rectangular arrangement, a 6×3 layout depicted in Figure 3.5 is chosen which is considered favorable for dual season application of a GSHP (Banks, 2012; Daemi, 2017).

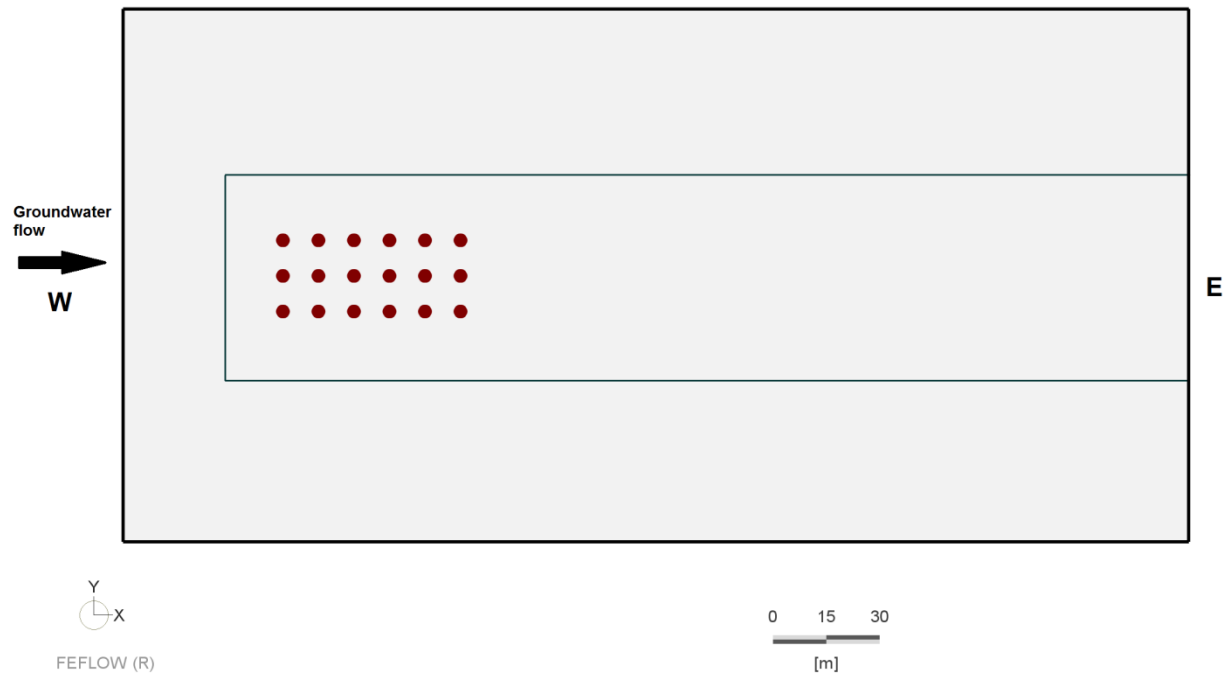

Figure 3.5. The rectangular 6×3 layout used as borehole arrangement

The model domain has 300x150x170 m, in the x, y, z dimensions respectively, in which the 18 boreholes are placed from top to the depth of 150 m as shown in Figure 3.6. The direction of groundwater flow is assumed to be from western to eastern boundaries.

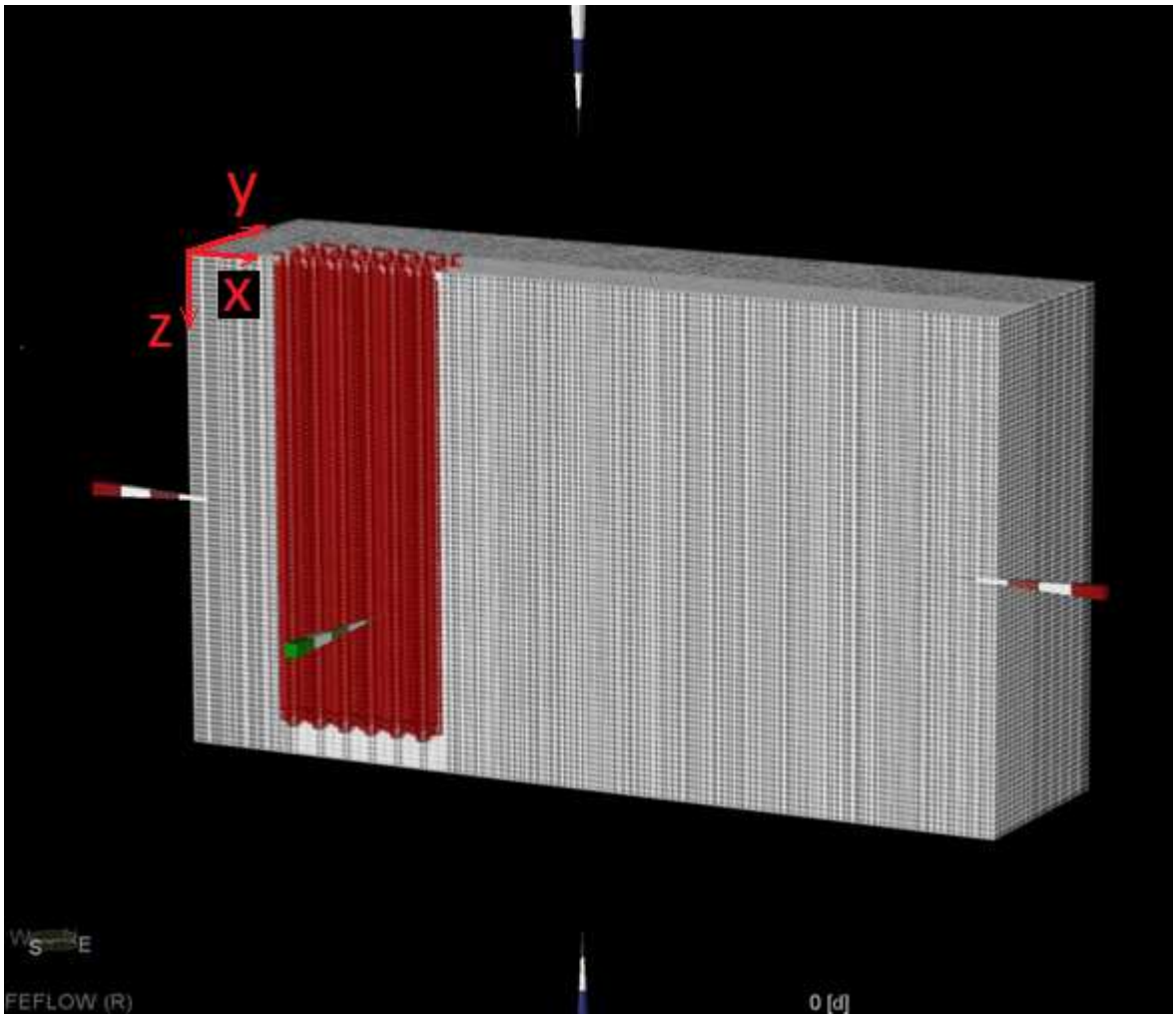

Figure 3.6. Mid-section view of the borefield; FEFLOW finite element model with 300x150x170 m, in the x, y, z direction, respectively

3.3.3. Simulation parameters and boundary conditions

The simulated borefield is assumed to be located in a saturated, homogeneous, and isotropic sandy aquifer located in the Toronto area with hydraulic conductivity of 7.3×10^{-5} $m.s^{-1}$ (6.31 $m.d^{-1}$) based on the model utilized by Daemi, (2017) and Daemi and Krol, (2019). This value is also in compliance with the range of hydraulic conductivities for fine to medium sands (Domenico & Schwartz, 1997). Soil thermal conductivity is taken as 2 $W.m^{-1}.K^{-1}$ from the range reported for saturated sand (Luo et al., 2016). Water thermal conductivity is assumed as 0.6 $W.m^{-1}.K^{-1}$ (*The Enginnering Toolbox - Water - Thermal Conductivity*, 2020). For volumetric heat capacity of the

wet soil and water, the values of 2.2×10^6 and 4.2×10^6 $J.m^{-3}.K^{-1}$ are taken, respectively (*The Enginnering Toolbox - Specific Heat of Some Common Substances*, 2020). The above mentioned values are also in agreement with the ranges reported by Dehkordi and Schincariol, (2014). Moreover, longitudinal and transverse thermo-dispersivities and porosity values are assumed to be as 0.5 m, 0.05 m and 0.3, respectively from Dehkordi and Schincariol, (2014).

A double U-tube (2U) heat exchanger with 15 cm diameter was used from the FEFLOW library, using the default parameters. The computational method is set to fully transient, also known as Al-Khoury et al.'s numerical solution (Diersch, 2014). Total refrigerant flow rate is taken as 0.0072 $m^3.s^{-1}$ (622 $m^3.d^{-1}$) from previous works done by Daemi, (2017) and Daemi and Krol, (2019). The background subsurface temperature is set to 10°C as the initial condition. Table 3.5 shows boundary conditions applied to the confined aquifer model.

Table 3.5. Boundary conditions applied to the model

Condition	Value	Unit
Head at western boundary	0	m
Head at eastern boundary	-0.03	m
No flow conditions at north and south boundaries	-	-
Adiabatic conditions at north and south boundaries	-	-
Temperature at top boundary	Variable according to Table 3.2	°C
Input power in boreholes	Variable according to Table 3.4	kW

For contaminant transport simulation, diffusion coefficient for benzene and toluene at 10°Cis estimated from EPA online calculator (*EPA On-Line Tools for Site Assessment Calculation - Diffusion Coefficient*, 2020) as 7×10^{-10} $m^2.s^{-1}$ and 6×10^{-10} $m^2.s^{-1}$, respectively. Dispersivity is estimated from Xu and Eckstein equation which is a nonlinear relationship based on a regression analysis (Fetter, 2008) presented in equation (3-27) with L_s as length scale:

$$\beta_L = 0.83\left(\log L_s\right)^{2.414} \tag{3-27}$$

By substitution of 300 m as length scale, the longitudinal dispersivity is calculated as 7.4 m and transverse dispersivity is then taken as 10% of the longitudinal dispersivity (Fetter, 2008) .The required flow and transport parameters are gathered in Table 3.6.

Table 3.6. Summary of required parameters for flow and transport simulation

Quantity	**Symbol**	**Value**	**Unit**
Hydraulic conductivity [(a)]	K	6.31	$m.d^{-1}$
Depth of borehole	D	150	m
Borehole diameter	$2r_b$	0.15	m
U-tube diameter	$2r_U$	32	mm
Pipes wall thickness	b	2.9	mm
Pipe distance	w	40	mm
Thermal conductivities of pipe walls	λ_π	0.42	$W.m^{-1}.K^{-1}$
Total refrigerant flow rate [(a)]	Q_r	622	$m^3.d^{-1}$
Refrigerant volumetric heat capacity	$\rho_r c_r$	4×10^6	$J.m^{-3}.K^{-1}$
Refrigerant thermal conductivity	λ_r	0.48	$W.m^{-1}.K^{-1}$
Refrigerant dynamic viscosity	μ_r	3×10^{-3}	$Kg.m^{-1}.s^{-1}$
Refrigerant density	ρ_r	1052	$Kg.m^{-3}$
Grout volumetric heat capacity	$\rho_g c_g$	2.5×10^6	$J.m^{-3}.K^{-1}$
Grout thermal conductivity	λ_g	1	$W.m^{-1}.K^{-1}$
Water volumetric heat capacity [(b)]	$\rho_w c_w$	4.2×10^6	$J.m^{-3}.K^{-1}$
Solid matrix volumetric heat capacity [(b)]	$\rho_s c_s$	2.2×10^6	$J.m^{-3}.K^{-1}$
Water thermal conductivity [(c)]	λ_w	0.6	$W.m^{-1}.K^{-1}$
Solid matrix thermal conductivity [(d)]	λ_s	2	$W.m^{-1}.K^{-1}$
Longitudinal thermodispersivity [(e)]	α_L	0.5	m
Transverse thermodispersivity [(e)]	α_T	0.05	m
Porosity	ε	0.3	-
Initial temperature	T_0	10	°C
Diffusion coefficient [(f)]	D_d	7×10^{-10} (benzene)	$m^2.s^{-1}$

		6×10^{-10} (toluene)	
Longitudinal dispersivity [g]	β_L	7.4	m
Transverse dispersivity	β_T	0.74	m

[a] Taken from Daemi and Krol, (2019)
[b] Taken from *The Enginnering Toolbox - Specific Heat of some common Substances*, (2020)
[c] Taken from *The Enginnering Toolbox- Water - Thermal Conductivity*, (2020)
[d] Taken from Luo *et al.*, (2016)
[e] Taken from Dehkordi and Schincariol, (2014)
[f] Taken from *EPA On-line Tools for Site Assessment Calculation - Diffusion Coefficient*, (2020)
[g] Calculated from equation (3-27)

3.3.4. BHE grid size selection and array setup

In FEFLOW, borehole heat exchangers are modeled as a singular internal boundary condition by a 1D line element. This line element, however, represents a 3D borehole object including pipes and grout material. This unique characteristic requires an optimal mesh density around the immediate vicinity of the borehole to achieve good accuracy.

A simple method for direct estimation of nodal distance around the BHEs (distance between the center of the BHE to the adjacent node) can be implemented in finite element discretization according to Figure 3.7. In this figure, n is number of neighboring nodes, Δ represents the nodal distance while r_b is borehole physical radius. Since FEFLOW uses triangular elements, n parameter is usually set to 4, 6 or 8. It has been shown that satisfaction of equation (3-28) leads to optimal mesh refinement around the BHE node with best accurate results and thus eliminate the need for finer mesh (Diersch, 2014).

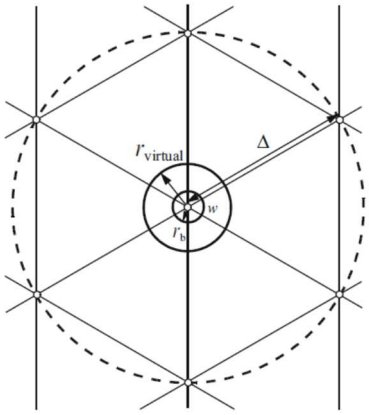

Figure 3.7. Spatial discretization around a BHE

$$\Delta = a.r_b \qquad \begin{cases} a=4.81 \text{ for } n=4 \\ a=6.13 \text{ for } n=6 \\ a=6.66 \text{ for } n=8 \end{cases} \tag{3-28}$$

For this study, r_b = 0.15/2 and n=6 thus the optimal nodal distance in the immediate vicinity of the boreholes is calculated as 0.46 m. This value is set as the geometric constraint around the BHE central node during mesh generation while a gradual transition to a coarser mesh is allowed which is described in a mesh convergence study in section 3.5.

In the BHE array setup, boreholes are interconnected in a parallel array configuration in which the inlet flow is guided to all 18 boreholes and then collected from all the BHEs in the outlet as depicted in Figure 3.8. Moreover, the flow rate of the refrigerant in each pipe is selected in a way that yields a turbulent flow to achieve a good heat transfer coefficient. Total refrigerant flow rate is taken as 622 $m^3.d^{-1}$ (Daemi, 2017; Daemi & Krol, 2019). To complete the setup of BHE arrays, input power should be assigned which is equal to the variable ground load introduced in Table 3.4.

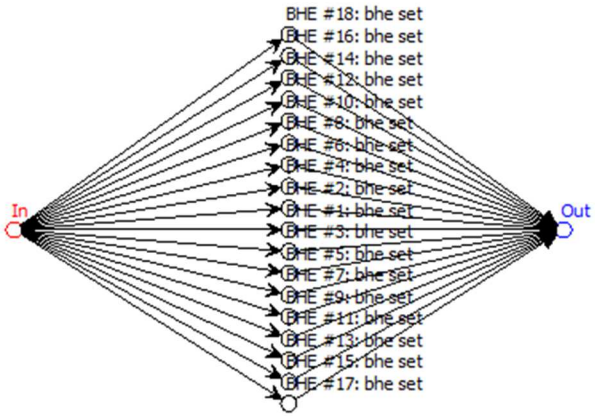

Figure 3.8. BHE parallel array configuration

3.4. Benchmark example

In numerical simulations, benchmarking helps to evaluate the model setup as part of model verification process. Therefore, a single BHE was used with 2U pipe configuration and constant input power located in the center of a 20×20×55m domain, based on a benchmark example presented by Diersch, (2014). In his book, Diersch modeled the 2U BHE in FEFLOW with 1D line element and compared the results with a fully discretized 3D model solution (FD3DM) which is depicted in Figure 3.9. The huge difference in grid element requirements between fully discretized 3D model solution (FD3DM) and dual continuum approach with 1D line elements is contrasted in this figure.

No flow and adiabatic boundary condition were applied to north and south boundaries while for the west and east boundaries, the hydraulic heads were set to 0 m and -0.02 m, respectively. Required physical parameters for 2U BHE are presented in Table 3.7. Based on these parameters, a model with 97,000 elements was prepared in FEFLOW and is depicted in Figure 3.10. The results of this model for the short-term (90 minutes) and long-term (180 days) simulation was compared with the results reported by (Diersch, 2014) and seen in Figures 3.11 and 3.12, respectively. In these figures, analytical refers to quasi-steady Eskilson and Claesson's solution whereas numerical method represents fully transient Al-Khoury et al.'s solution.

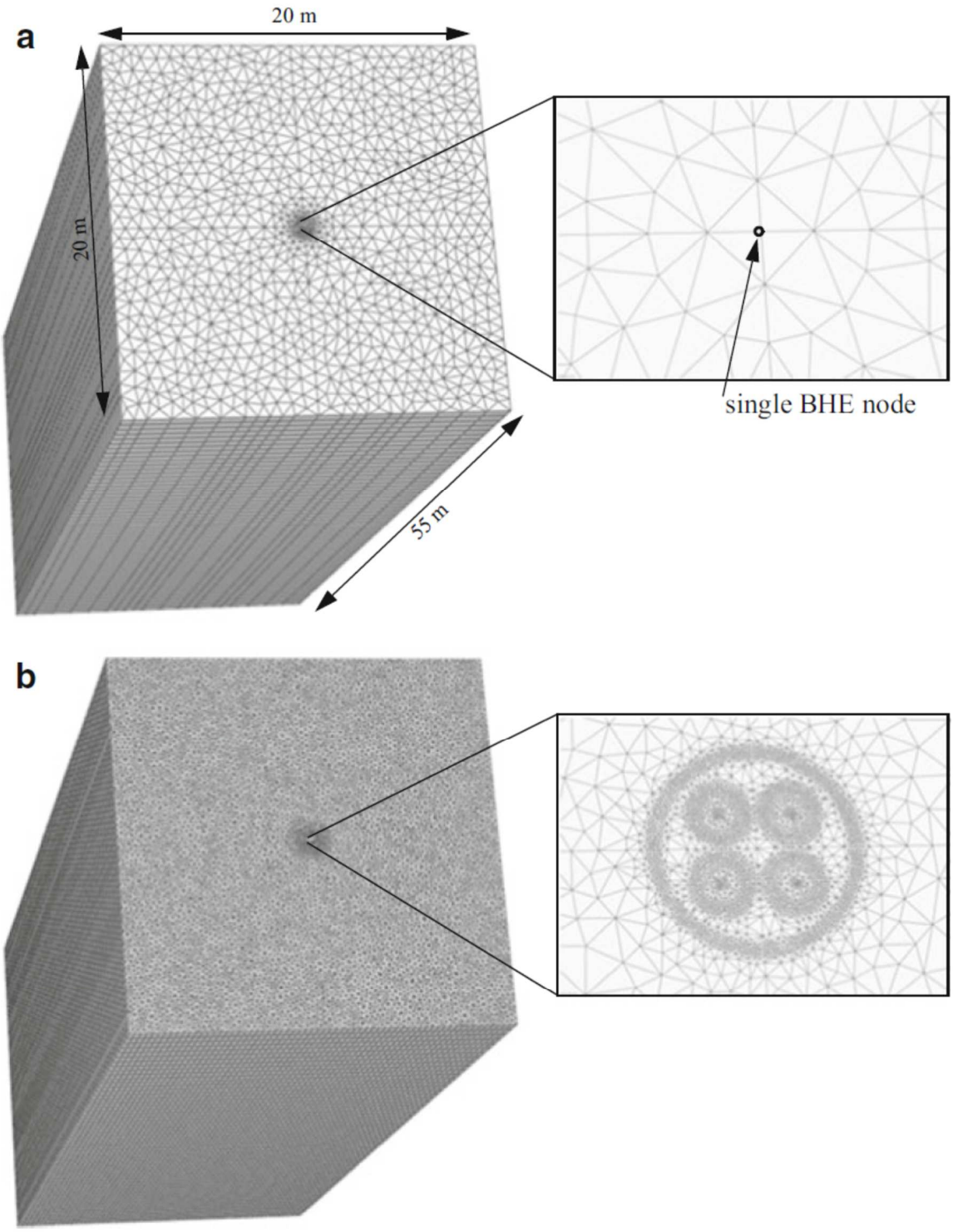

Figure 3.9. Finite element meshes for the 2U BHE as a single node (a) and FD3DM (b) (Diersch, 2014)

Table 3.7. Physical properties of the 2U benchmark BHE

Quantity	Symbol	Value	Unit
Depth of borehole	D	55	m
Borehole diameter	$2r_b$	0.12	m
U-tube diameter	$2r_U$	32	mm
Pipes wall thickness	b	2.9	mm
Pipe distance	w	42	mm
Thermal conductivities of pipe walls	λ_π	0.38	$W.m^{-1}.K^{-1}$
Total heat extraction rate	Q	6.322×10^{9}	$J.d^{-1}$
Refrigerant flowrate	Q_r	38.28	$m^3.d^{-1}$
Refrigerant volumetric heat capacity	$\rho_r c_r$	4.13×10^{6}	$J.m^{-3}.K^{-1}$
Refrigerant thermal conductivity	λ_r	0.65	$W.m^{-1}.K^{-1}$
Refrigerant dynamic viscosity	μ_r	0.52×10^{-3}	$Kg.m^{-1}.s^{-1}$
Refrigerant density	ρ_r	938	$Kg.m^{-3}$
Grout volumetric heat capacity	$\rho_g c_g$	2.19×10^{6}	$J.m^{-3}.K^{-1}$
Grout thermal conductivity	λ_g	2.3	$W.m^{-1}.K^{-1}$
Water volumetric heat capacity	$\rho_w c_w$	4.2×10^{6}	$J.m^{-3}.K^{-1}$
Solid matrix volumetric heat capacity	$\rho_s c_s$	2.4×10^{6}	$J.m^{-3}.K^{-1}$
Water thermal conductivity	λ_w	0.65	$W.m^{-1}.K^{-1}$
Solid matrix thermal conductivity	λ_s	2.46	$W.m^{-1}.K^{-1}$
Anisotropy factor of soil	Ξ_{aniso}	1	-
Longitudinal thermodispersivity	α_L	0.5	m
Transverse thermodispersivity	α_T	0.05	m
Porosity	ε	0.2	-
Initial temperature	T_0	10	°C
BHE inlet temperature	T_{inlet}	50	°C

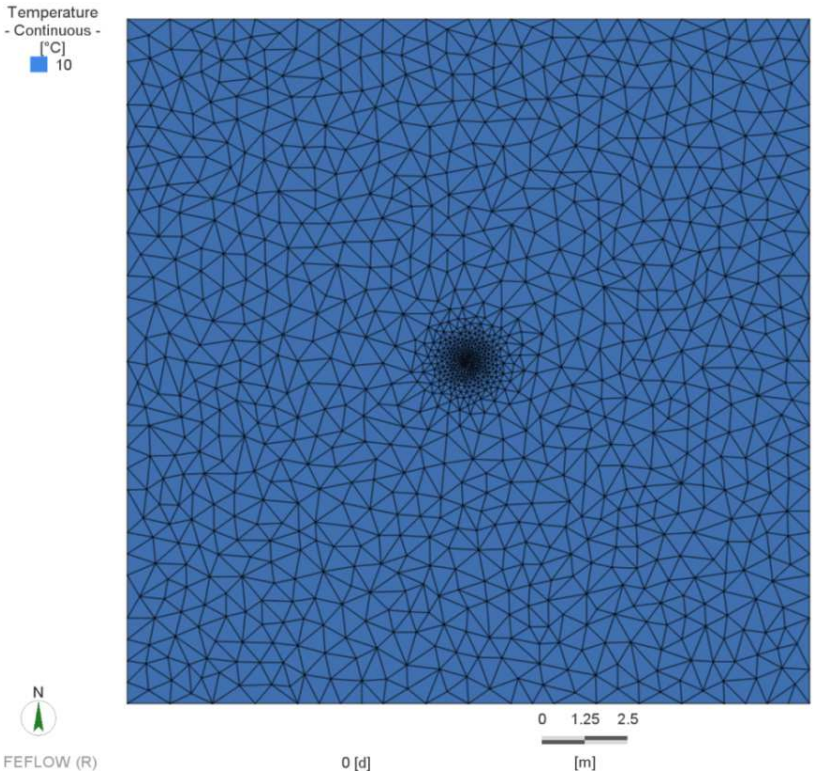

Figure 3.10. Finite element model of benchmark 2U BHE

The comparison plotted in Figure 3.11, shows that the analytical method overestimates the outlet temperature of the borehole in earlier times, but gets compatible with numerical method results after a few minutes (15 min). The fully discretized 3D model (FD3DM) has the most reliable results but it is computationally expensive. The results of the model used in this study is the fully transient solution, labeled as BHE numerical, is in fair agreement with the results obtained from (Diersch, 2014). Long-term quasi-steady results, labeled as BHE analytical, compared with benchmark example from (Diersch, 2014) in Figure 3.12, also demonstrate reasonable accuracy of this method.

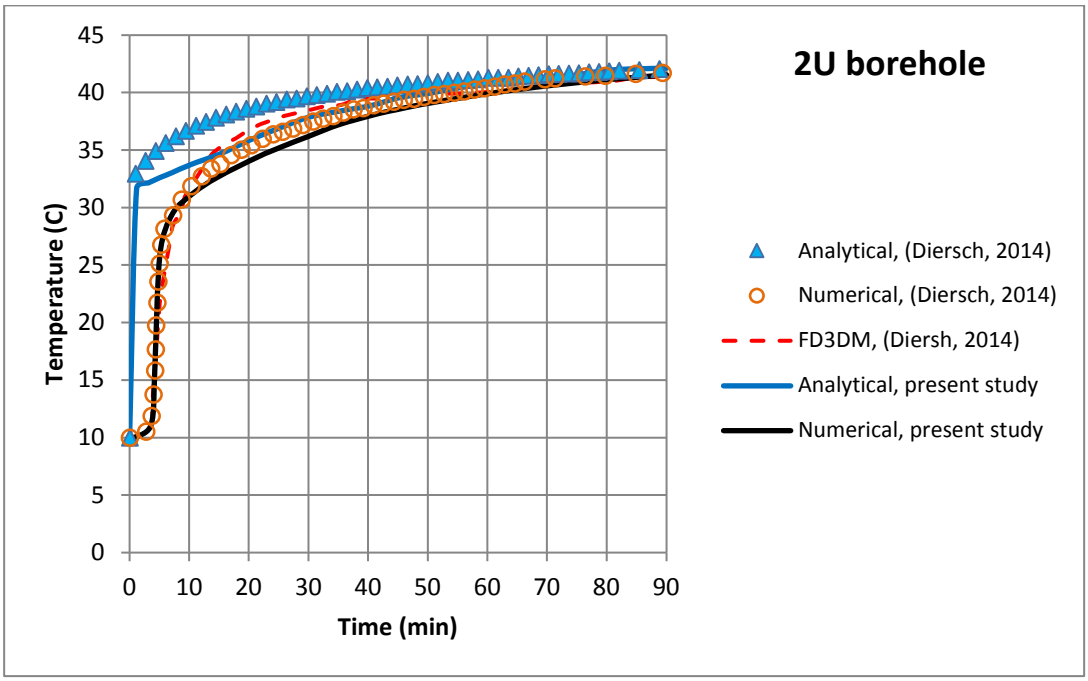

Figure 3.11. Comparison of short-term outlet temperature history of 2U BHE with results reported by Diersch, (2014)

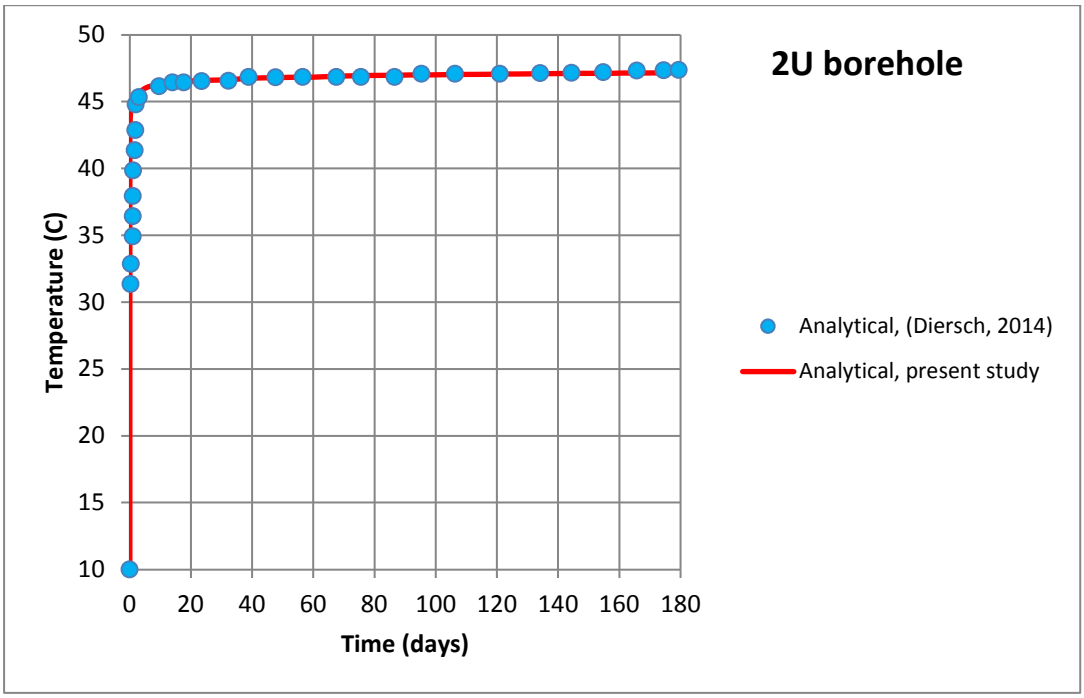

Figure 3.12. Comparison of long-term outlet temperature history of 2U BHE with results reported by Diersch, (2014)

3.5. Mesh convergence study and heat transport model verification

A common practice in finite element analysis to ensure model verification is to perform a mesh convergence study. A more finely discretized model will result in higher accuracy but at a higher computational time, therefore there is a trade-off with computational time and model accuracy. In a mesh convergence study, the mesh is refined until there is minimal change in the solution. Since the gradient of temperature is higher around the boreholes and in the direction of ground water flow, finer grid size is implemented in that area.

Based on the simulation parameter introduced in section 3.3.3 and boundary conditions in Table 3.5, six scenarios were modeled with increasing number of elements with different grid size and the nodal distance as 0.46 m at the immediate vicinity of the boreholes as calculated from equation (3-28). Model specification is reported in Table 3.8 and Figure 3.13 shows the top view of the mesh for comparison.

Table 3.8. Specification of 6 finite element models used for mesh convergence study

Model	Proposed elements in supermesh	Number of elements per layer	Number of layers	Total number of elements (x1000)
1	1000	5036	85	428
2	2000	6421	85	545
3	3000	8139	85	692
4	4000	9610	85	817
5	5000	11143	85	947
6	6000	12460	85	1059

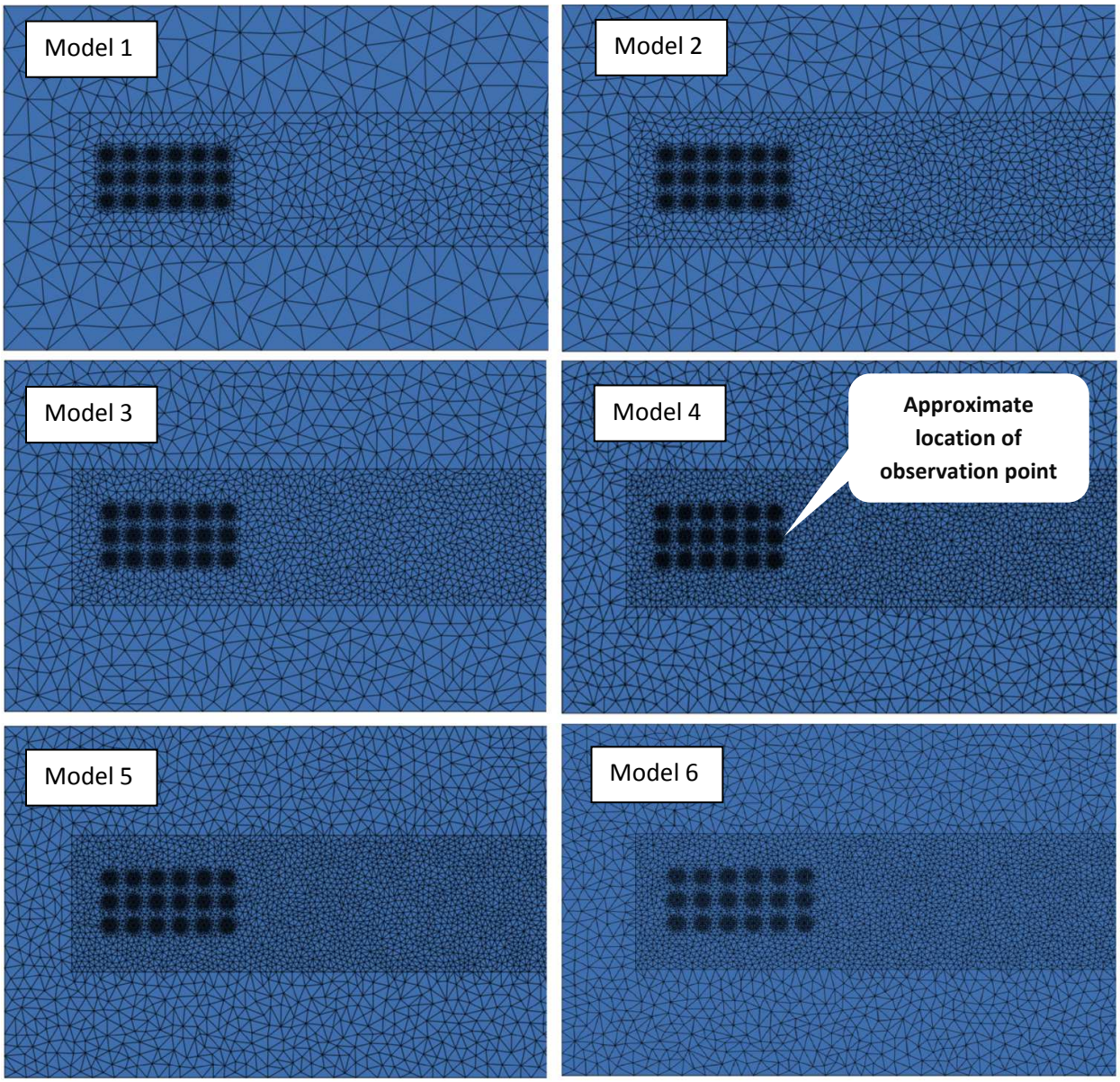

Figure 3.13. Top view of the various mesh configurations for the mesh convergence study and approximate location of observation point

The various scenarios were simulated for 30 days under transient heat and an observation point located 0.46m downstream of the last BHE column in the top layer (Figures 3.13 and 3.14) was used to evaluate the temperature, shown in Figure 3.15. It can be seen that as the number of elements increased, the temperature converged. As such, convergence was achieved using 5000 proposed elements per layer and 947000 total elements (model 5). The relative error for all 6

models with respect to the temperature achieved with the finest mesh as reference value (T_{ref}), is presented in Table 3.9. Therefore, the final 3D finite element model presented in Figure 3.16 consists of 85 layers, 18 boreholes, 947,155 triangular prism elements and 485,212 nodes.

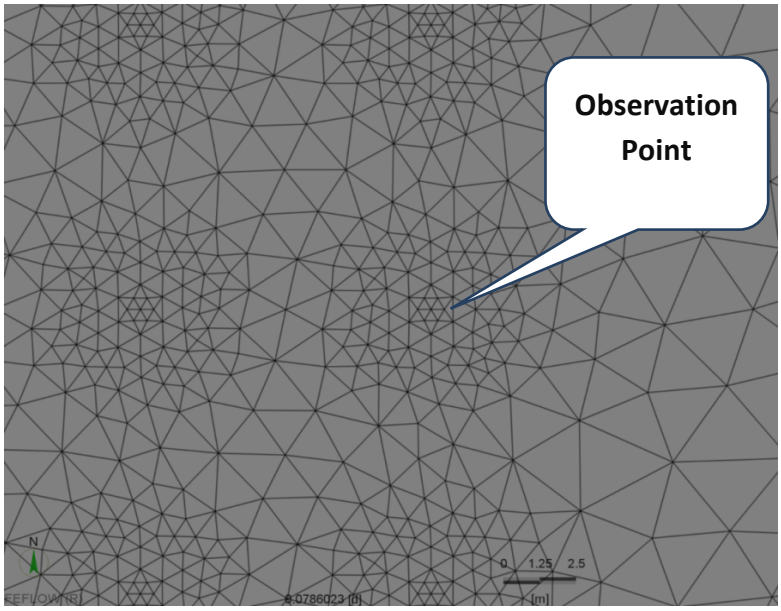

Figure 3.14. Location of the observation point

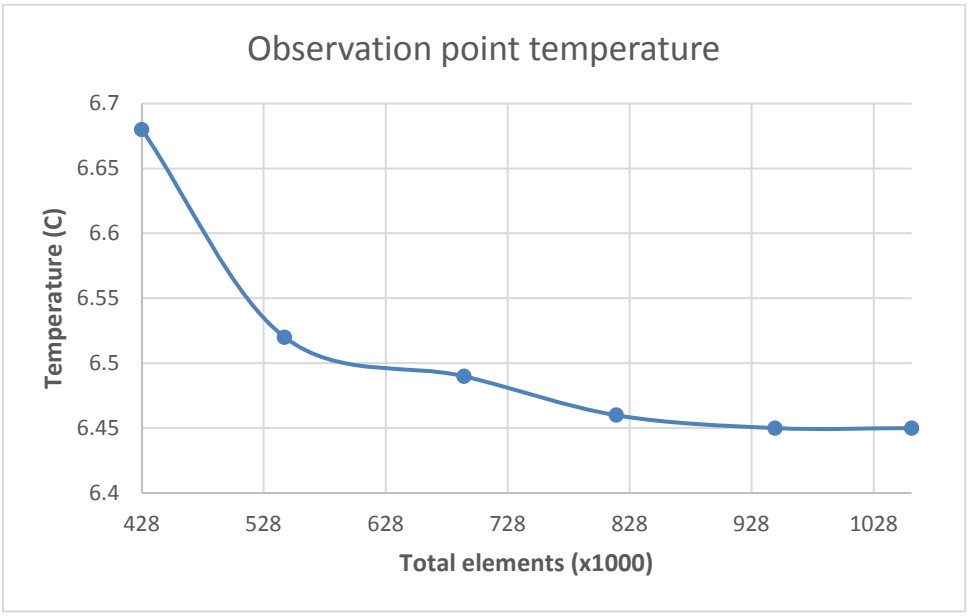

Figure 3.15. Temperature result for observation point after 30 days of simulation

Table 3.9. Relative error for 6 models used in mesh convergence study

Model	Total number of elements (x1000)	Temperature at observation point (°C)	Relative error (%) $Error = \frac{T - T_{ref}}{T_{ref}} \times 100$
1	428	6.68	3.6
2	545	6.52	1.1
3	692	6.49	0.6
4	817	6.46	0.2
5	947	6.45	0
6	1059	6.45	0

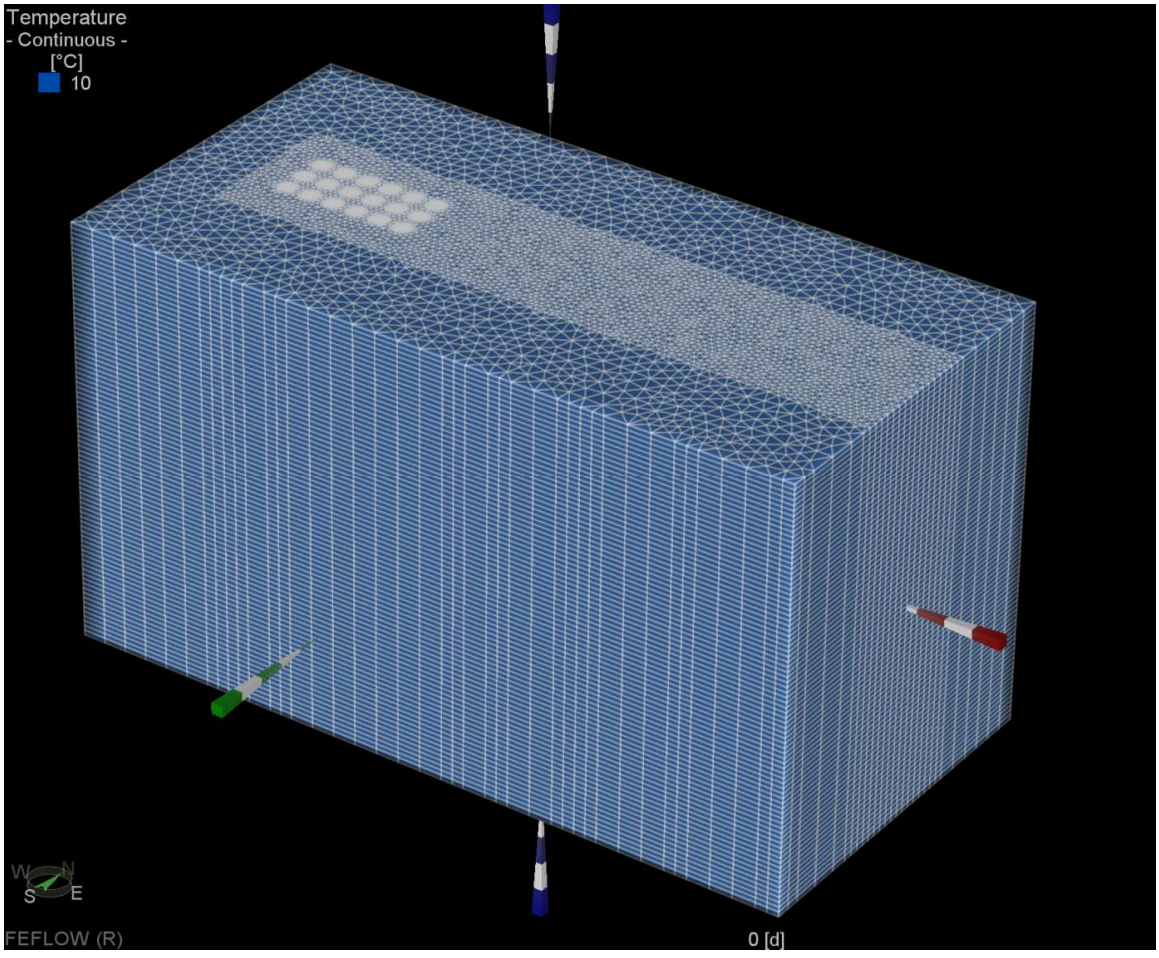

Figure 3.16.3D finite element model with 947k elements and 18 boreholes

3.6. Model validation with analytical solution for contaminant transport

Although no closed-form analytical solution is available for the 3D heat transport in porous medium with borehole heat exchangers, the slug injection with concentration of C_0 and volume of V_0, can be used to evaluate the 3D advective-dispersive transport equation in this study. The concentration of the mass for such a case is given as (Reddy & Inyang, 2000):

$$C\left(x,y,z,t\right)=\frac{M}{8\left(\pi t\right)^{\frac{3}{2}}\left(D_x D_y D_z\right)^{\frac{1}{2}}}\times\exp\left(-\frac{\left(x-vt\right)^2}{4D_x t}-\frac{y^2}{4D_y t}-\frac{z^2}{4D_z t}-\vartheta t\right) \tag{3-29}$$

where t, v and D denote time, linear (seepage) velocity and hydrodynamic dispersion coefficient, respectively. ϑ is first-order decay constant and $M=C_0V_0$ represent total mass of spill.

Seepage velocity is derived from division of Darcy flux by porosity and hydrodynamic dispersion coefficient can be calculated from molecular diffusion coefficient $\left(D_d\right)$, dispersivity factor $\left(\beta\right)$ and seepage velocity $\left(v\right)$ as:

$$D = D_d + \beta v \tag{3-30}$$

For simulation of an instantaneous spill of benzene in subsurface, 3D finite element model presented in Figure 3.16 with the boundary condition and model specification introduced in Table 3.5 and Table 3.6 was used. The hydraulic gradient, Darcy flux, seepage velocity and longitudinal hydrodynamic dispersion are calculated as follows:

$$i=\frac{h_2-h_1}{x}=\frac{-0.3-0}{300}=-0.001 \qquad \left(-\right) \tag{3-31}$$

$$q=-Ki=-7.3\times10^{-5}\times\left(-0.001\right)=7.3\times10^{-8} \qquad \left(ms^{-1}\right) \tag{3-32}$$

$$v=\frac{q}{\varepsilon}=\frac{7.3\times10^{-8}}{0.3}=2.43\times10^{-7} \qquad \left(ms^{-1}\right) \tag{3-33}$$

$$D = D_d + \beta v = 7\times10^{-9} + 7.4\times2.43\times10^{-7} = 1.81\times10^{-6} \quad \left(m^2 s^{-1}\right) \tag{3-34}$$

The benzene spill is modeled with an initial concentration of 100 mg.L^{-1} located at nodes around borehole number 9 (Figure 3.5) at a depth of 28 to 32 mbgs. Top view of the initial concentration at the slice located at 30 mbgs, is shown in Figure 3.17.

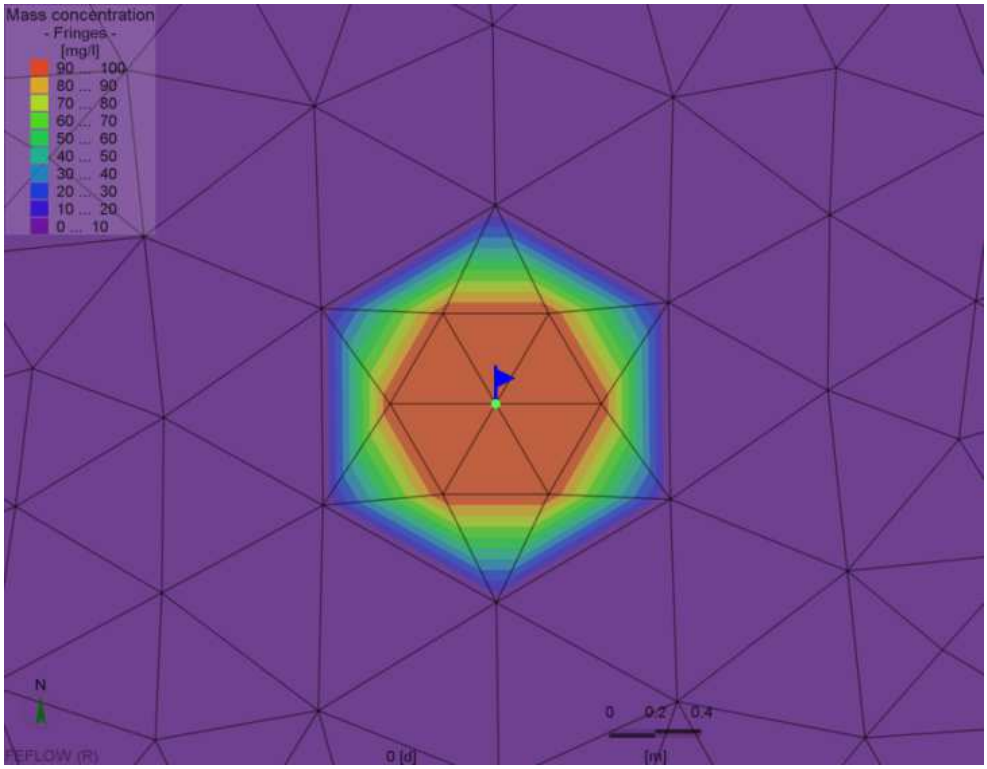

Figure 3.17. Spill of benzene with 100 mg.L^{-1} initial concentration in the model, depth = 30 mbgs

The values used in equation (3-29) and (3-10) are gathered in Table 3.10. A transient non-reactive mass transport simulation (without any decay or sorption) coupled with steady flow with boundary conditions introduced in Table 3.5 was performed in FEFLOW and Figure 3.18 shows the concentration after 365 days.

Table 3.10. Parameters used in non-reactive contaminant transport test for model validation

Quantity	Symbol	Value	Unit
Mass	M	0.615	kg
Hydraulic gradient	i	-0.001	-
Darcy flux	q	7.3×10^{-8}	$m.s^{-1}$
Porosity	ε	0.3	-
Linear velocity	v	2.43×10^{-7}	$m.s^{-1}$
Longitudinal dispersivity	β_L	7.4	m
Transverse dispersivity	β_L	0.74	m
Diffusivity	D_d	7×10^{-9}	$m^2.s^{-1}$
Longitudinal dispersion coefficient	D_x	1.81×10^{-6}	$m^2.s^{-1}$
Transverse dispersion coefficient	D_y , D_z	1.81×10^{-7}	$m^2.s^{-1}$
First-order decay constant	ϑ	0	s^{-1}

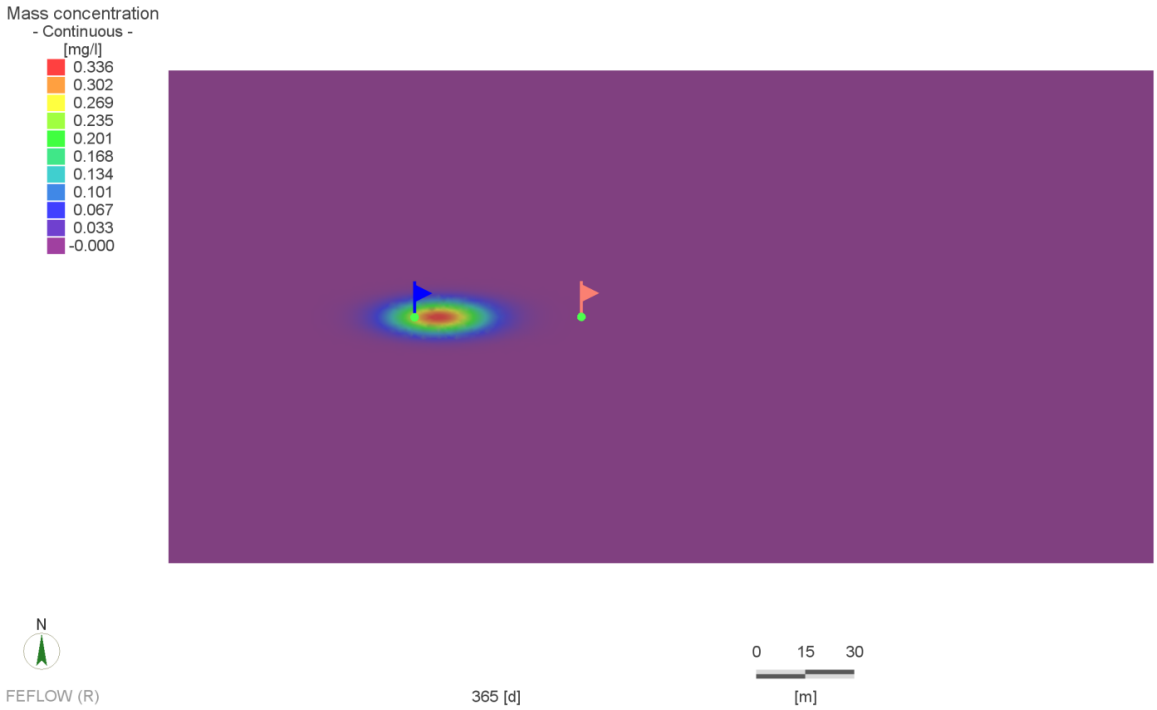

Figure 3.18. Benzene concentration after 365 days

For comparison purposes, the result of numerical simulation in the form of a breakthrough curve was viewed along a line specified with two flags in the Figure 3.18. The blue flag shows the start point at the center of initial spill which coincides with the center node of borehole number 9 and the red flag shows a point at 50 m distance in the flow direction (both at the depth of 30 mbgs). Numerical results are compared to the analytical solution given by equation (3-29) and shown in Figure 3.19. Although the results are in good agreement with the analytical solution, some difference is seen with the maximum relative error calculated as 6.7%. This variation is believed to be due to the nature of how initial concentrations are inputted into FEFLOW. FEFLOW only accepts initial concentration rather than mass and therefore the value of total mass for analytical solution is approximated by multiplication of concentration and volume derived from FEFLOW concentration isolines such as the one depicted in Figure 3.20. Thereby, the uncertainty in amount of calculated mass could be a source of error. Moreover, a period budget analysis of model showed mass imbalance of -1.12×10^{-6} g over 365 days, which is adequately low implying verification of the finite element model.

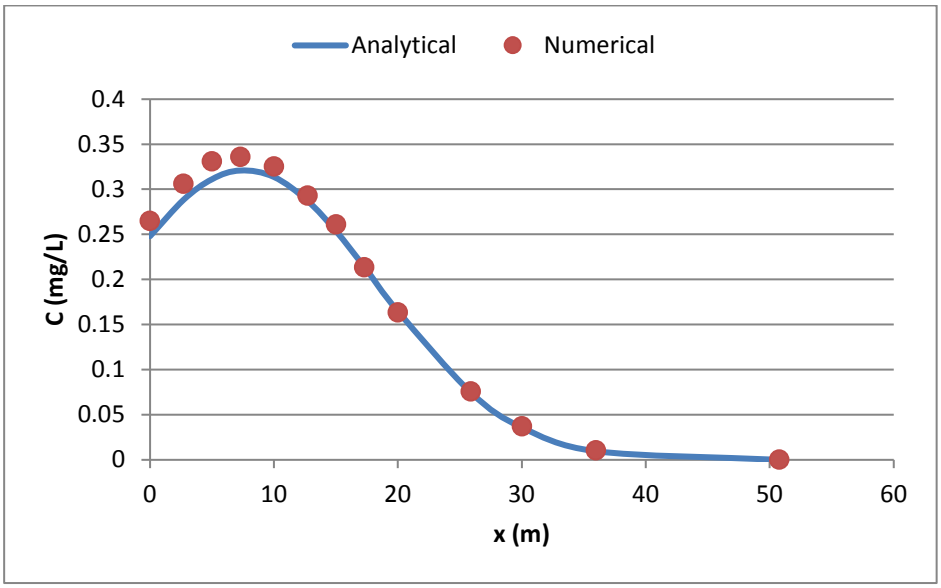

Figure 3.19. Comparison of breakthrough curves for analytical and numerical non-reactive transport simulation after 365 days

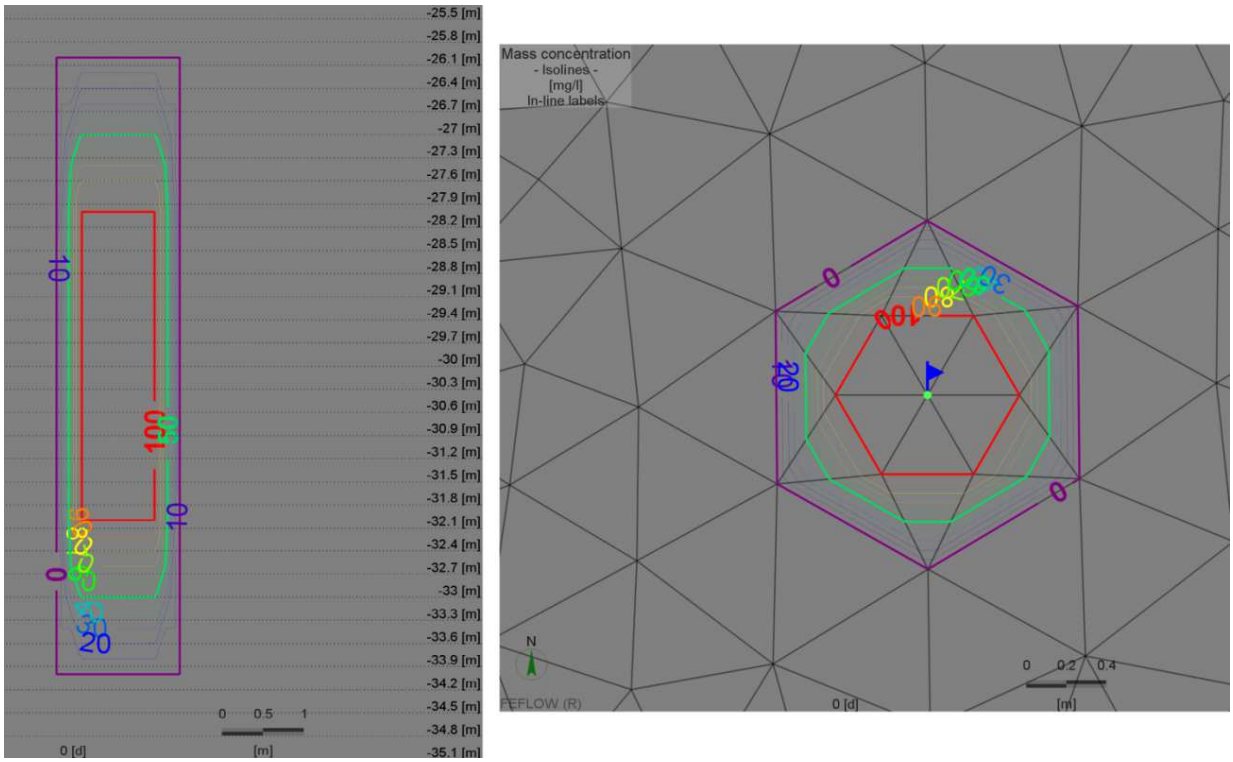

Figure 3.20. Concentration isolines in cross section view (left) and slice view (right)

As the second case for validation, a linear sorption model is implemented with linear sorption coefficient (k) set to 0.2 and soil particle density (ρ_s) as 2.65 kg.L^{-1}. Using equation (3-11) leads to calculation of distribution coefficient (k_d) as 0.075 L.kg^{-1}. Consequently, retardation factor can be calculated from equation (3-13):

$$R = 1 + \frac{(1-\varepsilon)}{\varepsilon}\rho_s k_d = 1 + \frac{(1-0.3)}{0.3} \times 2.65 \times 0.075 = 1.46 \qquad (3\text{-}35)$$

These values of velocity and dispersion coefficients are divided by retardation factor and equation (3-29) is compared to the simulations. The required parameters for analytical solution with retardation are gathered in Table 3.11.

Table 3.11. Parameters used in contaminant transport test with sorption for model validation

Quantity	Symbol	Value	Unit
Mass	M	0.615	kg
Hydraulic gradient	i	-0.001	-
Darcy flux	q	7.3×10^{-8}	$m.s^{-1}$
Porosity	ε	0.3	-
Retardation factor	R	1.46	-
Linear velocity	v	2.43×10^{-7}	$m.s^{-1}$
Retarded linear velocity	v_R	1.66×10^{-7}	$m.s^{-1}$
Longitudinal dispersivity	β_L	7.4	m
Transverse dispersivity	β_L	0.74	m
Diffusivity	D_d	7×10^{-9}	$m^2.s^{-1}$
Longitudinal dispersion coefficient	D_x	1.81×10^{-6}	$m^2.s$
Retarded longitudinal dispersion coefficient	D_{xR}	1.24×10^{-6}	$m^2.s$
Transverse dispersion coefficient	D_y , D_z	1.81×10^{-7}	$m^2.s$
Retarded transverse dispersion coefficient	D_{yR}, D_{zR}	1.26×10^{-7}	$m^2.s$
First-order decay constant	ϑ	0	s^{-1}

Breakthrough curve comparison for sorbed contaminant from numerical simulation and analytical solution is plotted in Figure 3.21 with maximum relative error calculated as 7.6% which shows a fair agreement for model validation purpose.

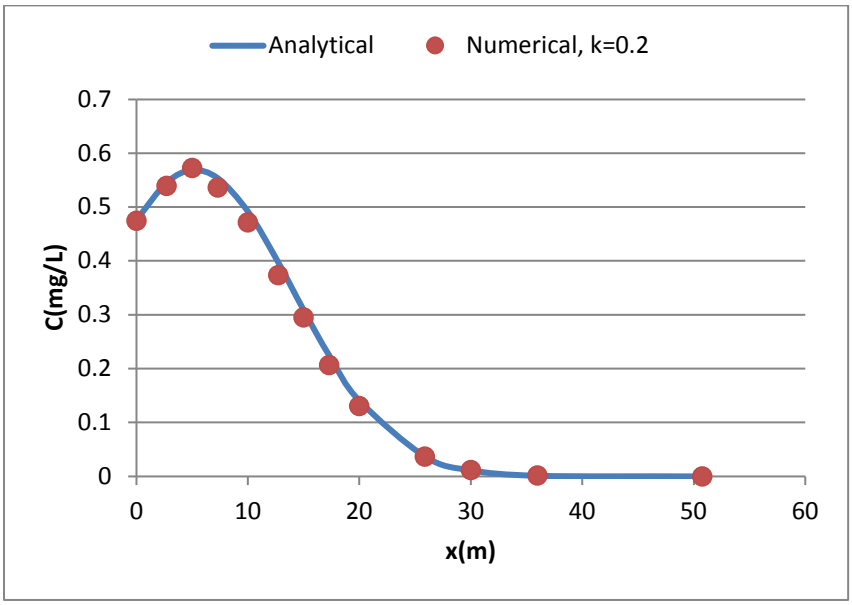

Figure 3.21. Comparison of breakthrough curves for analytical and numerical transport simulation with sorption after 365 days

3.7. Change in density and viscosity with temperature

Fluid viscosity varies with temperature in the model as shown in equations (3-2) to (3-4), which in turn leads to changes in hydraulic conductivity and Darcy flux. FEFLOW does not consider viscosity changes by default and the user needs to activate the option for variable viscosity via transport setting menu. Inclusion of viscosity dependencies in the simulation results in setting the conductivity values in a predefined reference temperature (10°C). Subsequently, hydraulic and thermal conductivities are re-calculated in each time step according to the current temperature (*FEFLOW 7.1 Documentation*, 2020). The predefined correlation between viscosity and temperature is a 3rd order polynomial, as presented in equations (3-36) and (3-37), which can be edited by user.

$$\frac{\mu_0^f}{\mu^f} = \frac{1 + 0.7063\zeta_0 - 0.04832\zeta_0^3}{1 + 0.7063\zeta - 0.04832\zeta^3} \tag{3-36}$$

$$\zeta = \frac{T - 150}{100} \quad , \quad \zeta_0 = \frac{T_0 - 150}{100} \tag{3-37}$$

Fluid density change with temperature, on the other hand, is considered in the simulation and cannot be turned off, unlike the option for viscosity. However, it is possible to assign a zero thermal expansion coefficient to the entire model to eliminate the temperature dependency according to equation (3-3). Dependency of the density to temperature is linear by default which reflects small temperature variations. FEFLOW allows the user to switch to a 6th order polynomial as a default nonlinear relationship which is also editable by user. By default, the Boussinesq approximation is considered which neglects all density differences except where they are multiplied by acceleration of gravity representing buoyancy terms. Boussinesq approximation is considered valid for small to moderate density changes whereas extended Oberbeck-Boussinesq function is incorporated when large density variations are expected (Diersch, 2009a). The extended Oberbeck-Boussinesq function that reflects temperature dependency is described by (Diersch et al., 2010):

$$Q_{EOB} = \beta\left(q.\nabla T + \varepsilon \frac{\partial T}{\partial t} \right) \tag{3-38}$$

Note that for standard Boussinesq approximation, the extended Oberbeck-Boussinesq equation $\left(Q_{EOB}\right)$ is set to zero.

3.8. Change in solubility and sorption with temperature

Aqueous solubility of hydrocarbons varies with temperature and the general trend for benzene and toluene is decreasing solubility with increased temperatures. This in turn leads to desorption of these species from solid phase (Finizio & Guardo, 2001).

As described in section 2.6, There are some empirical correlations between solubility $\left(S_w\right)$ and organic carbon partition coefficient $\left(k_{oc}\right)$ like equation (3-39) proposed by Kenaga, 1980 (Fetter,

2008) for aromatic hydrocarbons like benzene and toluene, Naphthalene, Pyrene and chloroethene contaminants.

Combining equation (3-39) with equation (3-40) leads to derivation of distribution coefficient $\left(k_d\right)$ which can be converted to non-dimensional linear sorption constant $\left(k\right)$ with multiplying by solid particle density $\left(\rho_s\right)$ introduced in equation (3-11):

$$\log\left(k_{oc}\right) = 3.64 - 0.55\left[\log\left(S_w\right)\right] \quad (3\text{-}39)$$

$$k_d = k_{oc}\, f_{oc} \quad (3\text{-}40)$$

$$k = \rho_s k_d = \rho_s k_{oc}\, f_{oc} \quad (3\text{-}41)$$

where f_{oc} represents soil organic carbon content which is set to 0.001 taken from (*Determining the Fraction of Organic Carbon (Foc) for Methods Three and Four*, 2017) as a conservative value. Soil particle density is taken as 2.65 kg.L^{-1}.

The correlation between the sorbed mass $\left(C^s\right)$ and the dissolved species concentration $\left(C\right)$ is explained by sorption isotherm functions. With linear sorption as the simplest model, equation (3-42) describes adsorption-desorption relationship which is linked to temperature variations implicitly through solubility changes. Note that in equation (3-42) both sorbed mass and dissolved species concentration have the same units such as mgL^{-1}.

$$C^s = k\,C \quad (3\text{-}42)$$

Based on the solubility of benzene and toluene in different temperatures taken from the work done by Finizio and Guardo, (2001), Tables 3.12 and 3.13, present sorption constants for benzene and toluene, respectively with varying temperatures.

Table 3.12. Solubility and sorption parameters for benzene in different temperatures

Temperature, θ (°C)	Solubility, S_w (mg.L^{-1})	k_{oc} (L.kg^{-1})	f_{oc}	k_d (L.kg^{-1})	ρ_s (kg.L^{-1})	k
15	1580 *	75.99	0.001	0.076	2.65	0.201
25	1620 *	74.95	0.001	0.075	2.65	0.196
35	1710 *	72.75	0.001	0.073	2.65	0.193

*Taken from Finizio and Guardo, (2001)

Table 3.13. Solubility and sorption parameters for toluene in different temperatures

Temperature, θ (°C)	Solubility, S_w (mg.L^{-1})	k_{oc} (L.kg^{-1})	f_{oc}	k_d (L.kg^{-1})	ρ_s (kg.L^{-1})	k
15	514 *	140.92	0.001	0.141	2.65	0.373
25	526 *	139.14	0.001	0.139	2.65	0.369
35	545 *	136.45	0.001	0.137	2.65	0.362

*Taken from Finizio and Guardo, (2001)

Based on the calculated sorption coefficients, a curve fitting is done in Figures 3.22 and 3.23 to achieve the correlation between sorption coefficient and temperature.

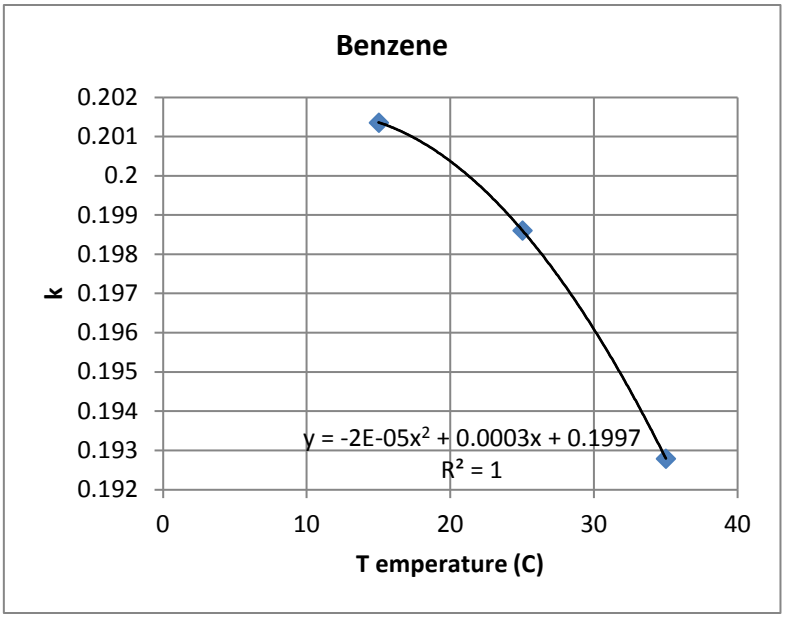

Figure 3.22. Benzene non-dimensional sorption coefficient as a function of temperature

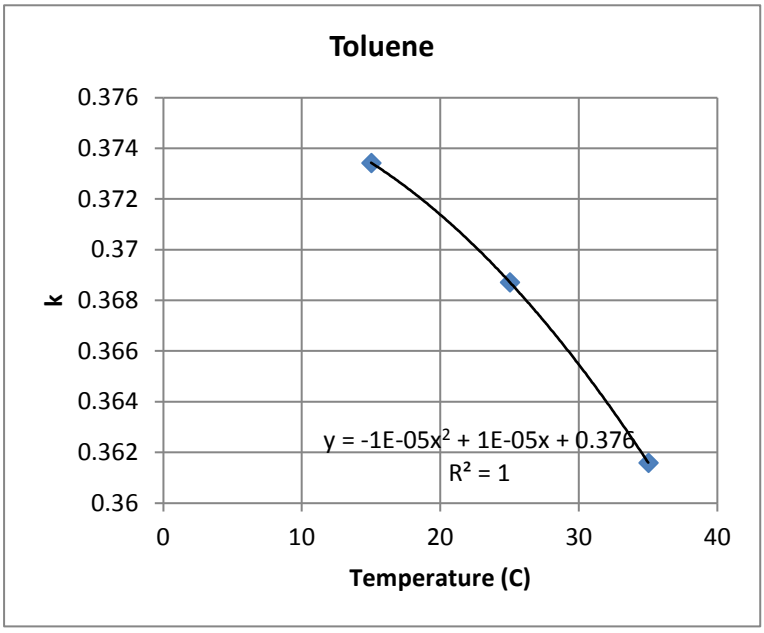

Figure 3.23. Toluene non-dimensional sorption coefficient as a function of temperature

The trend-line for benzene and toluene is presented in equation (3-43) and (3-44), respectively and is implemented in FEFLOW:

$$k = -2\times10^{-5}\theta^2 + 4.8\times10^{-4}\theta + 0.199 \quad (3\text{-}43)$$

$$k = -1\times10^{-5}\theta^2 + 1\times10^{-5}\theta + 0.376 \quad (3\text{-}44)$$

3.9. Change in biodegradation kinetics parameters with temperature

Michaelis-Menten (Monod) kinetics described in section 2.5 is selected as biodegradation mechanism in FEFLOW simulation. As stated in section 2.5, Michaelis-Menten parameters are temperature-dependent and Topiwala-Sinclair model introduced in equation (2-6) is taken for correlating with temperature. A sample of temperature-dependent kinetics parameters and Topiwala-Sinclair model fitted to experimental data for benzene and toluene is presented in Figure 3.24 and 3.25, respectively. Moreover, Table 3.14 shows temperature coefficients for Topiwala-Sinclair model fitted to these data. For future reference, this case is referred to as "original case".

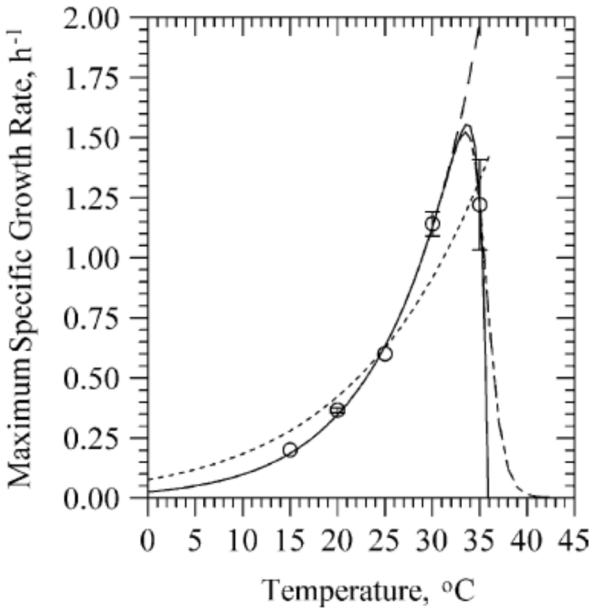

Figure 3.24. Temperature-dependent maximum specific growth rate of P. putida F1 strain grown on benzene with Topiwala-Sinclair fit (solid line) from Alagappan and Cowan, (2004)

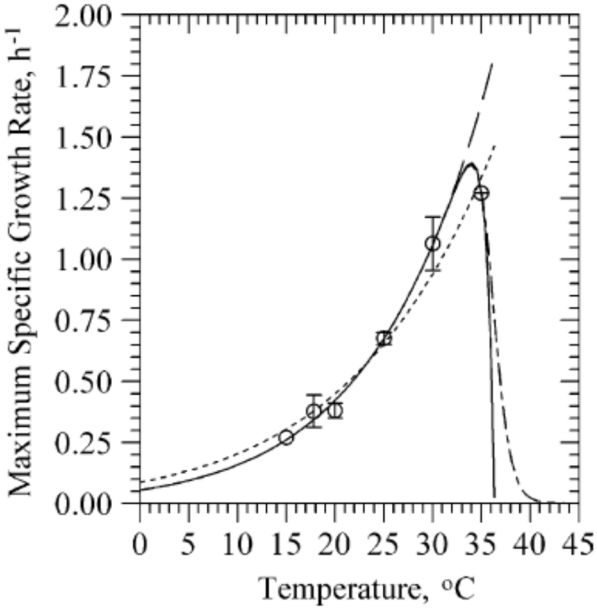

Figure 3.25. Temperature dependent maximum specific growth rate of P. putida F1 strain grown on toluene with Topiwala-Sinclair fit (solid line) from Alagappan and Cowan, (2004)

Table 3.14. Temperature coefficients for Topiwala-Sinclair fit for P. putida F1 strain from Alagappan and Cowan, (2004)

Parameter	Benzene	Toluene
A (h^{-1})	$1.2x10^{15}$	$5.1x10^{11}$
B (h^{-1})	$4.8x10^{161}$	$7.9x10^{160}$
E_a (kJ mol^{-1})	87	68
E_b(kJ mol^{-1})	954	952

With the values of Table 3.14 and universal gas constant as 8.314 $J.mol^{-1}.K^{-1}$, maximum specific growth rate in equation (2-5) is rewritten for benzene and toluene with equations (3-45) and (3-46) as follows:

$$\mu_m = A\,e^{-E_a/(R_uT)} - B\,e^{-E_b/(R_uT)} = 1.2\times10^{15}\times e^{-10464.3/T} - 4.8\times10^{161}\times e^{-114746.2/T} \quad (3\text{-}45)$$

$$\mu_m = A\,e^{-E_a/(R_uT)} - B\,e^{-E_b/(R_uT)} = 5\times10^{11}\times e^{-8179/T} - 7.9\times10^{160}\times e^{-114505.7/T} \quad (3\text{-}46)$$

Note that parameters A, B are given with the unit h^{-1} and T is the absolute temperature in K.

Biomass yield (Y), biomass concentration (B_c) and half saturation constant (k_s) are also taken from Alagappan and Cowan, (2004) and presented in Table 3.15. Although these values change with temperature, the dominant parameter is the maximum specific growth rate and hence, the other parameters were fixed for simulation. By combining equations (3-45) and (3-46) with Michaelis-Menten kinetics introduced in equation (2-3), the effect of temperature in biodegradation kinetics can be implemented in FEFLOW simulation.

Table 3.15. Michaelis-Menten kinetics parameters for benzene and toluene from Alagappan and Cowan, (2004)

Parameter	Benzene	Toluene
K_s ($mg.L^{-1}$)	2.45	0.7
Y ($mg.mg^{-1}$)	0.69	0.65
B_c ($mg.L^{-1}$)	2.7	1.61

As discussed in section 2.6, kinetics parameters are strongly site-specific reported values are not universally applicable, so each real case requires its own validated data as maximum specific growth rate or half saturation constant. On the other hand, few literature has reported the temperature coefficients as in Table 3.14 by Alagappan and Cowan, (2004). However, based on the nature of Topiwala-Sinclair model, maximum specific growth available at certain temperature and the microorganism involved, temperature dependent coefficients can be estimated. According to equation (2-5), four unknowns of A, B, E_a and E_b should be evaluated for Topiwala-Sinclair model fit which means that for four known values of maximum specific growth rate (μ_m) at different temperatures are needed. These four values can be retrieved from the following data or constraints:

1. The value of maximum specific growth rate (μ_m) at a certain temperature for some cases is reported in Table 2.3 (El-naas et al., 2014).
2. For P. putida F1 strain, the rate of microbial growth and biodegradation is reported to be around zero at 0°C (Alagappan & Cowan, 2004). Other microorganisms like P. ZD22 strain also have reported to stop growing at 0°C (H. Li et al., 2006).
3. Topiwala-Sinclair model is mathematical representation of combining two ascending $\left(A\, e^{-E_a/(R_u T)}\right)$ and descending $\left(-B\, e^{-E_b/(R_u T)}\right)$ exponential equations which have the same value at the peak of the curve in Figures 3.24 and 3.25. The maximum values reported to occurat about 34°C for P. putida F1 strain for both benzene and toluene (Alagappan & Cowan, 2004). The optimal growth temperature for another microorganism, R. rhodochrous strain, is reported as 35°C when growing on toluene as shown in Figure 3.26 (Deeb & Alvarez-cohen, 1999). In fact, most of the microorganisms involved in biodegradation of hydrocarbons are mesophiles so their optimum growth temperature is around 33°C to 39°C as shown in figure 1.14.
4. With exceeding the temperature from optimum value, enzyme thermal denaturation process is activated resulting in a dramatic decline in microbial growth and biodegradation rate. Therefore, specific growth rate in the curve plunges toward zero at temperatures above the optimum temperature.

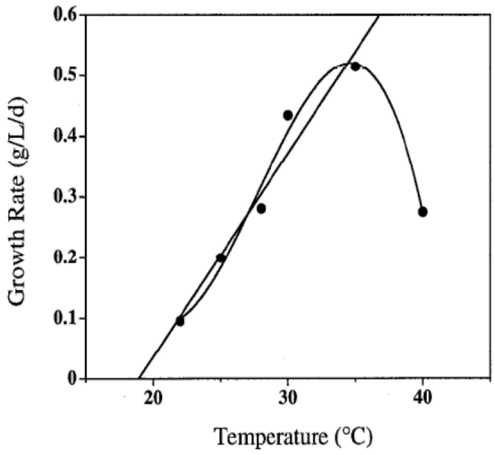

Figure 3.26. Temperature dependent growth rate of R. rhodochrousstrain grown on toluene with Topiwala-Sinclair fit from Deeb and Alvarez-cohen, (1999)

Applying these four constraints leads to achievement of four unknown temperature coefficients in Topiwala-Sinclair model. For this study, $\mu_m = 0.1631$ h^{-1} and $k_s = 71.18$ $mg.L^{-1}$ was used for benzene and $\mu_m = 0.1722$ h^{-1} and $k_s = 62.56$ $mg.L^{-1}$ for toluene from Table 2.3 for P. putida degrader. In addition, according to Figures 3.24 and 3.25, optimal temperature for microorganism growth is 34°C and maximum specific growth rate is approximately zero for 0°C and 37°C when thermal denaturation occurs. Based on these values and solving Topiwala-Sinclair equation, temperature coefficients are calculated and presented in Table 3.16, which is referred to as the "adjusted case".

Figure 3.27 plots temperature-dependent maximum specific growth rate of P. putida F1 strain grown on benzene with Topiwala-Sinclair fit for the adjusted case, which resembles Figure 3.24. Note that the values derived for the adjusted case has significantly lower degradation velocity than the case introduced by Alagappan and Cowan, (2004). To the author's knowledge, the values selected in this case are the lowest biodegradation rates reported in the literature (Table 2.3). Therefore, the adjusted case represents the worst-case scenario in terms of biodegradation, and the application of such low rates can show the impact of temperature on biodegradation process.

Table 3.16. Temperature coefficients for Topiwala-Sinclair model for P. putida F1 strain (adjusted case)

Parameter	Benzene	Toluene
A (h^{-1})	$2.8x10^{28}$	$4.85x10^{28}$
B (h^{-1})	$6.63x10^{180}$	$3.88x10^{182}$
E_a ($kJ.mol^{-1}$)	169.6	170.8
E_b ($kJ.mol^{-1}$)	1072	1082.3

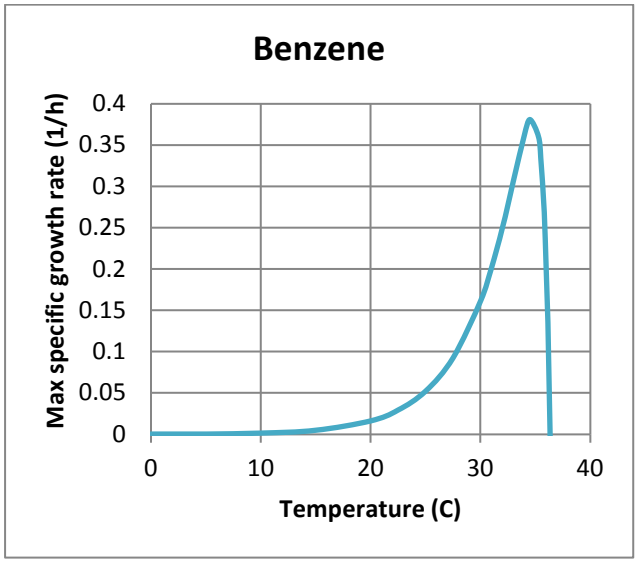

Figure 3.27. Temperature-dependent maximum specific growth rate of P. putida F1 strain grown on benzene with Topiwala-Sinclair fit (adjusted case)

By substitution of Biomass yield (Y) and biomass concentration (B_c) from Table 3.15, maximum specific growth rate in equation (2-5) is rewritten for benzene and toluene for the adjusted case with equations (3-47) and (3-48) as follows:

$$\mu_m = A\,e^{-E_a/(R_u T)} - B\,e^{-E_b/(R_u T)} = 2.8\times10^{28}\times e^{-20399.3/T} - 6.63\times10^{180}\times e^{-128939.1/T} \quad (3\text{-}47)$$

$$\mu_m = A\,e^{-E_a/(R_u T)} - B\,e^{-E_b/(R_u T)} = 4.85\times10^{28}\times e^{-20543.7/T} - 3.88\times10^{182}\times e^{-130178/T} \quad (3\text{-}48)$$

At background temperature of 10°C and Michaelis-Menten kinetics parameters from Table 3.14, linear sorption coefficient and maximum specific growth rate and maximum degradation velocity for the adjusted case for benzene are calculated from equations (3-43) and (3-47) as:

$$k = -2\times10^{-5}\theta^2 + 4.8\times10^{-4}\theta + 0.199 = 0.2018 \quad (3\text{-}49)$$

$$\mu_m = 2.8\times10^{28}\times e^{-20399.3/T} - 6.63\times10^{180}\times e^{-128939.1/T} = 1.38\times10^{-3}\ \left(h^{-1}\right) \quad (3\text{-}50)$$

$$v_{max} = \frac{\mu_m}{Y}B_c = \frac{1.38\times10^{-3}}{0.69}\times2.7 = 0.0054\ \left(mg.L^{-1}.h^{-1}\right) = 0.130\ \left(mg.L^{-1}.d^{-1}\right) \quad (3\text{-}51)$$

Moreover, linear sorption coefficient and maximum specific growth rate and maximum degradation velocity results at constant temperature of 10°C for toluene from equations (3-44) and (3-48) are as follows:

$$k = -1\times10^{-5}\theta^2 + 1\times10^{-5}\theta + 0.376 = 0.086 \quad (3\text{-}52)$$

$$\mu_m = 4.85\times10^{28}\times e^{-20543.7/T} - 3.88\times10^{182}\times e^{-130178/T} = 1.44\times10^{-3}\ \left(h^{-1}\right) \quad (3\text{-}53)$$

$$v_{max} = \frac{\mu_m}{Y}B_c = \frac{1.44\times10^{-3}}{0.65}\times1.61 = 0.0036\ \left(mg.L^{-1}.h^{-1}\right) = 0.086\ \left(mg.L^{-1}.d^{-1}\right) \quad (3\text{-}54)$$

Chapter 4 - Results and discussion

In this chapter flow and transport simulations are performed using the model that was described in the previous chapters. Various conditions are modeled to examine the effect of heat on flow and transport. As outlined in chapter 3, the model was validated for flow and transport using analytical solutions.

The second portion of this chapter deals with simulation of contaminant transport for the case of an instantaneous spill of benzene and toluene. The impact of temperature changes within the ground stemmed from geothermal heat pump utilization in first step is then incorporated into the model to capture the effect of temperature-dependent biodegradation and sorption parameters on remediation activities.

4.1. Flow and heat transport simulation results

The results of a one-year simulation using FEFLOW, with different conditions such as steady/transient flows, constant/variable viscosity and incorporation of density changes and buoyant flows are examined. Subsequently, a final simulation is done for a 10-year period for fully flow and transport transient condition, with the inclusion of variable viscosity and density effects. Note that a transient transport simulation might be applied with combination of transient flow and transient transport equation or alternatively, with steady-state flow and transient heat transport assumption. By assuming steady-state flow conditions, only one iteration is performed for flow model and the resulting flow field is applied for transient transport simulation (*FEFLOW 7.1 Documentation*, 2020). Moreover, FEFLOW allows for neglecting the temperature-dependent density changes by eliminating extended Oberbeck-Boussinesq terms $\left(Q_{EOB}\right)$ as stated in equation (3-38). This is done by placing a value of zero for thermal expansion coefficient $\left(\beta\right)$ thus neutralizing any changes in density with temperature. To incorporate the changes with temperature, a value of 1×10^{-4} K^{-1} is applied as water thermal expansion coefficient for an average temperature of 10°C (*The Engineering ToolBox - Volumetric or Cubic Thermal Expansion*,

2020). Furthermore, a temperature-dependent viscosity can be chosen in the FEFLOW transport setting box, which directly changes the hydraulic conductivity, while variable density also impacts the Darcy flux vector (q) as described in equations (3-1) to (3-4). Consequently, both viscosity and density changes with temperature impact the Darcy equation and flow field.

For flow and heat transport simulations, 5 scenarios are taken into account as presented in Table 4.1. Note that unlike viscosity, density could not turn to constant in FEFLOW setting so an expansion coefficient of zero is applied to the whole model whenever changes in density are neglected. On the other hand, expansion coefficient is set to 1×10^{-4} K^{-1} for variable density situation.

Table 4.1. Different scenarios for flow and heat transport simulation

Case	Flow condition	Transport condition	Viscosity condition	Density condition
FH-1	Transient	Transient	Variable	Variable
FH-2	Transient	Transient	Variable	Constant
FH-3	Transient	Transient	Constant	Variable
FH-4	Transient	Transient	Constant	Constant
FH-5	Steady	Transient	Variable	Variable

4.1.1. Simulation results for case FH-1 - transient flow, variable viscosity and variable density

According to the ground load calculated in Table 3.4, thermal load applied to the BHEs accounts for 5 months of heating from January to May, followed by 3 months of cooling from June to August and then again, 4 months of heating from September to December.

First, a steady flow simulation is performed to achieve steady state head distribution in the domain as depicted in Figure 4.1. This head distribution is then considered as initial head condition for transient simulations.

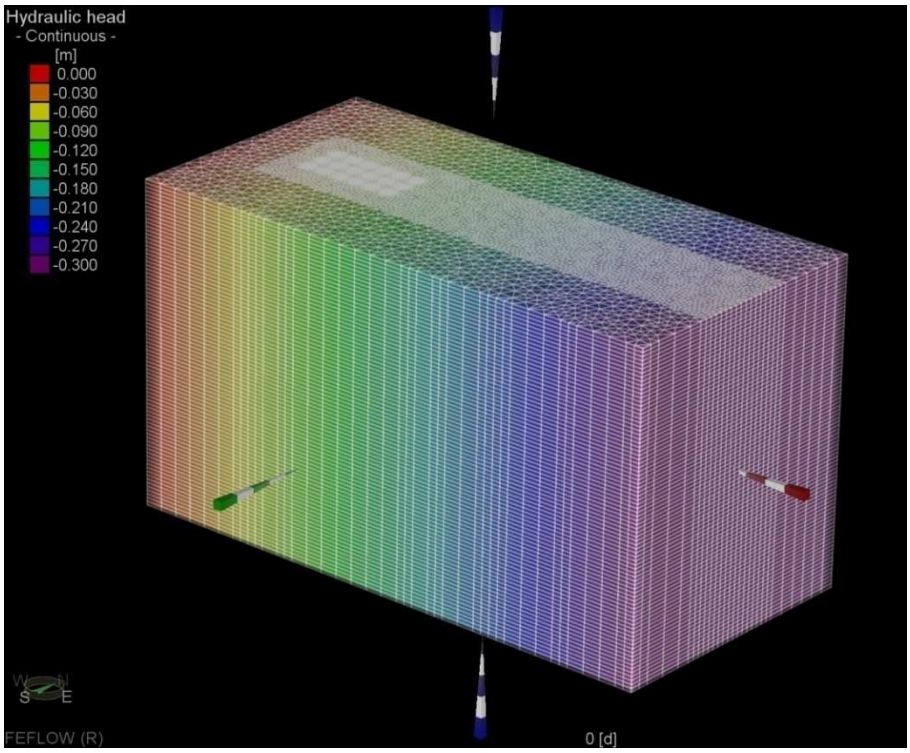

Figure 4.1. Steady state head distribution results

For the 5 cases introduced in Table 4.1, a simulation is performed for one year and the results are derived in the form of Darcy flux and temperature distribution. Figure 4.2 shows the temperature distribution results after one year (December) of operation for case FH1, as the base model, with variable viscosity and density. The results are shown from a side-view in the mid-plane of the model which corresponds to the central row of BHEs. In Figure 4.2, temperature ranges from -2.2°C at the top layer due to the surrounding air temperature, to 12.8°C at the front of the BHEs, indicating formation of a thermal plume. For better illustration, a top view at a slice located at 30 mbgs is plotted in Figure 4.3 which shows formation of heat plumes downgradient of flow.

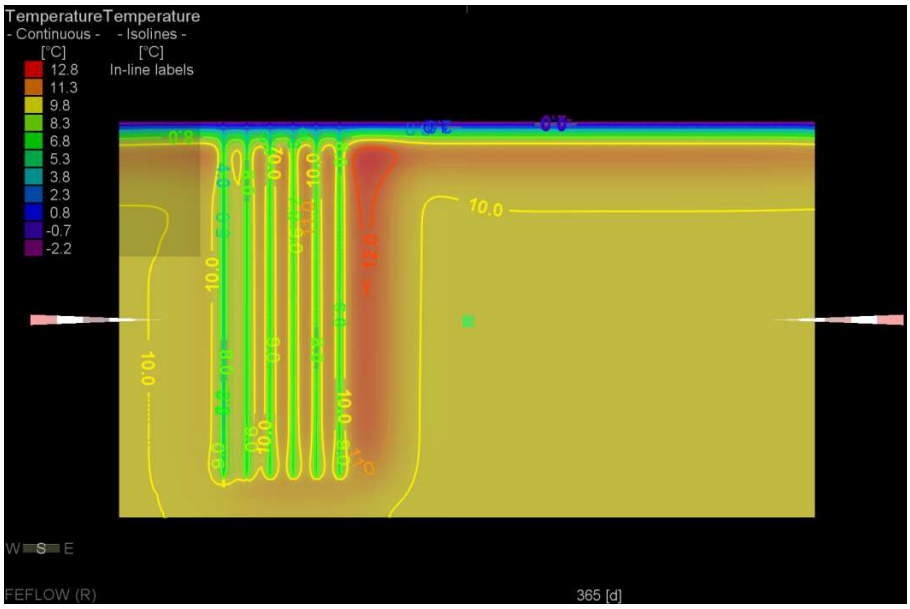

Figure 4.2. Temperature distribution from the side-view in the mid-plane, for case FH-1 after one year

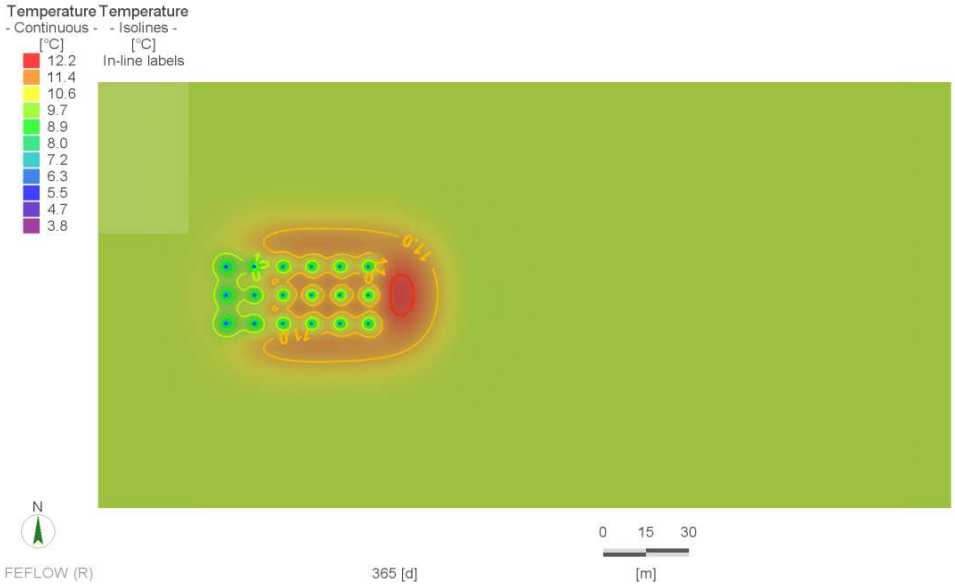

Figure 4.3. Top view of the thermal plume for case FH-1 at 30 mbgs after one year

Figure 4.4 illustrates Darcy flux from a cross sectional view in the mid-plane of the model (from BHE 7 to 12 in Figure 3.6) at the end of December of first year. The bullets representing Darcy flux are inclined towards the bottom of the domain which shows formation of downward buoyant flows owing to the heating mode operation and decrease in subsurface temperature around the

boreholes. The only exception is associated with about 20 m in bottom area which is free of BHEs and about 6 m near surface which is subject to air temperature.

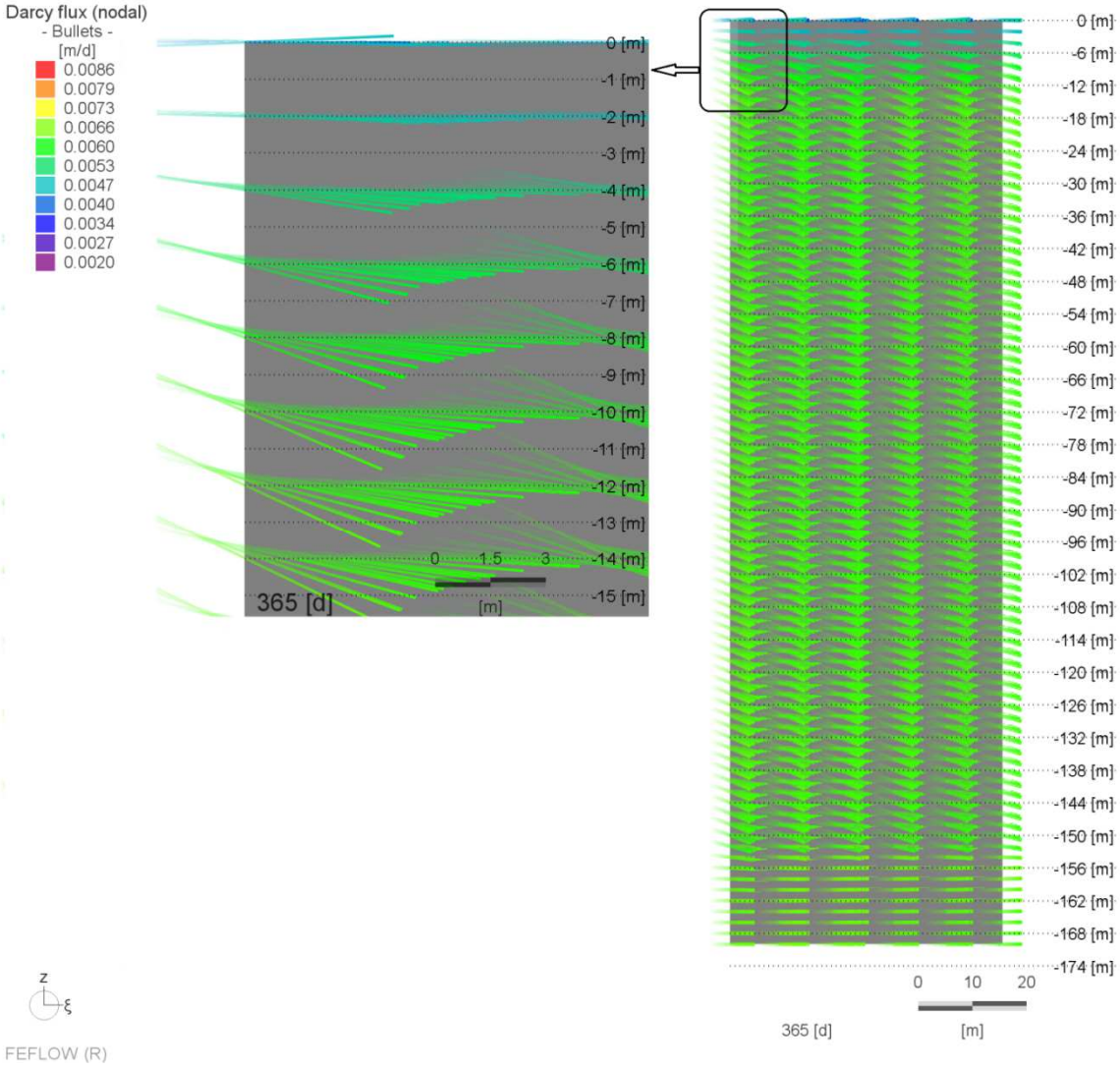

Figure 4.4. Darcy flux cross sectional view in the mid-plane of case FH-1 after one year

Figure 4.5 shows a cross sectional view of Darcy flux after 8 months at the end of August which is also end of cooling season. The upward Darcy flux bullets indicate formation of buoyant flow around the boreholes due to cooling season operation and the resulting temperature increase within the ground.

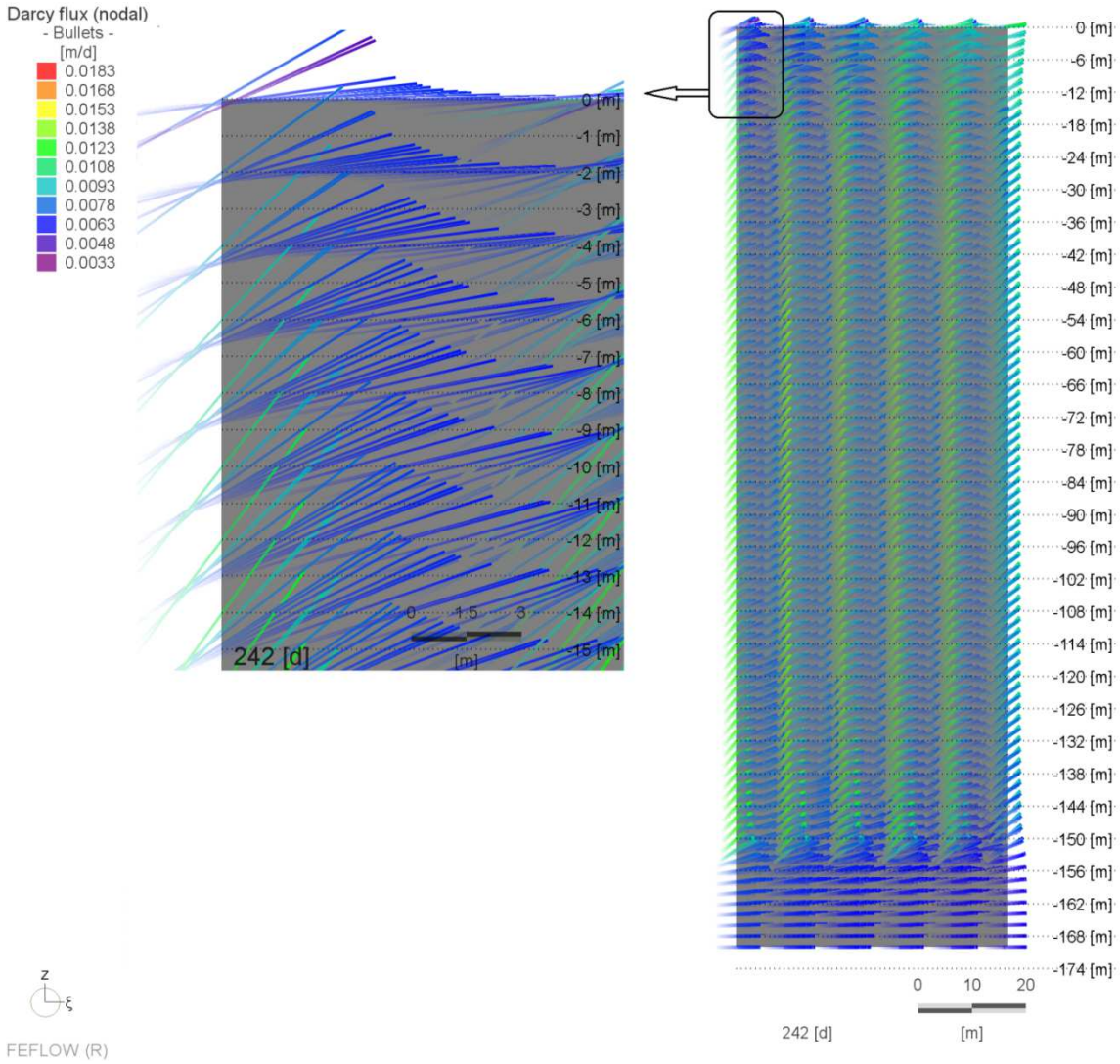

Figure 4.5. Darcy flux cross sectional view in the mid-plane of case FH-1 after 8 months

4.1.2. Simulation results for case FH-2 - transient flow, variable viscosity and constant density

Figure 4.6 depicts temperature distribution results (side view) after one year for case FH-2 with variable viscosity and constant density in the mid-plane of the domain. The temperature range is from -2.2°C to 12.8°C and the distribution of temperature is identical to case FH-1. On the other hand, illustration of thermal plumes at depth of 30 mbgs in Figure 4.7 shows slight differences in temperature distribution compared to Figure 4.3 for case FH1.

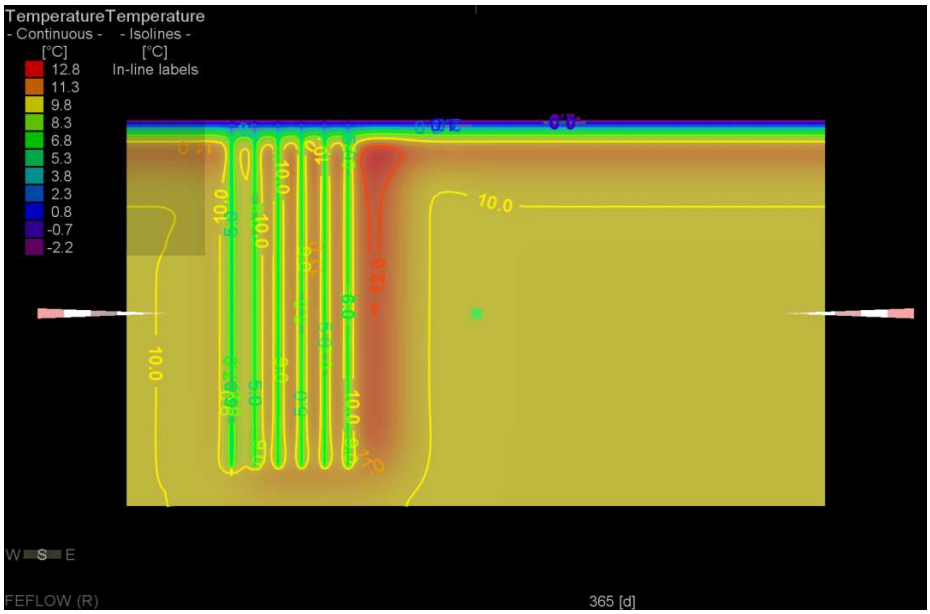

Figure 4.6. Temperature distribution from the side-view in the mid-plane, for case FH-2 after one year

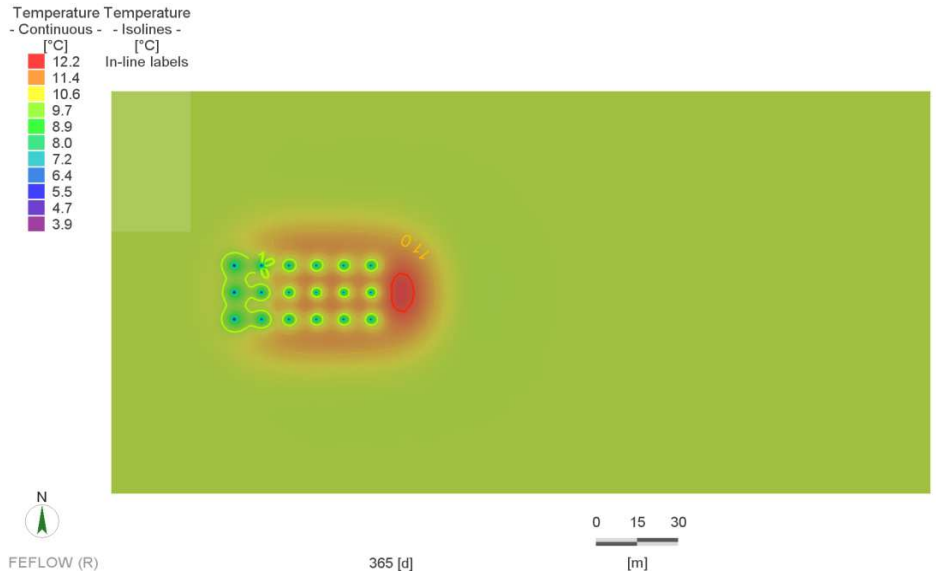

Figure 4.7. Top view of the thermal plume for case FH-2 at 30 mbgs after one year

In Figure 4.8, cross sectional view of Darcy flux in case FH-2 after one year is plotted. Not surprisingly, Darcy flux vectors remains horizontal showing absence of temperature-driven buoyant flows when no density variation is taken into account. Darcy velocity varies from 0.0045 to 0.0067 $m.d^{-1}$ throughout the entire domain for this case while it was from 0.0020 to 0.0086 $m.d^{-1}$ for case FH-1 plotted in Figure 4.4.

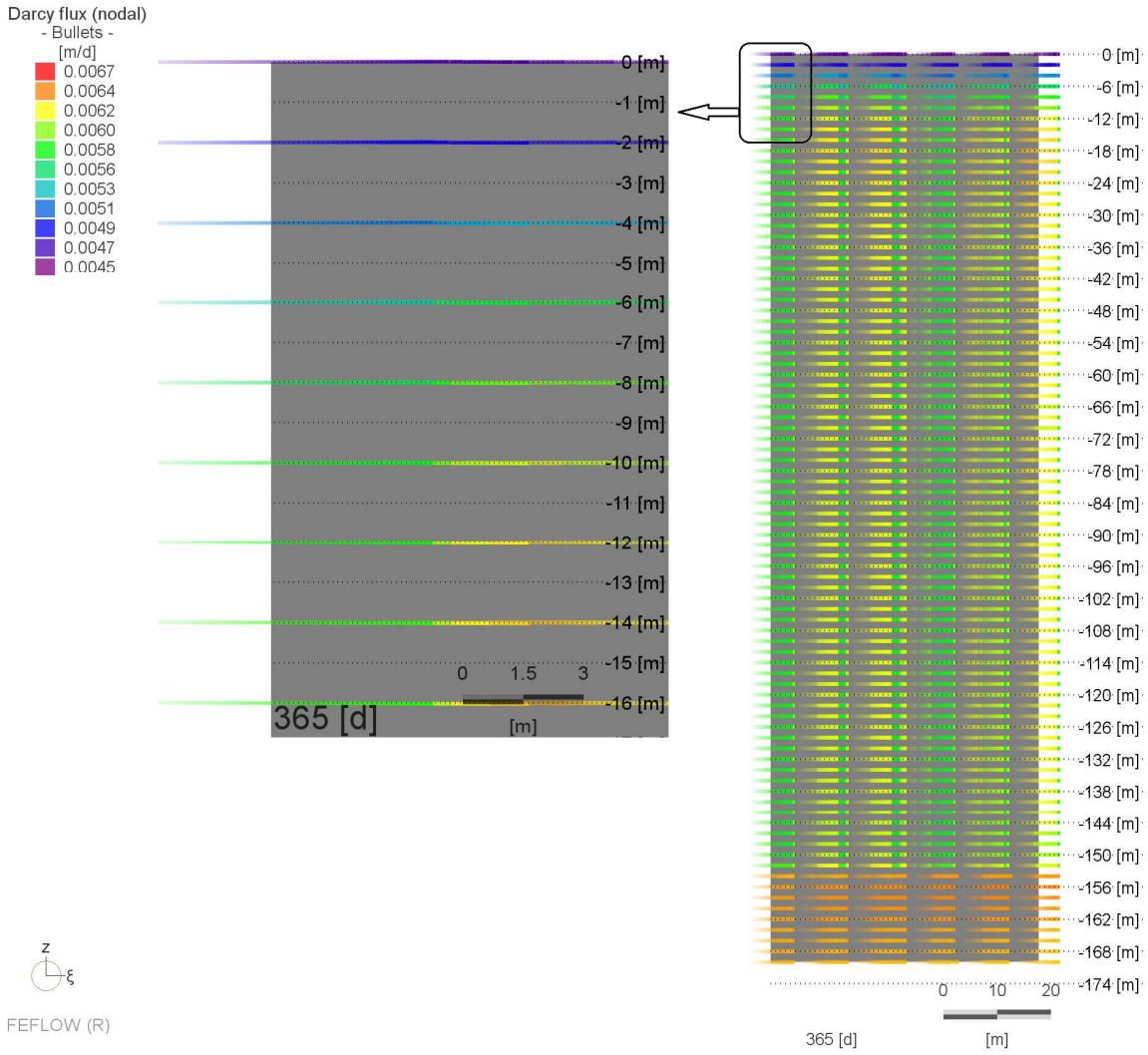

Figure 4.8. Darcy flux cross sectional view in the mid-plane of case FH-2 after one year

4.1.3. Simulation results for case FH-3 - transient flow, constant viscosity and variable density

Figure 4.9 depicts side-view temperature distribution results after one year of operation for case FH-3 with constant viscosity and variable density in the mid-plane of the model, showing general temperature range of -2.2°C to 12.7°C. Although maximum temperature is slightly lower than the FH-1 and FH-2 cases, the arrangement of isothermal lines shows great similarity with the previous cases. Moreover, thermal plumes at the depth of 30 mbgs are presented in Figure 4.10 which resemble the results for base case FH-1 presented in Figure 4.3.

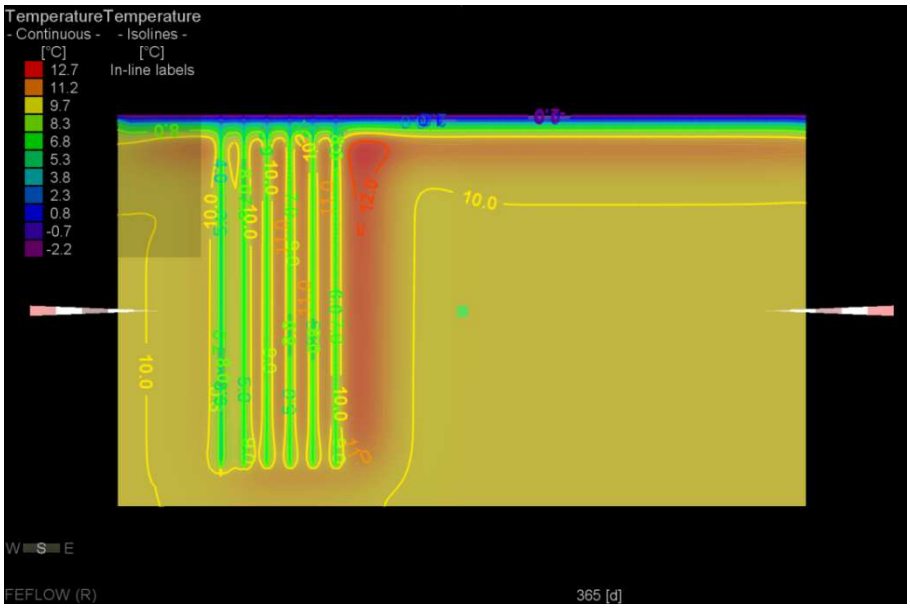

Figure 4.9. Temperature distribution from the side-view in the mid-plane, for case FH-3 after one year

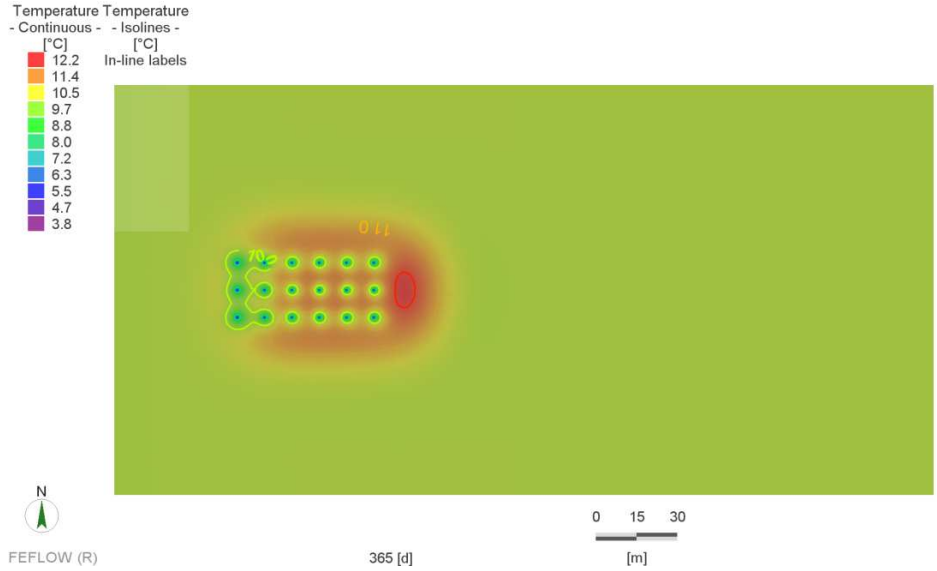

Figure 4.10. Top view of the thermal plume for case FH3 at 30 mbgs after one year

In Figure 4.11, cross sectional view of Darcy flux in case FH-3 after one year is plotted indicating development of temperature-driven buoyant flows with inclusion of density variation with temperature. The range of Darcy velocity is from 0.0028 to 0.0115 $m.d^{-1}$ which is a broader range compared to range of 0.0045 to 0.0067 $m.d^{-1}$ for case FH-2 in Figure 4.8 and 0.0020 to 0.0086 $m.d^{-1}$ for case FH-1 plotted in Figure 4.4.

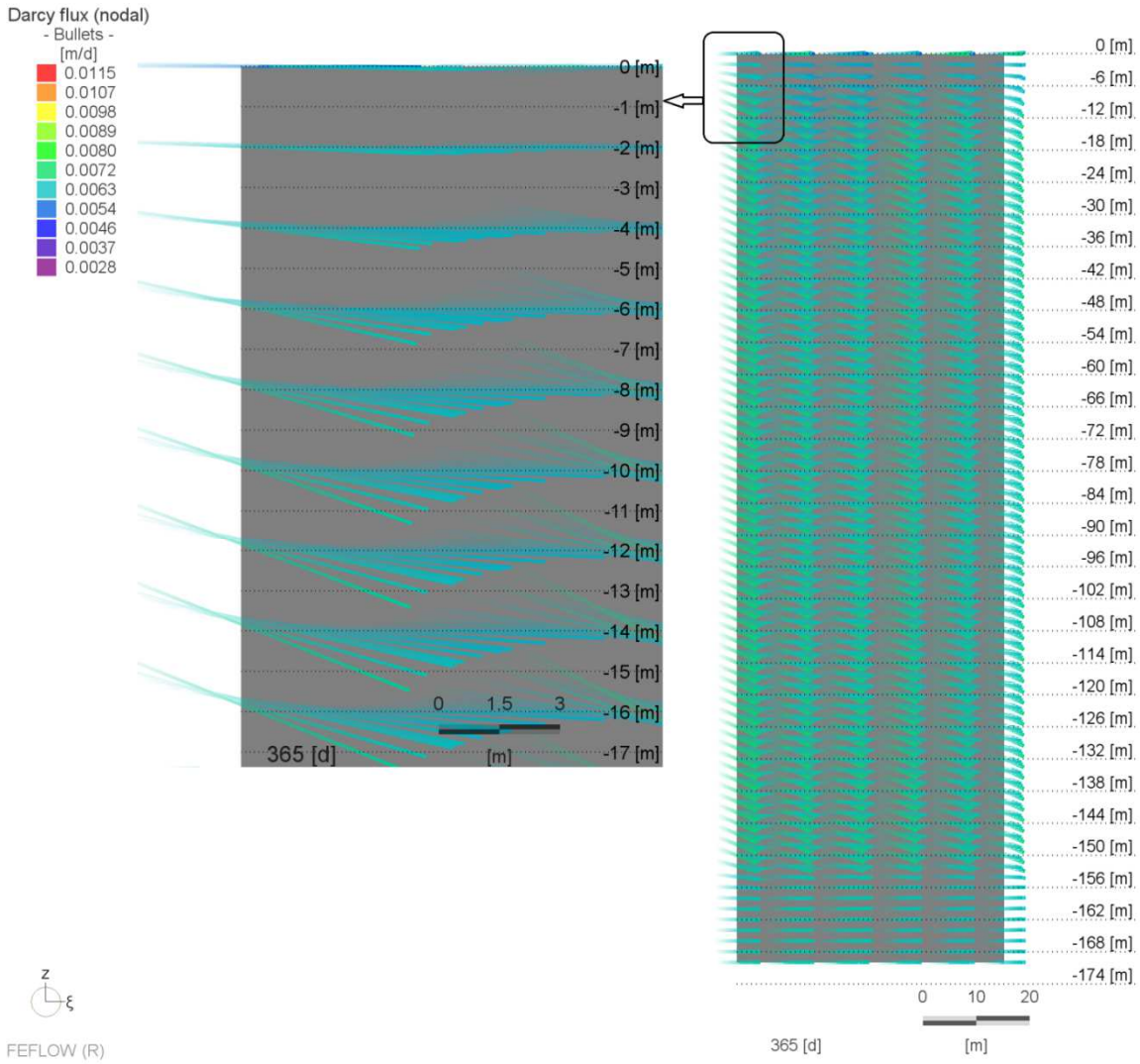

Figure 4.11. Darcy flux cross sectional view in the mid-plane of case FH-3 after one year

4.1.4. Simulation results for case FH-4 - transient flow, constant viscosity and constant density

Figure 4.12 shows side-view temperature distribution results after one year for case FH-4 with constant viscosity and constant density in the mid-plane of the model. Unlike other cases, temperature ranges from -2.2°C to 10.8°C in the vertical cross section and temperature isolines presented in Figure 4.13 at the depth of 30 mbgs, show significant differences to the previous cases. In this case, temperature varies from 1.4°C to 10.0°C and no evidence of thermal plume development is obvious in the plot. Therefore, neglecting temperature-driven changes in density

and viscosity due to heat pump operation could lead to significant deviation from realistic flow and temperature distribution within the ground and fails in capturing accurate thermal plumes.

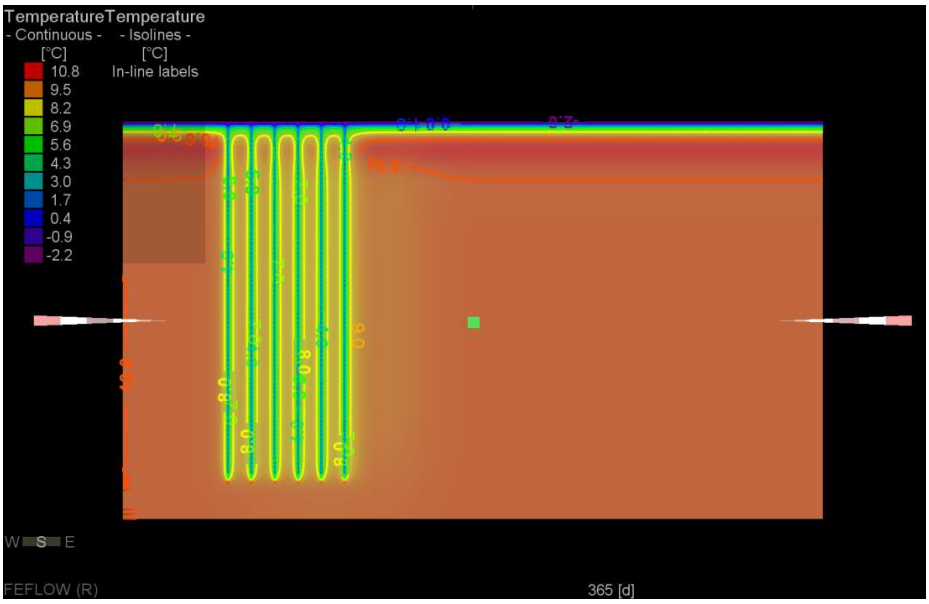

Figure 4.12. Temperature distribution from the side-view in the mid-plane, for case FH-4 after one year

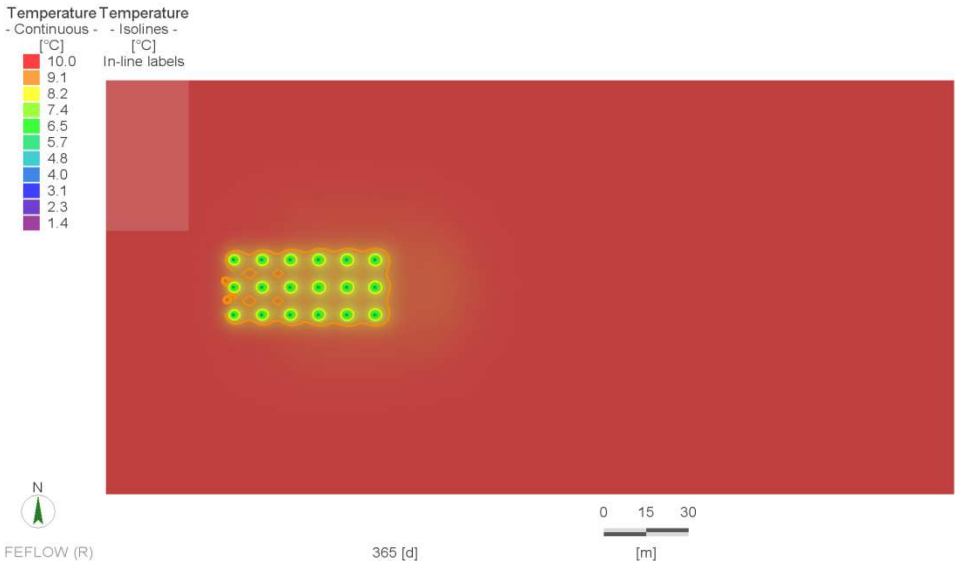

Figure 4.13. Top view of the thermal plume for case FH-4 at 30 mbgs after one year

Figure 4.14 depicts Darcy flux results at the end of one year operation for case FH-4. As expected from the assumption of constant viscosity and density, the Darcy flux remains constant at the entire model, regardless of the temperature changes around the BHEs.

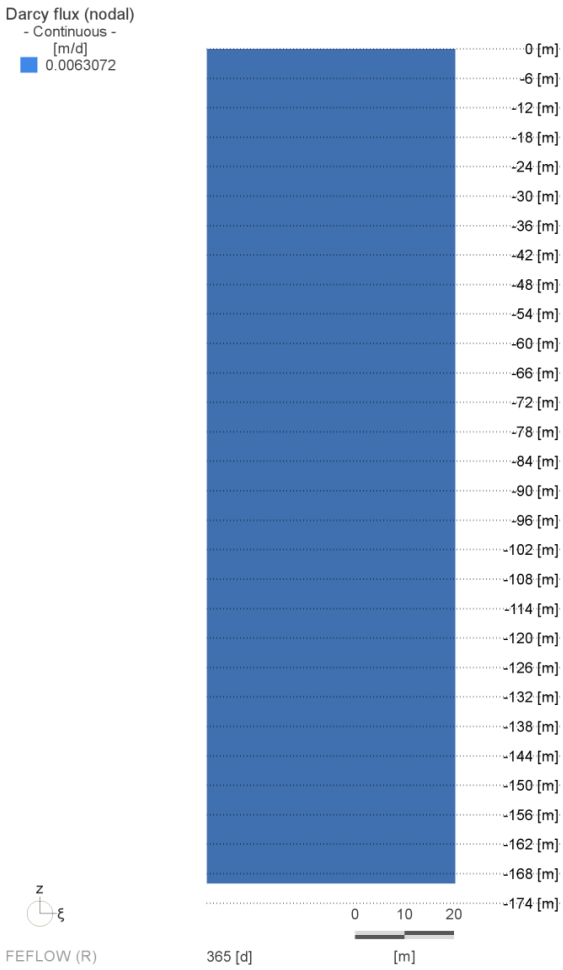

Figure 4.14. Darcy flux from cross sectional view in the mid-plane of case FH-4 after one year

4.1.5. Simulation results for case FH-5 - steady flow, variable viscosity and variable density

Figures 4.15, 4.16 and 4.17 show side-view temperature distribution, thermal plumes at 30 mbgs and cross-sectional Darcy flux after one year, respectively, for case FH-5 which is similar to case FH-1 except that the flow is considered steady. Comparison of Figure 4.15 to 4.2 for temperature profiles in vertical cross section and Figure 4.16 to 4.3 for thermal plumes at 30 mbgs show significant differences. Moreover, the range of Darcy flux variation in Figure 4.17 is from 0.0026

to 0.0075 $m.d^{-1}$ which reveals a notable contrast to Darcy flux in Figure 4.4 for case FH-1 (from 0.0020 to 0.0086 $m.d^{-1}$). Therefore, assumption of steady flows instead of transient condition can cause considerable error in both flow and temperature distributions. Comparison of results after one year for all 5 cases is summarized in Table 4.2.

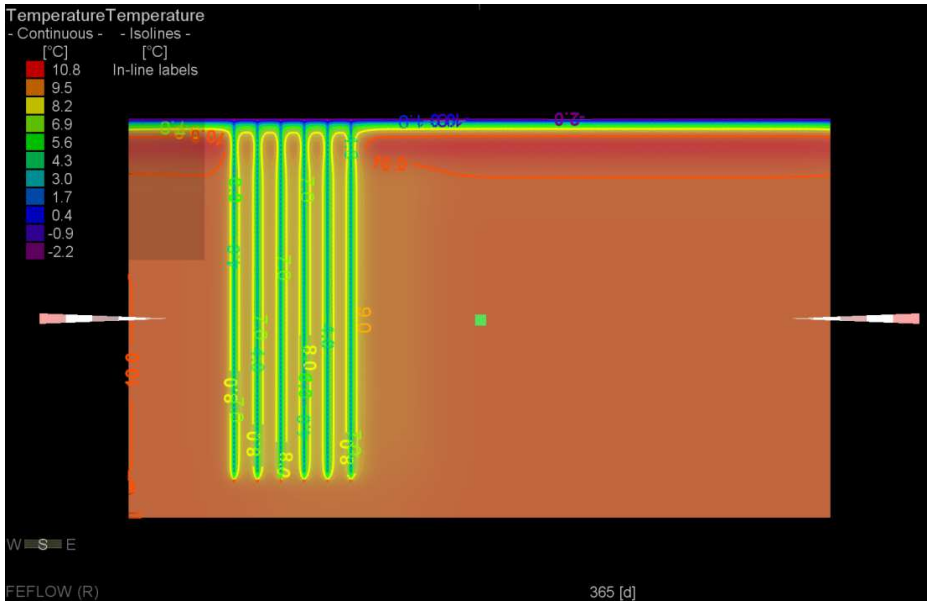

Figure 4.15. Temperature distribution from the side-view in the mid-plane, for case FH-5 after one year

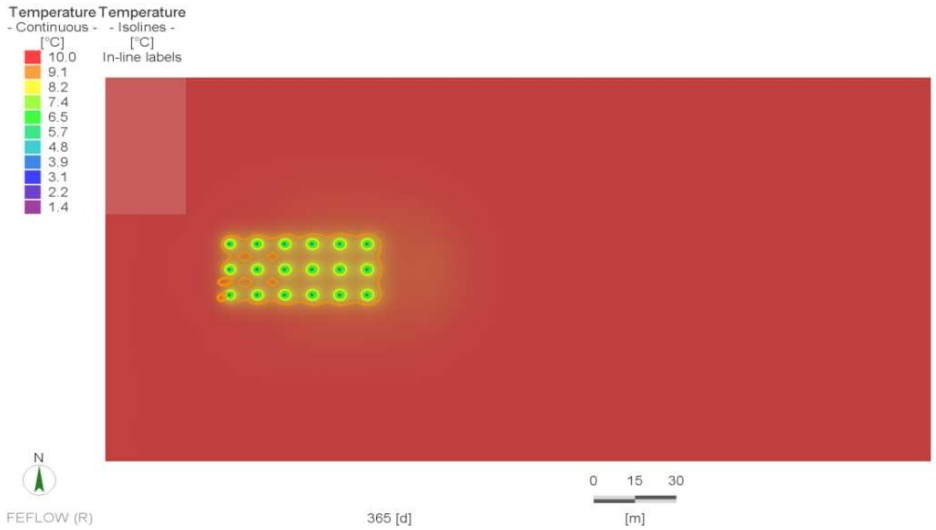

Figure 4.16. Top view of the thermal plume for case FH-5 at 30 mbgs after one year

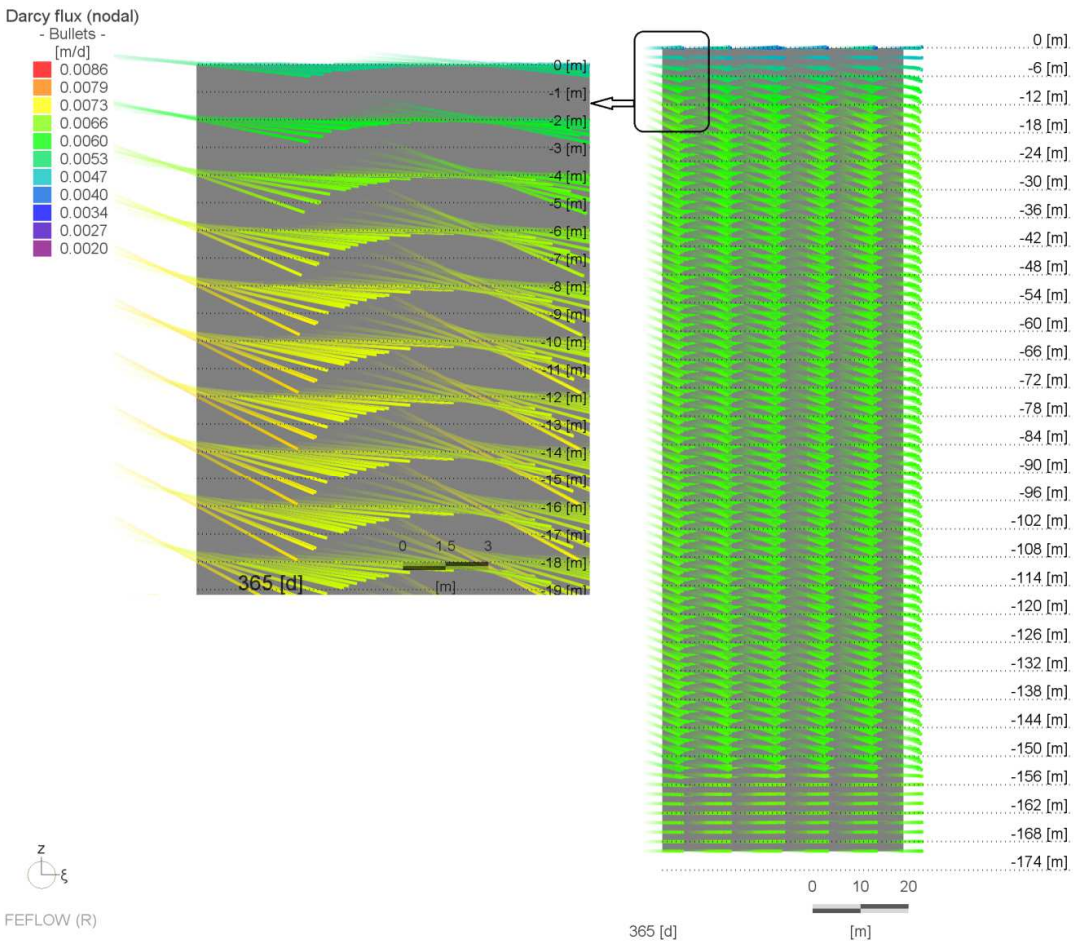

Figure 4.17. Darcy flux from cross sectional view in the mid-plane of case FH-5after one year

Table 4.2. Summary of results for different scenarios of flow and heat transport simulations after one year

Case	Description	Temperature range at mid-plane cross section (°C)	Temperature range at 30 mbgs slice (°C)	Darcy velocity range ($m.d^{-1}$)	Thermal plume
FH-1	Transient heat and flow, variable density and viscosity	-2.2 to 12.8	3.8 to 12.2	0.0020 to 0.0086	Yes
FH-2	Transient heat and flow, variable viscosity, constant density	-2.2 to 12.8	3.9 to 12.2	0.0045 to 0.0067	Yes
FH-3	Transient heat and flow, variable density, constant viscosity	-2.2 to 12.7	3.8 to 12.2	0.0028 to 0.0115	Yes
FH-4	Transient heat and flow, constant viscosity and density	-2.2 to 10.8	1.4 to 10	0.0063	No
FH-5	Transient heat, steady flow, variable density and viscosity	-2.2 to 10.8	1.4 to 10	0.0026 to 0.0075	No

4.1.6. Simulation results after 10 years

In this section, the results for a 10-year simulation for case FH-1 is presented. Figure 4.18 depicts the side-view temperature distribution results for case FH-1 at the end of December of the 10th year. Comparing the maximum temperature with the corresponding results of first year in Figure 4.2 shows a rise from 12.8°C to 13.4°C. More importantly, isothermal line of 11°C has reached the eastern boundary of the system which is about 200 m far from the last boreholes. Note that subsurface background temperature at the beginning of BHE operation was 10°C.

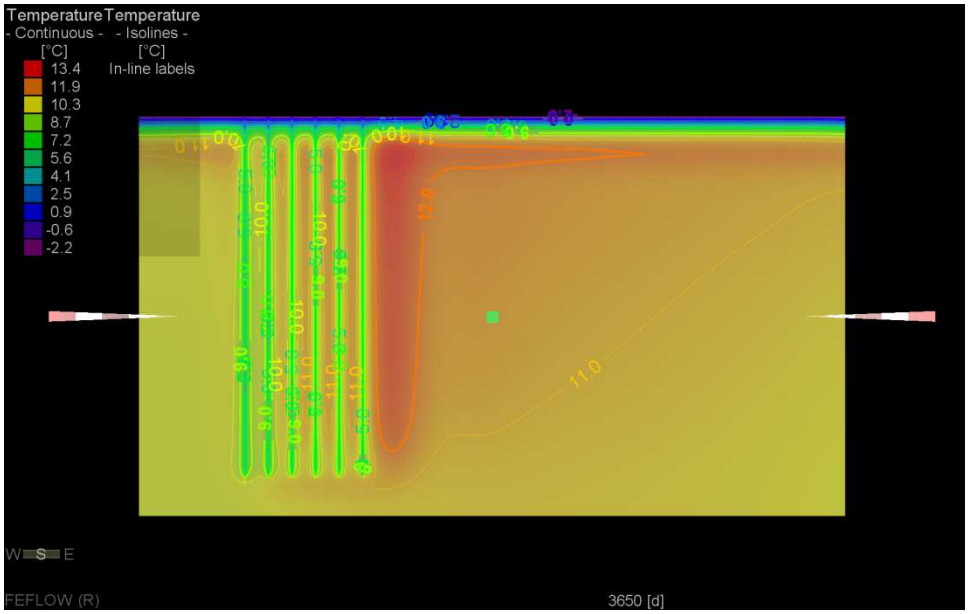

Figure 4.18. Temperature distribution from the side-view in the mid-plane, for case FH-1 at the end of December of the 10th year

Subsurface temperature distributions at 30 mbgs at the end of May for 1st and 10th years of operation is plotted in Figure 4.19 which clearly show formation and development of thermal plumes in heat affected zone with long-term operation of geothermal BHE system. Compared to background temperature of 10°C before BHE operation, temperature rise in the flow direction indicates the excessive heat injected into the subsurface from the building due to the cooling dominated load case. Due to lack of cooling period from January to May, the end of May results at the end of the first year does not reveal any change in background temperature. Nevertheless,

after 10 years of operation with sequential heating and cooling, the thermal plumes do develop showing a change in temperature distribution within the ground.

Moreover, the 11°C temperature isoline has reached the northern, southern and eastern boundaries as shown in Figure 4.19, which indicates a vast area is affected by the rise in temperature even though a moderate Darcy flux of around 0.006 $m.d^{-1}$ (7×10^{-8} $m.s^{-1}$) is assumed in this simulation. It should be noted that higher values of groundwater flux can lead to heat affected zone expansion, though it can also alleviate the extent to which temperature rises. On the other hand, low values of groundwater flux help contain the heat affected zone, tough at the cost of lower heat transfer rates and higher temperature raise in the immediate vicinity of the boreholes.

In Figure 4.20, temperature distributions at the end of August after one and ten years of simulation at 30 mbgs are depicted. Despite the apparent similarity of two profiles, 10-year operation of BHEs has resulted in lasting changes in subsurface temperature from 10°C to 11°C in an extensive area in the model. Moreover, the maximum temperature at 10 years is higher than the first year of BHE operation.

Finally, Figure 4.21 compares thermal plumes at the same depth at the end of December of the 1st and 10th years which clearly shows development of thermal plumes with time. As can be seen, the unbalanced heating and cooling loads led to lasting changes in background temperature within the subsurface, even at the end of 1st year of BHE operation and a rise up to 12.2°C is observed. The excess heat injected into the ground is accumulated with time and the maximum temperature is elevated to 13.1°C at the end of 10th year.

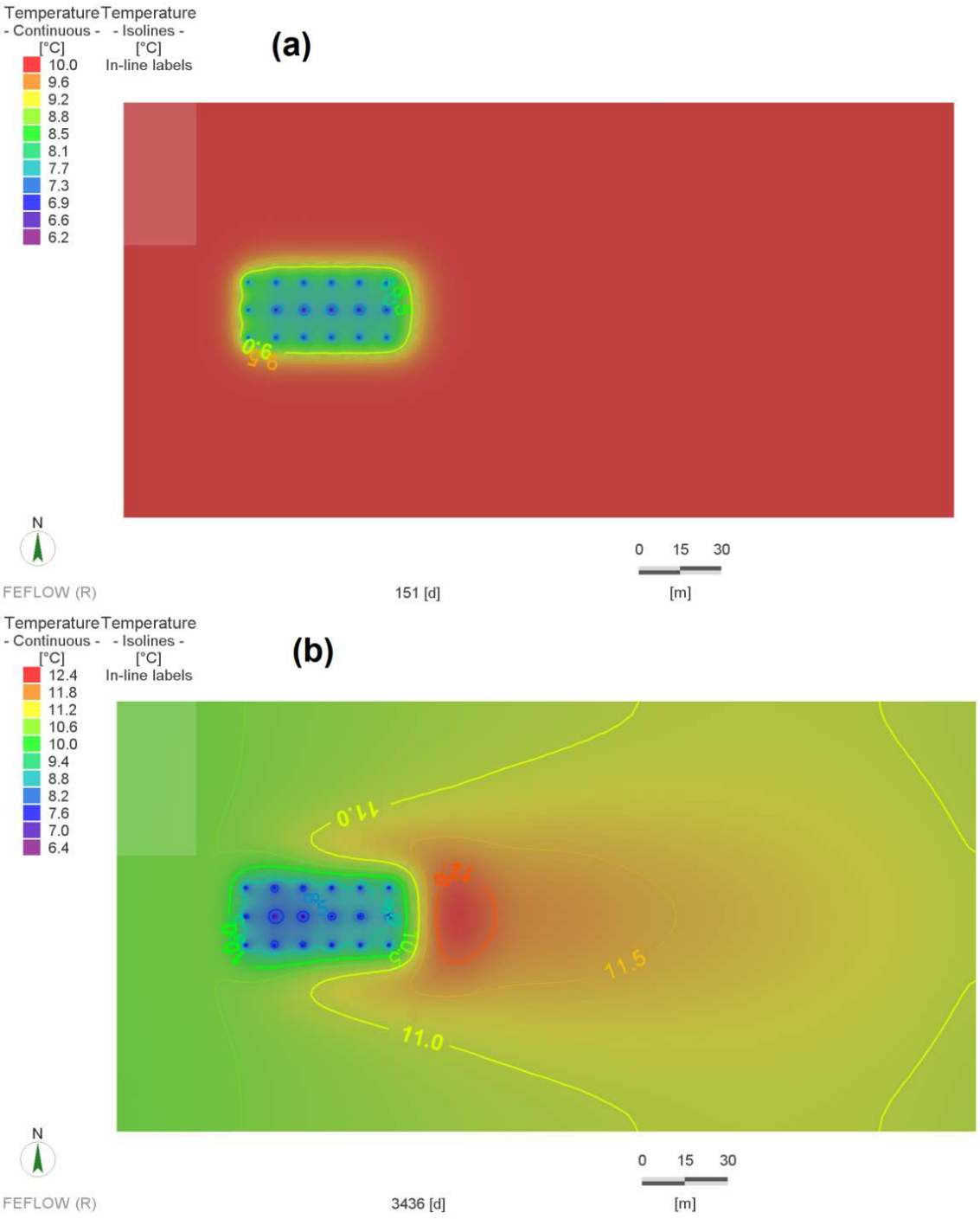

Figure 4.19. Comparison of thermal plume development at 30 mbgs at the end of May of the 1st year (a) and 10th year (b)

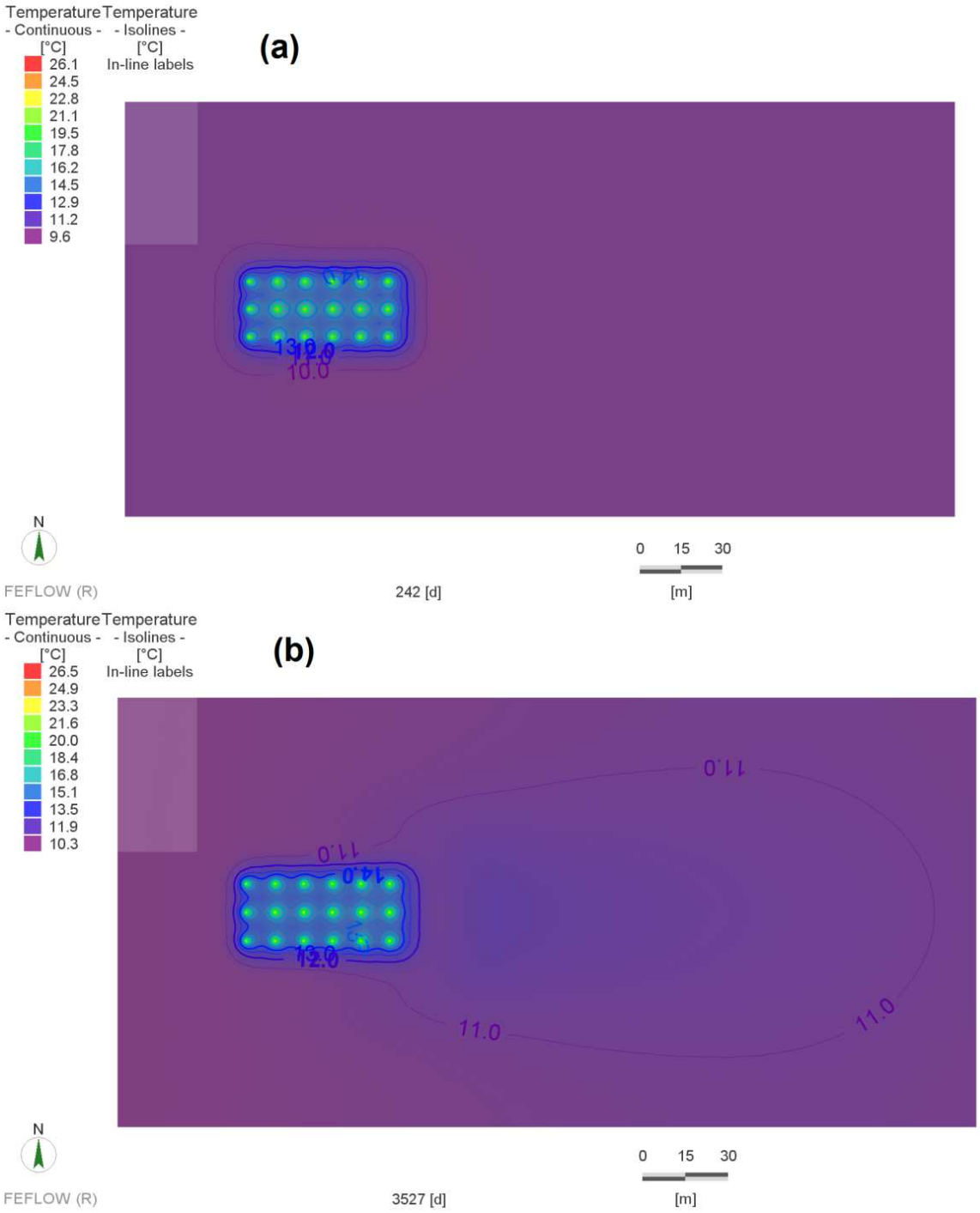

Figure 4.20. Comparison of thermal plume development at 30 mbgs at the end of August of the 1st year (a) and 10th year (b)

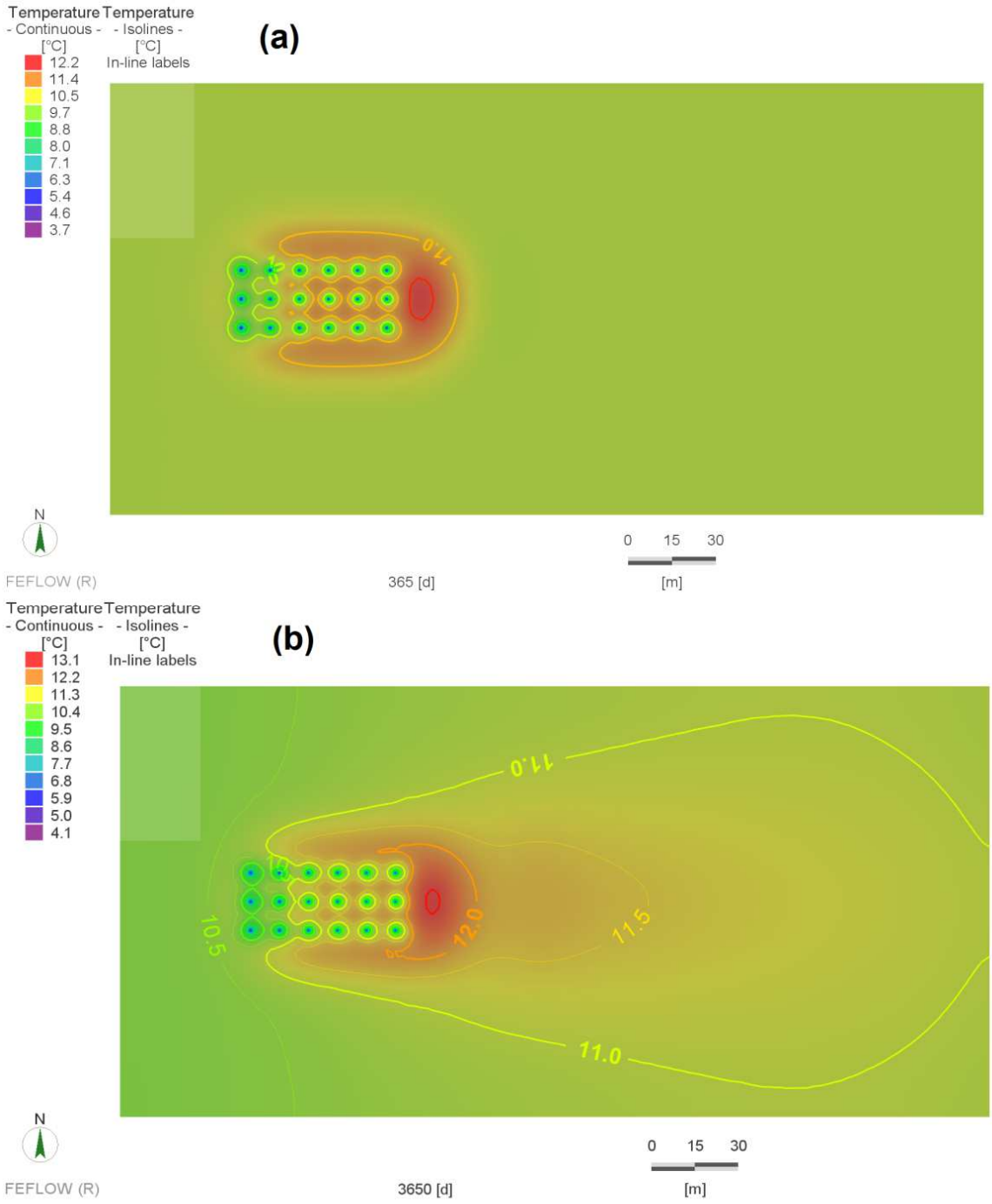

Figure 4.21. Comparison of thermal plume development at 30 mbgs at the end of December of the 1st year (a) and 10th year (b)

4.1.7. Effect of surface temperature fluctuations

To capture the penetration depth of outdoor air temperature, Darcy flux and ground temperatures at the end of 10 years simulations at the end of May, August and December are plotted in Figure 4.22 and 4.23, respectively. Considering the difference between the top zone (which is affected by air temperature) and the rest of the model, it can be inferred that zone of seasonal fluctuation is limited to about top 12 m near the surface. Moreover, the bottom zone of the domain which is free of boreholes, remained unaffected from temperature and Darcy flux variations which indicates that bottom boundary does not have any impact on the model.

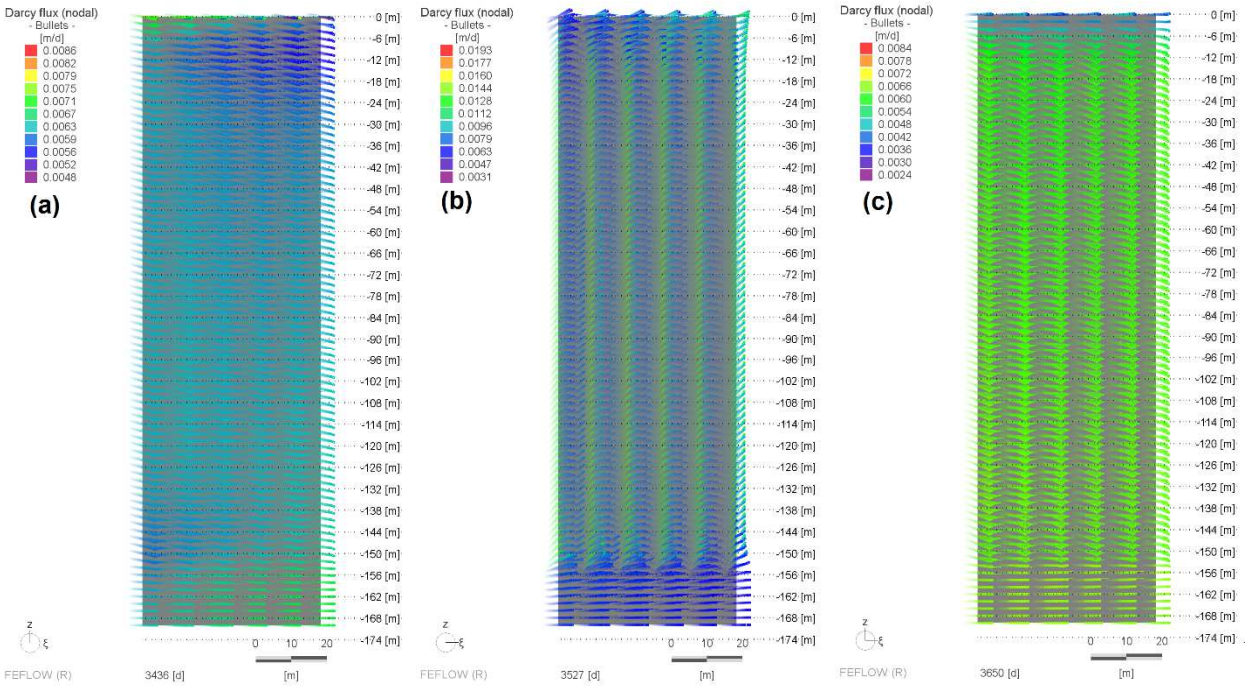

Figure 4.22. Comparison of Darcy flux from cross sectional view in the mid-plane of the model at 10th year at the end of May (a), August (b) and December (c)

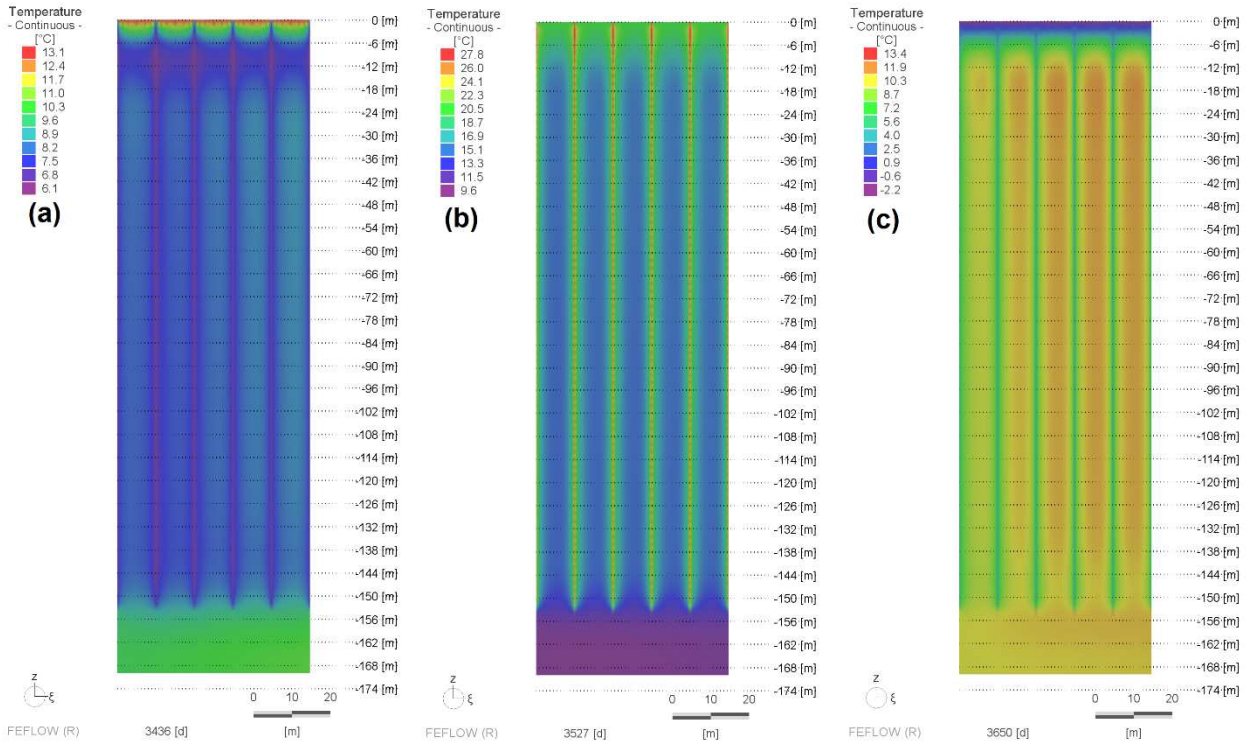

Figure 4.23. Comparison of temperature from cross sectional view in the mid-plane of the model at 10th year at the end of May (a), August (b) and December (c)

4.2. Contaminant transport simulation results

In this section, the results for contaminant transport simulations for benzene and toluene are presented. Since the final objective of this thesis is to study the impact of temperature changes resulting from geothermal heating on contaminants transport and fate, corresponding transport parameters varying with temperature were implemented in the simulation. As discussed in chapter 3.8 and 3.9, linear sorption model is adopted and Michaelis-Menten (Monod) kinetics is selected as the degradation model.

For temperature-dependent sorption coefficient, equations (3-43) and (3-44) were introduced in chapter 3.8 and equations (3-45), (3-46), (3-47) and (3-48) represent the Monod parameters as a function of temperature. Nevertheless, explicit correlation of variable sorption and Monod parameters are not applicable in FEFLOW. FEFLOW allows for definition of these parameters as a function of temperature via "Expression editor" varying with location for every node at initial

condition but they remain constant for the rest of simulation. Another approach is to use an implicit association of sorption coefficient and Monod parameters with temperature through the "time series" option. Defining through time series, however, allows for setting sorption and Monod parameters variable with time but not with location. In this regard, the average temperature history is derived from the flow and heat transport simulations (section 4.1) for case FH-1 as shown in Figure 4.24. Subsequently, the temperature is interpolated at every month and then the aforementioned parameters are calculated using equations (3-43) to (3-48) at the correlated temperature. Therefore, a time series was defined for each of the sorption coefficient and Monod parameter in FEFLOW which projects these parameters at any simulation time. Admittedly, the plot shows average temperature in the vicinity of the boreholes and the temperature at far distance is ignored in this approach. Therefore, it is only applicable to a contaminant source located in the vicinity of the boreholes. Nonetheless, this approximation paves the way to include variable temperature-dependent sorption and biodegradation kinetics in a contaminant transport simulation.

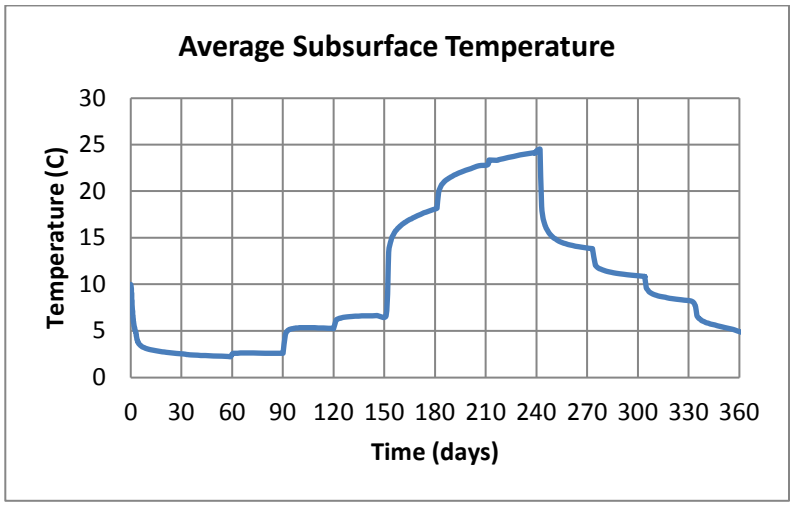

Figure 4.24. Average temperature from case FH-1 for the first year of BHE operation

Based on the values from Figure 4.24, time-varying sorption coefficient and Monod velocity for benzene and toluene are evaluated from equations (3-43) to (3-48) and are shown in Tables 4.3

and 4.4, respectively. Note that the values in Tables 4.3 and 4.4 are reported at the end of the month and a linear interpolation is employed for the other days in each month.

Table 4.3. Variable sorption coefficient and Monod velocity parameter for benzene

Month	Temperature (°C)	Sorption coefficient (-)	Monod velocity ($mg.L^{-1}.d^{-1}$)
Jan	2.5	0.2001	0.0185
Feb	2.3	0.2000	0.0171
Mar	2.6	0.2001	0.0188
Apr	5.3	0.2010	0.0383
May	6.7	0.2013	0.0551
Jun	18.2	0.2011	0.9919
Jul	23.4	0.1993	3.3664
Aug	24.5	0.1987	4.3925
Sep	13.8	0.2018	0.3411
Oct	10.9	0.2019	0.1621
Nov	7.6	0.2015	0.0711
Dec	4.7	0.2008	0.0327

Table 4.4. Variable sorption coefficient and Monod velocity parameter for toluene

Month	Temperature (°C)	Sorption coefficient (-)	Monod velocity ($mg.L^{-1}.d^{-1}$)
Jan	2.5	0.3760	0.0120
Feb	2.3	0.3760	0.0111
Mar	2.6	0.3760	0.0122
Apr	5.3	0.3758	0.0250
May	6.7	0.3756	0.0360
Jun	18.2	0.3729	0.6623
Jul	23.4	0.3708	2.2675
Aug	24.5	0.3702	2.9642
Sep	13.8	0.3742	0.2261
Oct	10.9	0.3749	0.1069
Nov	7.6	0.3755	0.0466
Dec	4.7	0.3758	0.0213

For benzene, 6 different scenarios in Table 4.5 are considered to examine the effect of temperature dependent sorption and degradation parameters on subsurface contaminant fate and transport. Moreover, another 2 cases are assumed for toluene transport which contrast the effect of temperature on sorption and biodegradation (Table 4.6).

Table 4.5. Different scenarios for benzene contaminant transport simulations

Case	Sorption	Biodegradation	Flow and heat transport description
C-1	Constant sorption at 10°C (equation 3.49)	No biodegradation	Transient flow Transient heat transport
C-2	Variable sorption with temperature (Table 4.3)	No biodegradation	Transient flow Transient heat transport
C-3	Constant sorption at 10°C (equation 3.49)	Constant biodegradation at 10°C (equation 3.51)	Transient flow Transient heat transport
C-4	Constant sorption at 10°C (equation 3.49)	Variable biodegradation with temperature (Table 4.3)	Transient flow Transient heat transport
C-5	Constant sorption at 10°C (equation 3.49)	Constant biodegradation at 10°C (equation 3.51)	Transient flow No heat transport
C-6	Variable sorption with temperature (Table 4.3)	Variable biodegradation with temperature (Table 4.3)	Transient flow Transient heat transport

Table 4.6. Different scenarios for toluene contaminant transport simulations

Case	Sorption	Biodegradation	Flow and heat transport description
C-7	Constant sorption at 10°C (equation 3.52)	Constant biodegradation at 10°C (equation 3.54)	Transient flow No heat transport
C-8	Variable sorption with temperature (Table 4.4)	Variable biodegradation with temperature (Table 4.4)	Transient flow Transient heat transport

In chapter 3.9, two cases were introduced with temperature-dependent biodegradation coefficients and equations. The first one, namely original case, described by equations (3-45) and (3-46) was directly taken from the work done by Alagappan and Cowan, (2004) and the second

one, was developed from various reported values and described by equations (3-47) and (3-48). The purpose of introducing two cases was to compare two scenarios of temperature-dependent biodegradation, namely one with a high biodegradation rate (original case) and another at a low rate (adjusted case). The rate of biodegradation for the original case, however, was so high that the concentration reached almost zero in less than one month. Therefore, capturing the impact of temperature on biodegradation was not possible since Monod degradation velocity varies on a monthly basis in the simulation. In addition, the nature of subsequent heating and cooling modes of the heat pump calls for the impact of temperature on biodegradation to be investigated for at least one year where complete heating and cooling cycles can be included. Otherwise, the results will appear to be heavily dependent on the start time and season of the geothermal heat pump system operation. As such, only the results for adjusted case, with lower biodegradation rates, are presented in the following sections. This represents the worst-case scenario where biodegradation rates are low.

4.2.1. Summary of assumptions in biodegradation modeling

Despite the capabilities of FEFLOW software and the novel approach applied in this study to include variable-rate Monod kinetics in biodegradation modeling, some assumptions needed to be considered:

1. This study assumes only aerobic metabolism -as the prevailing method for BTEX biodegradation- and neglects anaerobic pathways.
2. Interaction of different hydrocarbon contaminants in a mixture might lead to co-metabolism or competition for biodegradation which adds to the complexity; Monod equation does not account for such interactions and therefore they were not included in this study (Bekins et al., 1998).
3. Monod equation is empirical and biodegradation parameters are strongly site-specific. Therefore, biodegradation rates for a certain microorganism and contaminants, is not universally applicable and may vary from site to site.

4. Elevated temperatures could result in change in volatilization, which is not included in this study.
5. Biodegradation is a complex process with many contributing factors besides temperature. Interaction of such parameters could lead to different biochemical pathways and formation of byproducts which in turn might impact biodegradation. The effect of temperature on biodegradation is the only factor considered in this study.
6. Monod equation is sensitive to the initial substrate concentration, i.e., the lower the half saturation constant, the greater the capacity to grow rapidly in an environment with low concentration (Diersch, 2009b). Therefore, extrapolation of the biodegradation results to other concentration levels is not recommended.
7. The approach in this study uses the average ground temperature in the vicinity of the boreholes to model biodegradation parameters variable with time and temperature. However, the changes associated with location are neglected due to the limitations in FEFLOW software. Therefore, it is only applicable to the contaminant source located in the vicinity of the boreholes.

4.2.2. Impact of variable sorption coefficient on benzene transport

For all the simulations, case FH-1 (introduced in section 4.1.1) was used and transient mass transport was included to simulate the instantaneous spill of benzene. Cases C-5 and C-7 were simulated without heat transport to represent no geothermal heating. The spill is modeled with an initial 100 $mg.L^{-1}$ concentration at a depth of 28 to 32 mbgs, as shown in Figure 4.25, in top view. The initial concentration of 100 $mg.L^{-1}$ was chosen based on the literature presented in section 2.8 showing that typical toluene and benzene concentrations are in this range. In addition, high contaminant concentration can result in inhibiting microbial growth (Logeshwaran et al., 2018).

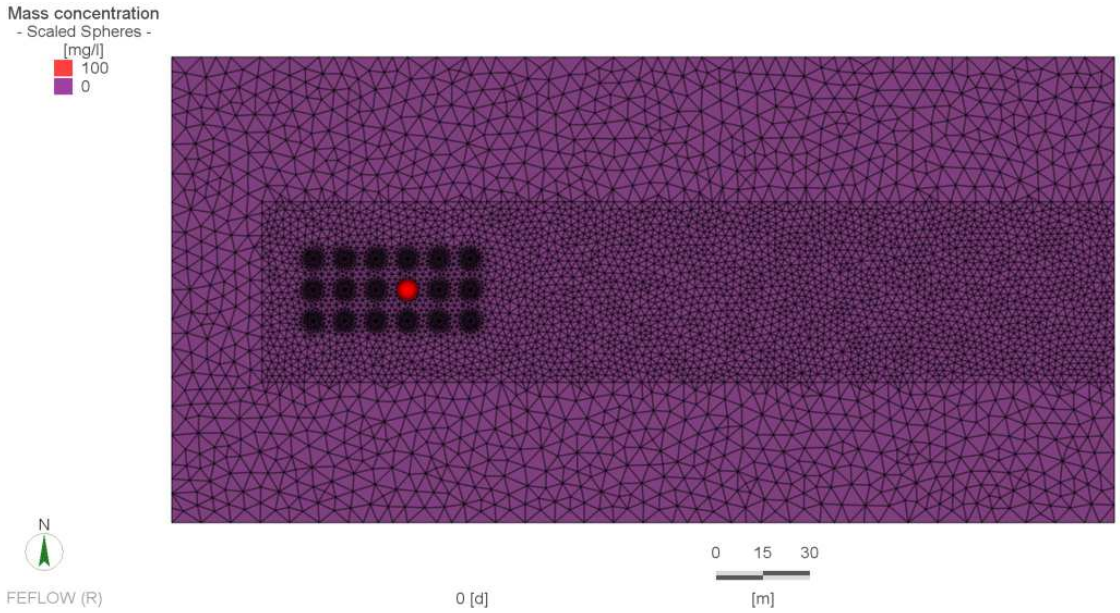

Figure 4.25. Initial concentration of contaminant spill located at the depth of 28 to 32 mbgs

To study the effect of variable sorption coefficient on benzene transport within the subsurface, a one-year simulation is performed for two cases of C-1 and C-2 and the mass concentration results are plotted in Figure 4.26. Both cases neglect biodegradation in the model but C-1 incorporates constant sorption at 10°C as the background temperature, whereas C-2 assumes variable sorption parameter.

Comparison of the results show that initial concentration of 100 $mg.L^{-1}$ is reduced to maximum 0.554 and 0.472 $mg.L^{-1}$ for constant and variable sorption coefficients, respectively. The 15% difference between the results indicates slight impact of temperature-dependent assumption for sorption with a change in sorption from 0.1987 to 0.2019 due to temperature dependency.

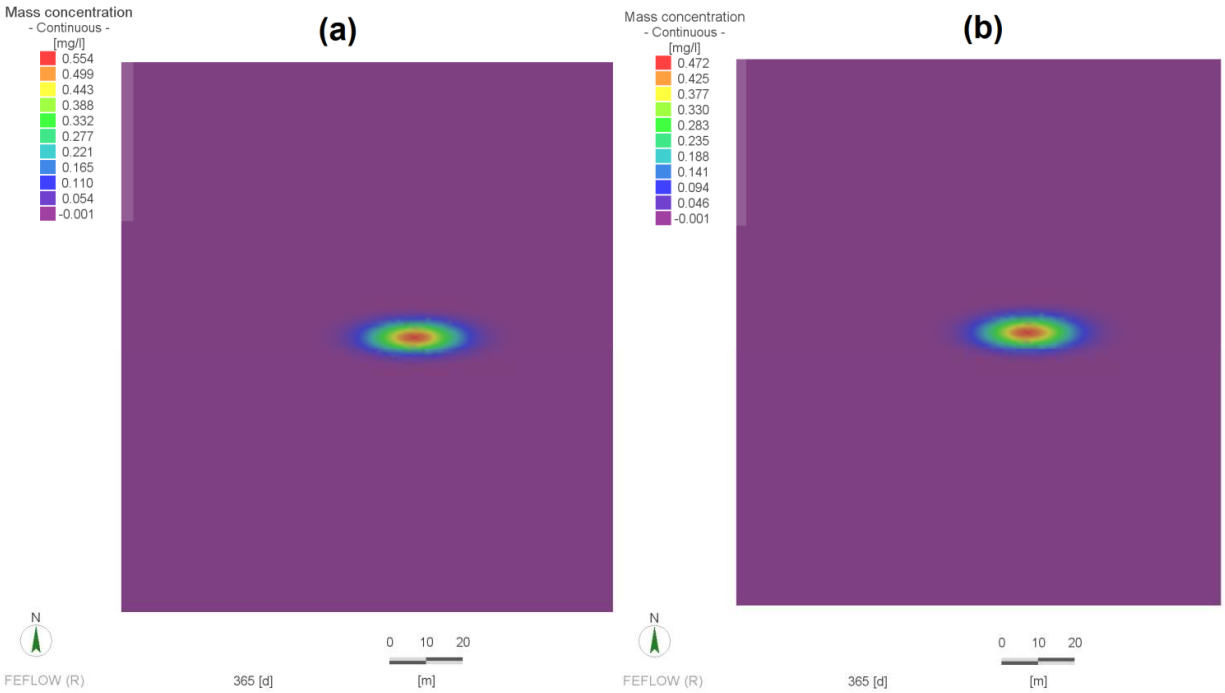

Figure 4.26. Effect of sorption on benzene mass concentration at 30 mbgs (top view) after one year for (a) constant sorption (case C-1) and (b) variable sorption (case C-2); no biodegradation

4.2.3. Impact of variable Monod velocity on benzene transport

Figure 4.27 illustrates the impact of biodegradation for benzene after one year at 30 mbgs in top view, by simulating case C-3 with constant sorption and biodegradation parameters and case C-4 which assumes constant sorption but variable biodegradation with temperature.

Comparison of the results in Figures of 4.26 and 4.27 illustrates the impact of variable biodegradation on contaminant transport. As depicted in Figure 4.26 (a) for case C-1, the maximum concentration of benzene after one year is 0.554 $mg.L^{-1}$ when no biodegradation is employed in the model. The results for case C-3 in Figure 4.27 (a) with assumption of constant biodegradation at background temperature of 10°C show maximum concentration of 0.247 $mg.L^{-1}$. However, the results for variable biodegradation parameter for case C-4 in Figure 4.27 (b), showing a drastic decline in maximum concentration to 0.011 $mg.L^{-1}$ at the end of the first year, demonstrate the significant impact of heat injected into the subsurface in biodegradation of

benzene. The temperature change for this time period is from 2.5 to 24.5 °C as plotted in Figure 4.24.

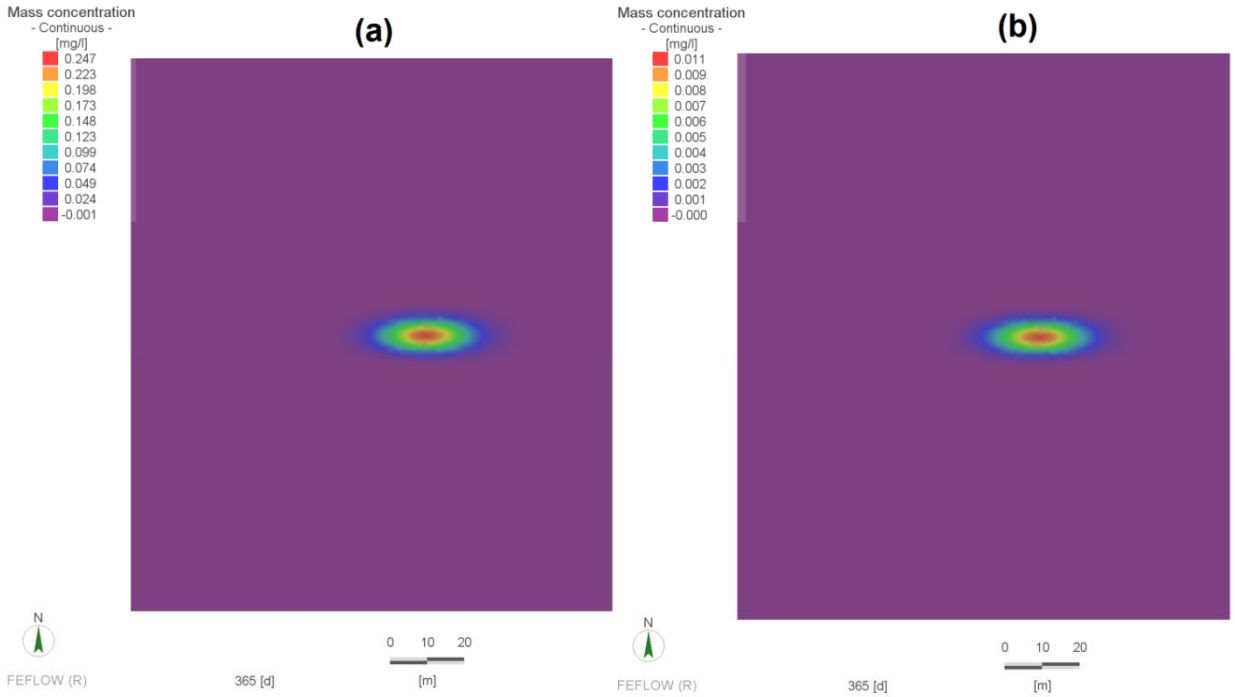

Figure 4.27. Effect of biodegradation on benzene mass concentration at 30 mbgs (top view) after one year for (a) constant biodegradation (case C-3) and (b) variable biodegradation (case C-4); constant sorption is assumed for both cases

4.2.4. Impact of geothermal heating on benzene transport and fate with temperature-dependent sorption and biodegradation

Since one of the main goals of this research was to capture the impact of temperature changes resulting from geothermal heating on contaminants' fate and transport, it is essential to compare the results of contaminants transport with and without heat transport within the subsurface. For this reason, Figure 4.28 depicts the results for case C-5 where the temperature is assumed to be constant at 10°C and case C-6 with variable sorption and biodegradation resulted from BHE operation. Comparison of the simulation results for these two cases reveals a remarkable mass concentration decline from 0.306 to 0.011 mg.L^{-1}, when heat transfer with subsurface occurs and

temperature-dependent biodegradation and sorption are assumed in the simulation. Moreover, case C-4 presented in Figure 4.27 (b) and case C-6 in Figure 4.28 (b) show almost identical results which emphasize that the assumption of variable sorption coefficient does not play a significant role, compared to variable biodegradation. Table 4.7 summarizes the maximum concentration results for all 6 cases of benzene transport.

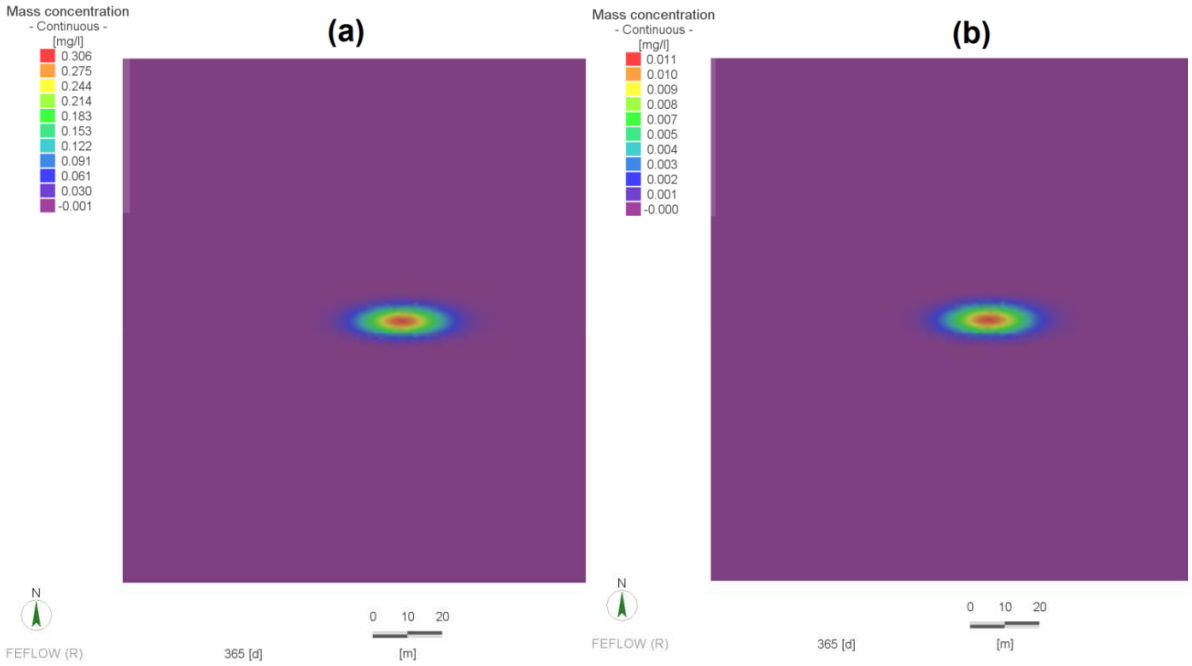

Figure 4.28. Effect of geothermal heating on benzene mass concentration at 30 mbgs (top view) after one year for (a) no heating (case C-5) and (b) variable sorption and biodegradation resulted from geothermal heating (case C-6)

Table 4.7. Summary of maximum concentration results for different benzene transport scenarios

Case	Maximum concentration ($mg.L^{-1}$)	Case description
C-1	0.554	Constant sorption, No biodegradation
C-2	0.472	Temperature-dependent sorption, No biodegradation
C-3	0.247	Constant sorption and biodegradation
C-4	0.011	Constant sorption, Temperature-dependent biodegradation
C-5	0.306	Constant sorption and biodegradation, No geothermal heating
C-6	0.11	Temperature-dependent sorption and biodegradation

For better comparison, the breakthrough curves for two cases of constant sorption and biodegradation at 10°C (case C-5) and temperature-dependent sorption and biodegradation parameters (case C-6) at a location 5 m far from benzene spill are plotted in Figure 4.29, after a one year period. The labels correlate with average ground temperature.

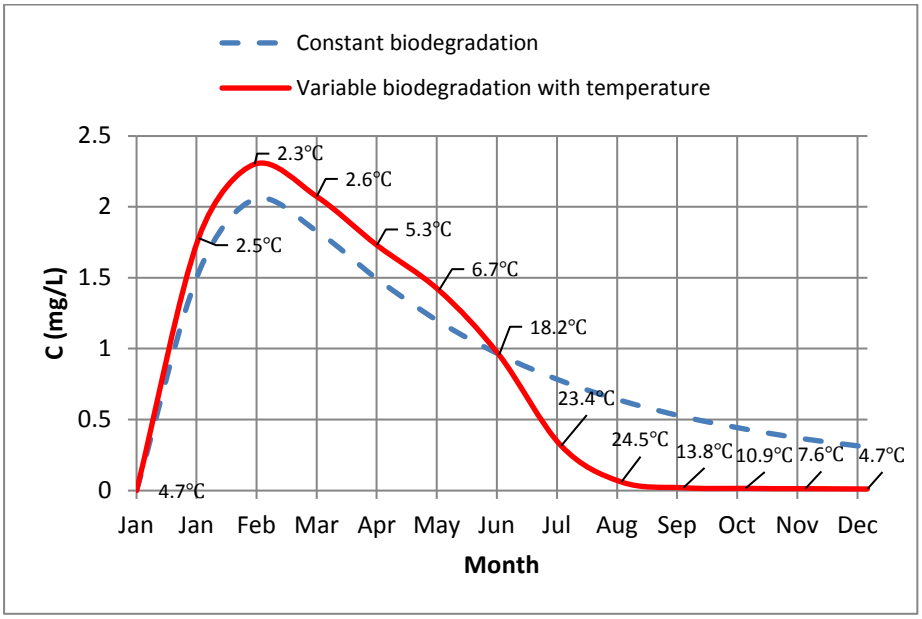

Figure 4.29. Breakthrough curves with constant and variable sorption and biodegradation rate at 5 m horizontal distance from the benzene spill

As seen in the graph, for the first 6 months (January to June) of geothermal operation, variable biodegradation assumption yields higher concentration of benzene which means less biodegradation is happening in the subsurface. This is due to the fact that during the first 5 months, ground temperature is less than 10°C owing to heating mode operation resulting in a lower biodegradation rate. During cooling mode, however, subsurface temperatures rise above 10°C and the biodegradation rate increases, leading to a substantial decline in concentration. The impact of higher temperatures on biodegradation is so significant that when the second heating cycle occurs and temperature drops again below 10°C in November and December, the decrease in microbial activity and biodegradation does not impact the concentration.

4.2.5. Impact of geothermal heating on toluene fate and transport with temperature-dependent sorption and biodegradation

Similar to benzene case, toluene spill is modeled with 100 mg.L^{-1} concentration at the depth of 28 to 32 mbgs and the model is solved with transient flow and mass transport assumptions. Figure 4.30 compares toluene mass concentration results after one year at 30 mbgs in top view for case C-7 with constant sorption and biodegradation parameters at of 10°C when no BHE is implemented and case C-8 with sorption and biodegradation parameters variable with temperature. Similar to simulations for benzene, the results show considerable increase in toluene disintegration when temperature-dependent biodegradation rates are employed. In this case, the maximum concentration after one year at constant temperature of 10°C which was 0.485 mg.L^{-1} has reduced to 0.037 mg.L^{-1} with inclusion of the temperature changes resulted from geothermal heat pump operation. Table 4.8 summarizes the maximum concentration results for toluene transport cases.

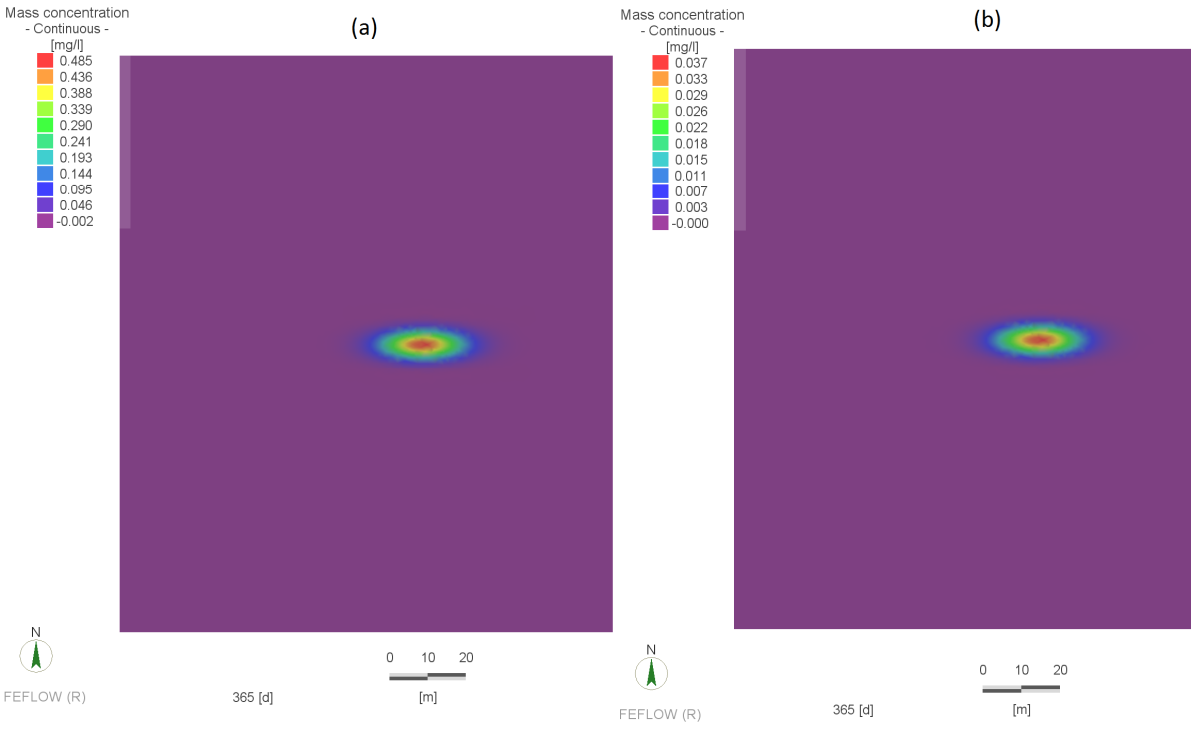

Figure 4.30. Effect of geothermal heating on toluene mass concentration at 30 mbgs after one year for (a) no heating (case C-7) and (b) variable sorption and biodegradation resulted from geothermal heating (case C-8)

Table 4.8. Summary of maximum concentration results for different toluene transport scenarios

Case	Maximum concentration ($mg.L^{-1}$)	Case description
C-7	0.485	Constant sorption and biodegradation, No geothermal heating
C-8	0.037	Temperature-dependent sorption and biodegradation

Again, breakthrough curves of toluene for two cases of constant sorption and biodegradation at 10°C without geothermal heating (case C-7) and temperature-dependent sorption and biodegradation parameters (case C-8) at a location 5 m far from spill are plotted in Figure 4.31 after one year of simulation. The results are similar to the benzene case demonstrating the impact of variable temperatures on biodegradation process. The labels correlate with average ground temperature.

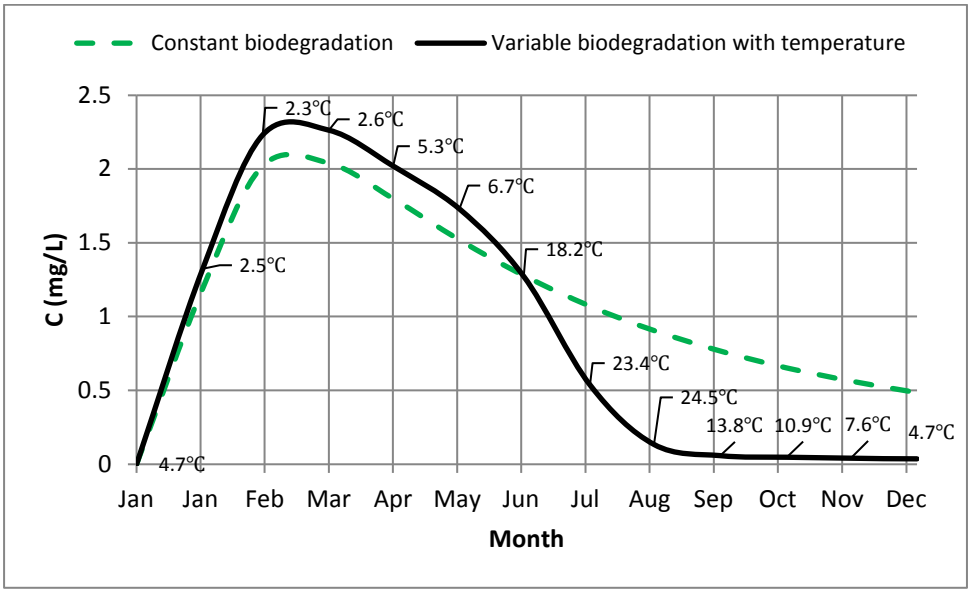

Figure 4.31. Breakthrough curves with constant and variable sorption and biodegradation rates at 5 m horizontal distance from the toluene spill

For better comparison, breakthrough curves for benzene and toluene are plotted in Figure 4.32 together. While benzene biodegrades relatively faster at constant temperature, the effectiveness

of high temperature on biodegradation rate is so significant that both benzene and toluene are significantly degraded after one year of BHE operation.

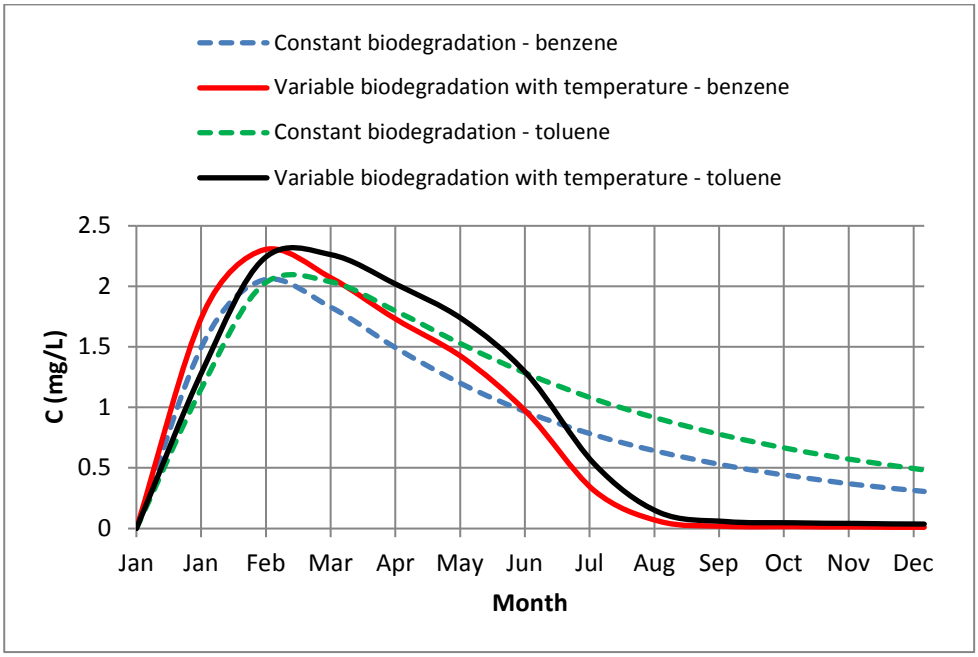

Figure 4.32. Comparison of breakthrough curves for benzene and toluene with constant and variable sorption and biodegradation rate at 5 m horizontal distance from the spill

4.2.6. Comparison of the required time for contaminant concentration reaching maximum allowable limit according to Canadian drinking water quality standards

In spite of substantial degradation for both benzene and toluene after one year of GSHP operation, reaching a concentration of 11 $\mu g.L^{-1}$ for benzene, compared to 37 $\mu g.L^{-1}$ for toluene, does not meet the Health Canada's requirements for benzene tolerance limit since maximum allowable concentrations for benzene and toluene in groundwater are 5 and 60 $\mu g.L^{-1}$, respectively (*Guidelines for Canadian Drinking Water Quality: Guideline Technical Document Benzene*, 2009; *Guidelines for Canadian Drinking Water Quality Guideline Technical Document Toluene, Ethylbenzene and Xylenes*, 2014).

Therefore, another benzene transport simulation with temperature-dependent sorption and biodegradation (case C-6) was performed with time extended to two years of GSHP operation. The results depicted in Figure 4.33 show that for adjusted case study, benzene concentration dropped below maximum allowable limit of 5 $\mu g.L^{-1}$ (*Guidelines for Canadian Drinking Water Quality: Guideline Technical Document Benzene*, 2009) after 607 days (20 months) while the time required for toluene to drop below maximum allowable limit of 60 $\mu g.L^{-1}$ (*Guidelines for Canadian Drinking Water Quality Guideline Technical Document Toluene, Ethylbenzene and Xylenes*, 2014) was 273 days (9 months).

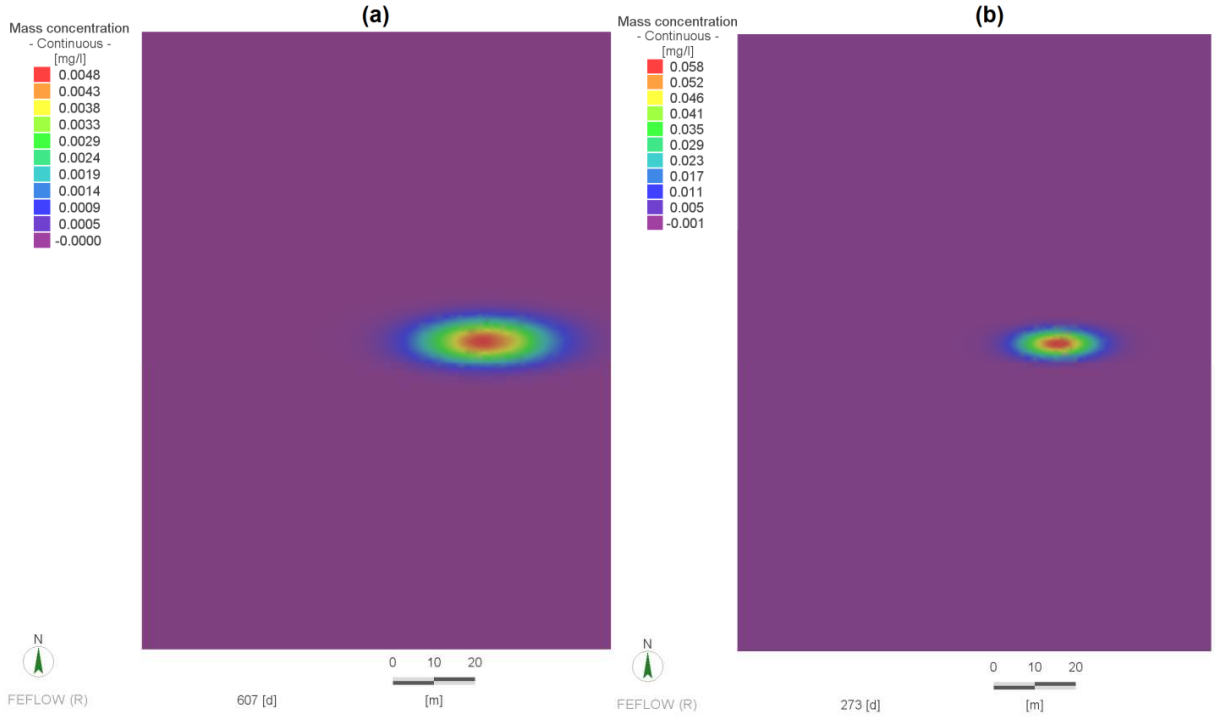

Figure 4.33. Comparison of time required for contaminant concentration reaching maximum allowable limit according to Canadian drinking water quality standards for (a) benzene (b) toluene

Chapter 5 - Summary and conclusion

Application of geothermal energy as an omnipresent source of thermal energy from the ground is a promising way to increase the use of renewable energy for space heating or cooling of buildings. Geothermal or ground source heat pumps are among the top growing energy technologies used for heating and cooling from shallow geothermal energy sources and have the ability to be widely implemented (Banks, 2012; Yuan et al., 2017). However, despite being commercially available for many years, little research has been performed on the environmental impacts of geothermal heat pumps, especially their potential for enhanced bioremediation. Therefore, evaluation of the effect of heat extracted or stored in the subsurface on groundwater flow and contaminant transport is valuable information in utilization and optimization of geothermal heating systems as a possible remediation strategy.

5.1. Summary

In this research, subsurface flow and transport simulations in the presence of a geothermal heat pump system are performed. The main objectives of this research, described in chapter 1, were as follows: (1) simulation, model validation and verification of a vertical closed-loop geothermal heat pump located in Canada using FEFLOW software, (2) study of long-term effects of geothermal heat pumps on ground temperature and development of thermal plumes in the subsurface, and (3) investigation of the impact of temperature changes resulting from geothermal heating on petroleum contaminants' fate and transport through temperature-dependent sorption and biodegradation.

Following a brief introduction and literature review on background studies in the first two chapters, a 3D numerical model in FEFLOW is developed, verified and validated in chapter 3 (objective 1). Objectives 2 and 3 are presented in chapter 4, with the simulation of different flow and transport scenarios. The simulations revealed the impact of heat transferred from a multiple BHE geothermal heat pump on groundwater flow through changes in fluid viscosity and density

and formation of buoyant flows around the boreholes. The resulting groundwater flow and heat transport also led to development of thermal plumes as the temperature anomalies within subsurface. For a case study of an office building in Toronto, a long-lasting increase in ground temperature is observed after 10 years of geothermal plant operation.

After investigation of changes in ground temperature, temperature-dependent sorption and biodegradation kinetics are employed in a coupled flow, heat and mass transport simulation to study the effect of heat from the BHE system on a hydrocarbon contaminant spill. The results reveal that the temperature changes caused by ground source heat pump's operation can significantly enhance biodegradation of Monoaromatic hydrocarbon contaminants.

5.2. Discussion and implications

The results of the flow and heat transport simulations with BHEs showed that a heated zone formed downstream of borefield during cooling cycle, lasting into subsequent heating seasons. Therefore, these simulations showed that a thermally affected zone can be formed even at the end of the first year of BHE operation. Moreover, thermally affected zone reached distances beyond 200 meters from the boreholes after 10 years of operation, with a moderate groundwater linear velocity of about 7.7 m/year. The extent and development of these heat (or cold) plumes, however, is dependent of the thermal load exerted from the building on the heat pump system as well as soil and groundwater conditions. Nonetheless, these simulations showed that for a typical 3-story building located in Toronto, significant thermal plumes could result from BHE operations. This study also showed that including temperature dependent density and viscosities is important to be able to accurately predict the extent of the thermal plume as well as the resulting groundwater velocities (magnitude and direction).

The result of contaminant transport simulations showed that even a cyclic subsurface temperature change in the range of 2 to 25°C could lead to a substantial increase in biodegradation rates compared to constant biodegradation (at 10°C), when no geothermal

heating is implemented. This in turn reveals the potential of geothermal heat pump systems as a promising bioremediation scheme. The impact of temperature on sorption, however, was insignificant compared to biodegradation parameters.

Despite the efforts to couple different fields of fluid dynamics, heat transfer, contaminant transport and biological science in this interdisciplinary study, there are still many uncertainties associated with this work:

1. Local temperature variation in the immediate vicinity of the BHEs is approximated by average subsurface temperature in the borefield area and used in the bioremediation study. This is due to the limitation of FEFLOW.
2. In case of high hydraulic conductivities, strong advective transport causes the contaminant mass to leave the borefield area in a short time. Therefore, calculation of sorption and biodegradation parameters based on average temperature of the borefield may be invalid.
3. Existence of co-contaminants in the subsurface might result in inhibitory effects on biodegradation of target hydrocarbons which is not considered by Monod kinetics, and therefore not included in this study.
4. Alteration from aerobic to anaerobic conditions in subsurface could lead to a decrease in biodegradation rates which is not considered in present research. Moreover, change in temperature can change redox potential, leading to different pathways in biodegradation process.
5. Biodegradation is a complex phenomenon with various parameters involved. Even with the existence of favorable microorganisms, oxygen level and temperatures, biodegradation did not occur in some real case studies in the past (Suarez & Rifai, 1999).

In addition to the results discussed in chapter 4 and summarized in this section, there are some implications from the simulation performed in this study as follows:

1. Results from different scenarios for flow and heat transport, showed that assuming constant viscosity or density in the simulation could lead to slight variation in temperature field. Nevertheless, the impact of temperature-dependent viscosity or density on Darcy velocity magnitude and flow direction (owing to formation of buoyant flows) is substantial. Therefore, assuming constant viscosity or density in the simulation of a geothermal heat pump system with coupled heat and contaminant transport attributes, could result in significant error in flow and mass concentration results.
2. Although the combination of steady-state flow with transient heat is considered as a transient transport simulation in FEFLOW, temperature and flow results might deviate significantly from the fully transient flow and heat transport simulation. Therefore, a realistic simulation calls for combining transient flow and transient heat transport simulation to achieve accurate temperature and flow results as well as to capture thermal plume impact.
3. Considering lifespan of a GSHP system as 20 to 25 years, formation of thermal plumes could lead to a vast thermally affected zone with hundreds of meters lengths. Therefore, it is imperative to perform careful design and analysis to avoid thermal interference with underground facilities.
4. In this study, the average ground temperature in the vicinity of the boreholes is derived in each month, to calculate the corresponding sorption and biodegradation coefficients in FEFLOW. Although this approach paves the way to model variable sorption and biodegradation with time and temperature, it neglects the temperature changes associated with location. Thereby, from the remediation perspective, it is only applicable to the contaminant source located close to the boreholes to achieve accurate contaminant concentration results.
5. Although the parameters used in this study were taken from the available literature to achieve a realistic analysis, real laboratory or field data is essential to ensure that the simulation results are completely valid, since biodegradation parameters are strongly site-specific.

6. Monod parameters used in the simulation were the lowest values available for aerobic biodegradation. Therefore, to the authors knowledge, the case study was representative of the worst-case scenario for remediation purpose. However, there might be different values associated with other cases in reality.
7. The results of present study revealed significant effect of variable temperature on biodegradation kinetics for Monoaromatic hydrocarbons thus endorsing the favorable impact of employing geothermal heat pumps for remediation purpose. However, it should be noted that variation in building thermal loads might affect the subsurface temperature and effectiveness of such systems.

5.3. Conclusion

This study aimed at understanding the effect of heat input on subsurface contaminants' fate and transport. The numerical modeling of flow, heat and mass transport within the ground was performed using the FEFLOW software based on the multiple borehole heat exchanger incorporated as a geothermal heat pump system. First, a transient temperature profile and thermal plume spread within the subsurface was obtained for a multiple borehole heat exchanger system. The resulting subsurface temperature redistribution from the geothermal heat pump operation was examined with respect to the impact on contaminants' fate and transport by affecting their dissolution rate, sorption characteristics and microorganism's population responsible for biodegradation. This temperature change was employed in contaminant transport simulation by means of temperature-dependent parameters associated with biodegradation kinetics to investigate the effect of geothermal heating system. Comparison of the contaminant transport results for variable and constant biodegradation kinetics showed remarkable impact of temperature-dependent biodegradation coefficient on treatment of hydrocarbon contaminants. It is also concluded that the potential of utilizing this temperature change within the subsurface for bioremediation purpose makes site-specific flow and transport simulations significantly valuable for employment of sustainable geothermal heat pump systems.

5.4. Suggested future work

Further studies and research areas are suggested as follows:

1. Combining numerical simulation with laboratory or field tests to ascertain the validity of the results and obtain parameters.
2. Examining the impact of different building load profiles from different climates on biodegradation of hydrocarbon contaminants.
3. Inclusion of variably saturated zone in flow and transport simulations.
4. Study the effect of more complex geologic characteristics such as anisotropy, heterogeneity or fractured rocks.
5. Development of FEFLOW software to add spatial changes in temperature-dependent sorption and biodegradation parameters to achieve better accuracy.
6. Study the impact of geothermal heating on more complex and persistent hydrocarbon contaminants and nonaqueous phase liquids such as chlorinated volatile organic compounds.
7. Study the impact of volatilization on fate and transport of BTEX compounds.

References

Alagappan, G., & Cowan, R. M. (2004). Effect of temperature and dissolved oxygen on the growth kinetics of Pseudomonas putida F1 growing on benzene and toluene. *Chemosphere*, *54*, 1255–1265. https://doi.org/10.1016/j.chemosphere.2003.09.013

Allaerts, K., Coomans, M., & Salenbien, R. (2015). Hybrid ground-source heat pump system with active air source regeneration. *Energy Conversion and Management*, *90*, 230–237. https://doi.org/10.1016/j.enconman.2014.11.009

Alvarez, P. J. J., Anid, P. J., & Vogel, T. M. (1991). Kinetics of aerobic biodegradation of benzene and toluene in sandy aquifer material. *Biodegradation*, *2*, 43–51. https://doi.org/https://doi.org/10.1007/BF00122424

Banks, D. (2012). *An introduction to thermogeology: Ground source heating and cooling: Second edition*. John Wiley & Sons, Ltd. https://doi.org/10.1002/9781118447512

Bekins, B. A., Warren, E., & Godsy, E. M. (1998). A Comparison of Zero-Order, First-Order, and Monod Biotransformation Models. *Groundwater*, *36*(2), 261–268. https://doi.org/https://doi.org/10.1111/j.1745-6584.1998.tb01091.x

Beyer, C., Popp, S., & Bauer, S. (2016). Simulation of temperature effects on groundwater flow , contaminant dissolution , transport and biodegradation due to shallow geothermal use. *Environmental Earth Sciences*, *75*(18), 1–20. https://doi.org/10.1007/s12665-016-5976-8

Bhatia, A. (2014). Heat Loss Calculations and Principles. In *HVAC Heating Load Calculations and Principles* (1st ed., p. 68). CreateSpace Independent Publishing Platform.

Blum, P., Campillo, G., & Kölbel, T. (2011). Techno-economic and spatial analysis of vertical ground source heat pump systems in Germany. *Energy*, *36*(5), 3002–3011. https://doi.org/10.1016/j.energy.2011.02.044

Bonte, M. (2013). *Impacts of shallow geothermal energy on groundwater quality, A hydrochemical and geomicrobial study of the effects of ground source heat pumps and*

aquifer thermal energy storage. [Vrije Universiteit]. http://www.hydrology-amsterdam.nl/personalpages/PhDs/Bonte_PhD_thesis_2013.pdf

Bonte, M., Röling, W. F. M., Zaura, E., Van Der Wielen, P. W. J. J., Stuyfzand, P. J., & Van Breukelen, B. M. (2013). Impacts of Shallow Geothermal Energy Production on Redox Processes and Microbial Communities. *Environmental Science & Technology*, *47*(24), 14476–14484.

Brons, H. J., Griffioen, J., Appelo, C. A. J., & Zehnder, A. J. B. (1991). Biogeochemical reactions in aquifer material from a thermal energy storage site. *Water Research*, *25*(6), 729–736. https://doi.org/https://doi.org/10.1016/0043-1354(91)90048-U

Canadian Climate Normals 1981-2010 Station Data. (2020). Environment Canada. https://climate.weather.gc.ca/climate_normals/results_1981_2010_e.html?searchType=stnName&txtStationName=toronto&searchMethod=contains&txtCentralLatMin=0&txtCentralLatSec=0&txtCentralLongMin=0&txtCentralLongSec=0&stnID=5097&dispBack=0

Chang, W., Whyte, L., & Ghoshal, S. (2011). Comparison of the effects of variable site temperatures and constant incubation temperatures on the biodegradation of petroleum hydrocarbons in pilot-scale experiments with field-aged contaminated soils from a cold regions site. *Chemosphere*, *82*(6), 872–878. https://doi.org/10.1016/j.chemosphere.2010.10.072

Cory, S., Lenoir, A., Donn, M., & Garde, F. (2011). Formulating a Building Climate Classification Method. *12th Conference of International Building Performance Simulation Association*, 14-16 November 2011.

Daemi, N. (2017). *Geothermal Systems Performance and Environmental Impacts* [York University]. http://hdl.handle.net/10315/34406

Daemi, N., & Krol, M. M. (2019). Impact of building thermal load on the developed thermal plumes of a multi-borehole GSHP system in different canadian climates. *Renewable*

Energy, *134*, 550–557. https://doi.org/10.1016/j.renene.2018.11.074

De Sousa, C., Ridsdale, R., Lima, I., & Easton., M. (2018). *THE STATE OF BROWNFIELDS IN CANADA - Renewing Canada's National Brownfield Redevelopment Strategy*. Canadian Brownfields Network. https://www.canadianbrownfieldsnetwork.ca/sites/default/uploads/files/The_State_of_Brownfields_in_Canada_final.pdf

Deeb, R. A., & Alvarez-cohen, L. (1999). Temperature Effects and Substrate Interactions During the Aerobic Biotransformation of BTEX Mixtures by Toluene-Enriched Consortia and Rhodococcus rhodochrous. *Biotechnology and Bioengineering*, *62*(5), 526–536. https://doi.org/https://doi.org/10.1002/(SICI)1097-0290(19990305)62:5<526::AID-BIT4>3.0.CO;2-8

Dehkordi, S. E., & Schincariol, R. A. (2014). Effect of thermal-hydrogeological and borehole heat exchanger properties on performance and impact of vertical closed-loop geothermal heat pump systems. *Hydrogeology Journal*, *22*, 189–203. https://doi.org/10.1007/s10040-013-1060-6

Dehkordi, S. E., Schincariol, R. A., & Olofsson, B. (2015). Impact of Groundwater Flow and Energy Load on Multiple Borehole Heat Exchangers. *Groundwater*, *53*(4), 558–571. https://doi.org/10.1111/gwat.12256

Determining the fraction of organic carbon (foc) for methods three and four. (2017). Alaska Department of Environmental Conservation (ADEC). https://www.google.com/url?sa=t&rct=j&q=&esrc=s&source=web&cd=&cad=rja&uact=8&ved=2ahUKEwjCuo-cxaPqAhWIlHIEHZzBDTkQFjAAegQIARAB&url=https%3A%2F%2Fdec.alaska.gov%2Fmedia%2F11930%2Fdetermining-the-fraction-of-organic-carbon2017.pdf&usg=AOvVaw3bl8KcKI_qGFv9askpTS9W

Diao, N., Li, Q., & Fang, Z. (2004). Heat transfer in ground heat exchangers with groundwater

advection. *International Journal of Thermal Sciences*, *43*(12), 1203–1211. https://doi.org/10.1016/j.ijthermalsci.2004.04.009

Diersch, H. J. G. (2009a). *FEFLOW - Finite Element Subsurface Flow and Transport Simulation Systems - White Papers Volume 1* (1st ed.). DHI-WASY GmbH.

Diersch, H. J. G. (2009b). *FEFLOW - Finite Element Subsurface Flow and Transport Simulation Systems - White Papers Volume 4* (1st ed.). DHI-WASY GmbH.

Diersch, H. J. G. (2014). *FEFLOW: Finite Element Modeling of Flow, Mass and Heat Transport in Porous and Fractured Media* (1st ed.). Springer Berlin Heidelberg. https://doi.org/10.1007/978-3-642-38739-5

Diersch, H. J. G., Bauer, D., Heidemann, W., Ruhaak, W., & Schatzl, P. (2011a). Finite element modeling of borehole heat exchanger systems Part 1 . Fundamentals. *Computers & Geosciences*, *37*, 1122–1135. https://doi.org/10.1016/j.cageo.2010.08.003

Diersch, H. J. G., Bauer, D., Heidemann, W., Ruhaak, W., & Schatzl, P. (2011b). Finite element modeling of borehole heat exchanger systems Part 2 . Numerical simulation. *Computers & Geosciences*, *37*, 1136–1147. https://doi.org/10.1016/j.cageo.2010.08.002

Diersch, H. J. G., Bauer, D., Heidemann, W., Rühaak, W., & Schätzl, P. (2010). *FEFLOW - Finite Element Subsurface Flow and Transport Simulation Systems - White Papers Volume 5* (1st ed.). DHI-WASY GmbH.

Domenico, P., & Schwartz, F. (1997). *Physical and chemical hydrogeology* (2nd ed.). John Wiley & Sons, Ltd.

Donaldson, R., & Lord, R. (2018). Can brownfield land be reused for ground source heating to alleviate fuel poverty? *Renewable Energy*, *116*, 344–355. https://doi.org/https://doi.org/10.1016/j.renene.2017.09.037

Doran, P. M. (2013). *Bioprocess Engineering Principles* (2nd ed.). Academic Press. https://doi.org/https://doi.org/10.1016/C2009-0-22348-8

El-naas, M. H., Acio, J. A., & Telib, A. E. El. (2014). Aerobic biodegradation of BTEX : Progresses and Prospects. *Journal of Environmental Chemical Engineering*, *2*(2), 1104–1122. https://doi.org/10.1016/j.jece.2014.04.009

EPA On-line Tools for Site Assessment Calculation - Diffusion Coefficient. (2020). U. S. Environmental Protection Agency. https://www3.epa.gov/ceampubl/learn2model/part-two/onsite/estdiffusion.html

FEFLOW 7.1 documentation. (2020). DHI Group. http://www.feflow.info/html/help71/feflow/mainpage.htm#t=02_News%2Fnews.html

Ferguson, G., & Woodbury, A. D. (2006). Observed thermal pollution and post-development simulations of low-temperature geothermal systems in Winnipeg , Canada. *Hydrogeology Journal*, *14*, 1206–1215. https://doi.org/10.1007/s10040-006-0047-y

Fetter, C. W. (2008). *Contaminant Hydrogeology* (2nd ed.). Waveland Press, Inc.

Finizio, A., & Guardo, A. Di. (2001). Estimating temperature dependence of solubility and octanol-water partition coefficient for organic compounds using RP-HPLC. *Chemosphere*, *45*, 1063–1070. https://doi.org/https://doi.org/10.1016/S0045-6535(01)00105-9

Ghoreishi-madiseh, S. A., Kuyuk, A. F., Antonio, M., & Brito, R. De. (2019). An analytical model for transient heat transfer in ground-coupled heat exchangers of closed-loop geothermal systems. *Applied Thermal Engineering*, *150*, 696–705. https://doi.org/10.1016/j.applthermaleng.2019.01.020

Guidelines for Canadian Drinking Water Quality: Guideline Technical Document Benzene. (2009). Health Canada. https://www.canada.ca/en/health-canada/services/publications/healthy-living/guidelines-canadian-drinking-water-quality-guideline-technical-document-benzene.html

Guidelines for Canadian Drinking Water Quality Guideline Technical Document Toluene, Ethylbenzene and Xylenes. (2014). Health Canada. https://www.canada.ca/en/health-

canada/services/publications/healthy-living/guidelines-canadian-drinking-water-quality-toluene-ethylbenzene-xylenes.html

Hähnlein, S., Bayer, P., Ferguson, G., & Blum, P. (2013). Sustainability and policy for the thermal use of shallow geothermal energy. *Energy Policy*, *59*, 914–925. https://doi.org/10.1016/j.enpol.2013.04.040

Hecht-Mendez, J., Molina-Giraldo, N., Blum, P., & Bayer, P. (2010). Evaluating MT3DMS for Heat Transport Simulation of Closed Geothermal Systems. *Ground Water*, *48*(5), 741–756. https://doi.org/10.1111/j.1745-6584.2010.00678.x

Hecht-méndez, J., Paly, M. De, Beck, M., & Bayer, P. (2013). Optimization of energy extraction for vertical closed-loop geothermal systems considering groundwater flow. *Energy Conversion and Management*, *66*, 1–10. https://doi.org/10.1016/j.enconman.2012.09.019

Hein, P., Kolditz, O., Görke, U., Bucher, A., & Shao, H. (2016). A numerical study on the sustainability and efficiency of borehole heat exchanger coupled ground source heat pump systems. *Applied Thermal Engineering*, *100*, 421–433. https://doi.org/10.1016/j.applthermaleng.2016.02.039

Hiller, E., Jurkovič, Ľ., & Bartaľ, M. (2008). Effect of Temperature on the Distribution of Polycyclic Aromatic Hydrocarbons in Soil and Sediment. *Soil and Water Research*, *3*(4), 231–240. https://doi.org/https://doi.org/10.17221/28/2008-SWR

How To Evaluate Alternative Cleanup Technologies For Underground Storage Tank Sites. (2004). U.S. Environmental Protection Agency. https://www.epa.gov/ust/how-evaluate-alternative-cleanup-technologies-underground-storage-tank-sites-guide-corrective

Jesußek, A., Grandel, S., & Dahmke, A. (2013). Impacts of subsurface heat storage on aquifer hydrogeochemistry. *Environmental Earth Sciences*, *69*, 1999–2012. https://doi.org/10.1007/s12665-012-2037-9

Junfeng, D. O. U., Xiang, L. I. U., & Zhifeng, H. U. (2008). Anaerobic BTEX degradation in soil

bioaugmented with mixed consortia under nitrate reducing conditions. *Journal of Environmental Sciences*, *20*, 585–592. https://doi.org/https://doi.org/10.1016/S1001-0742(08)62098-7

Khodaei, K., Reza, H., Mazaheri, M., Mohammadzadeh, H., & Mahmoodlu, M. G. (2017). BTEX biodegradation in contaminated groundwater using a novel strain (Pseudomonas sp. BTEX-30). *International Biodeterioration & Biodegradation*, *116*, 234–242. https://doi.org/10.1016/j.ibiod.2016.11.001

Klotzbucher, T., Kappler, A., Straub, K. L., & Haderlein, S. B. (2007). Biodegradability and groundwater pollutant potential of organic anti-freeze liquids used in borehole heat exchangers. *Geothermics*, *36*, 348–361. https://doi.org/10.1016/j.geothermics.2007.03.005

Koohi-Fayegh, S., & Rosen, M. A. (2014). An analytical approach to evaluating the effect of thermal interaction of geothermal heat exchangers on ground heat pump efficiency. *Energy Conversion and Management*, *78*, 184–192. https://doi.org/10.1016/j.enconman.2013.09.064

Krol, M. M., Johnson, R. L., & Sleep, B. E. (2014). An analysis of a mixed convection associated with thermal heating in contaminated porous media. *Science of the Total Environment, The*, *499*, 7–17. https://doi.org/10.1016/j.scitotenv.2014.08.028

Krol, M. M., Mumford, K. G., Johnson, R. L., & Sleep, B. E. (2011). Modeling discrete gas bubble formation and mobilization during subsurface heating of contaminated zones. *Advances in Water Resources*, *34*(4), 537–549. https://doi.org/10.1016/j.advwatres.2011.01.010

Krol, M. M., Sleep, B. E., & Johnson, R. L. (2011). Impact of low-temperature electrical resistance heating on subsurface. *Water Resources Research*, *47*(5), 1–12. https://doi.org/10.1029/2010WR009675

Lee, E. Y., Jun, Y. S., Cho, K., & Ryu, H. W. (2002). Degradation Characteristics of Toluene ,

Benzene , Ethylbenzene , and Xylene by Stenotrophomonas maltophilia T3-c. *Journal of the Air & Waste Management Association*, *52*(4), 400–406. https://doi.org/10.1080/10473289.2002.10470796

Lee, J. S., Song, K. S., Ahn, J. H., & Kim, Y. (2015). Comparison on the transient cooling performances of hybrid ground- source heat pumps with various fl ow loop con fi gurations. *Energy*, *82*, 678–685. https://doi.org/10.1016/j.energy.2015.01.076

Li, H., Liu, Y. H., Luo, N., Zhang, X. Y., Luan, T. G., Hu, J. M., & Wang, Z. Y. (2006). Biodegradation of benzene and its derivatives by a psychrotolerant and moderately haloalkaliphilic Planococcus sp . strain ZD22. *Research in Microbiology*, *157*, 629–636. https://doi.org/10.1016/j.resmic.2006.01.002

Li, M., & Lai, A. C. K. (2015). Review of analytical models for heat transfer by vertical ground heat exchangers (GHEs): A perspective of time and space scales. *Applied Energy*, *151*, 178–191. https://doi.org/10.1016/j.apenergy.2015.04.070

Li, Weiyi, Lin, X., Cao, C., Gong, Z., & Gao, Y. (2018). Organic Rankine Cycle-assisted ground source heat pump combisystem for space heating in cold regions. *Energy Conversion and Management*, *165*, 195–205. https://doi.org/https://doi.org/10.1016/j.enconman.2018.03.062

Li, Wenxin, Li, X., Wang, Y., Du, R., & Tu, J. (2019). Effect of the heat load distribution on thermal performance predictions of ground heat exchangers in a stratified subsurface. *Renewable Energy*, *141*, 340–348. https://doi.org/10.1016/j.renene.2019.04.025

Littlejohns, J. V, & Daugulis, A. J. (2008). Kinetics and interactions of BTEX compounds during degradation by a bacterial consortium. *Process Biochemistry*, *43*, 1068–1076. https://doi.org/10.1016/j.procbio.2008.05.010

Logeshwaran, P., Megharaj, M., Sreenivasulu, C., Bowman, M., & Naidu, R. (2018). Petroleum hydrocarbons (PH) in groundwater aquifers : An overview of environmental fate, toxicity,

microbial degradation and risk-based remediation approaches. *Environmental Technology & Innovation*, *10*, 175–193. https://doi.org/10.1016/j.eti.2018.02.001

Lucia, U., Simonetti, M., Chiesa, G., & Grisolia, G. (2017). Ground-source pump system for heating and cooling: Review and thermodynamic approach. *Renewable and Sustainable Energy Reviews*, *70*, 867–874. https://doi.org/10.1016/j.rser.2016.11.268

Lund, J. W., & Boyd, T. L. (2016). Direct utilization of geothermal energy 2015 worldwide review. *Geothermics*, *60*, 66–93. https://doi.org/10.1016/j.geothermics.2015.11.004

Luo, J., Rohn, J., Bayer, M., Priess, A., Wilkmann, L., & Xiang, W. (2015). Heating and cooling performance analysis of a ground source heat pump system in Southern Germany. *Geothermics*, *53*, 57–66. https://doi.org/10.1016/j.geothermics.2014.04.004

Luo, J., Rohn, J., Xiang, W., Bertermann, D., & Blum, P. (2016). A review of ground investigations for ground source heat pump (GSHP) systems. *Energy and Buildings*, *117*, 160–175. https://doi.org/10.1016/j.enbuild.2016.02.038

Majorowicz, J., Grasby, S. E., & Skinner, W. R. (2009). Estimation of Shallow Geothermal Energy Resource in Canada : Heat Gain and Heat Sink. *Natural Resources Research*, *18*(2), 95–108. https://doi.org/10.1007/s11053-009-9090-4

Mensah, K., Jang, Y., & Choi, J. M. (2017). Assessment of design strategies in a ground source heat pump system. *Energy & Buildings*, *138*, 301–308. https://doi.org/10.1016/j.enbuild.2016.12.055

Moradi, A., Smits, K. M., & Sharp, J. O. (2018). Coupled Thermally-Enhanced Bioremediation and Renewable Energy Storage System: Conceptual Framework and Modeling Investigation. *Water*, *10*(10), 1288. https://doi.org/10.3390/w10101288

National Research Council - In Situ Bioremediation: When Does it Work? (1993). The National Academies Press. https://doi.org/10.17226/2131

Ngueleu, S. K., Rezanezhad, F., Al-raoush, R. I., & Cappellen, P. Van. (2018). Sorption of benzene

and naphthalene on (semi) -arid coastal soil as a function of salinity and temperature. *Journal of Contaminant Hydrology*, *219*, 61–71. https://doi.org/10.1016/j.jconhyd.2018.11.001

Omer, A. M. (2013). Direct expansion ground source heat pumps for heating and cooling. *International Research Journal on Engineering*, *1*(2), 27–48. http://www.apexjournal.org

Ozudogru, T. Y., Olgun, C. G., & Senol, A. (2014). 3D numerical modeling of vertical geothermal heat exchangers. *Geothermics*, *51*, 312–324. https://doi.org/10.1016/j.geothermics.2014.02.005

Parker, N., Schneegurt, M., Thi Tu, A.-H., Lister, P., & Forster, B. M. (2016). *Microbiology* (1st ed.). OpenStax Press. https://openstax.org/details/books/microbiology

Pophillat, W., Attard, G., Bayer, P., & Hecht-m, J. (2020). Analytical solutions for predicting thermal plumes of groundwater heat pump systems. *Renewable Energy*, *147*, 2696–2707. https://doi.org/10.1016/j.renene.2018.07.148

Powers, S. E., Hunt, C. S., Heermann, S. E., Corseuil, X., Rice, D., & Alvarez, P. J. J. (2001). The Transport and Fate of Ethanol and BTEX in Groundwater Contaminated by Gasohol. *Critical Reviews in Environmental Science and Technology*, *31*(1), 79–123. https://doi.org/https://doi.org/10.1080/20016491089181

Raymond, J., Therrien, R., & Gosselin, L. (2010). Low-temperature geothermal energy in mining environments. *CIM Journal*, *1*(2), 140–149.

Reardon, K. F., Mosteller, D. C., & Rogers, J. D. B. (2000). Biodegradation Kinetics of Benzene , Toluene , and Phenol as Single and Mixed Substrates for Pseudomonas putida F1. *BIOTECHNOLOGY AND BIOENGINEERING, 69*(4), 385–400. https://doi.org/https://doi.org/10.1002/1097-0290(20000820)69:4<385::AID-BIT5>3.0.CO;2-Q

Reddy, L. N., & Inyang, H. I. (2000). *Geoenvironmental Engineering: Principles and Applications*

(1st ed.). CRC Press.

Rees, S. J. (2016). *Advances in Ground-Source Heat Pump Systems* (1st ed.). Woodhead Publishing.

Remodeling calculator. (2020). On-Line Source. https://www.remodelingcalculator.org/geothermal-heating-cooling-costs/

Sagia, Z., Rakopoulos, C., & Kakaras, E. (2012). Cooling dominated Hybrid Ground Source Heat Pump System application. *Applied Energy*, *94*, 41–47. https://doi.org/10.1016/j.apenergy.2012.01.031

Saito, T., Hamamoto, S., Ueki, T., Ohkubo, S., Moldrup, P., Kawamoto, K., & Komatsu, T. (2017). Temperature change affected groundwater quality in a confined marine aquifer during long-term heating and cooling. *Water Research*, *94*(2016), 120–127. https://doi.org/10.1016/j.watres.2016.01.043

Schelenz, S., Vienken, T., Shao, H., Firmbach, L., & Dietrich, P. (2017). On the importance of a coordinated site characterization for the sustainable intensive thermal use of the shallow subsurface in urban areas : a case study. *Environmental Earth Sciences*, *76*(2), 1–15. https://doi.org/10.1007/s12665-016-6331-9

Self, S. J., Reddy, B. V., & Rosen, M. A. (2013). Geothermal heat pump systems: Status review and comparison with other heating options. *Applied Energy*, *101*, 341–348. https://doi.org/10.1016/j.apenergy.2012.01.048

Si-zhong, Y., Hui-jun, J. I. N., Zhi, W. E. I., Rui-xia, H. E., Yan-jun, J. I., & Xiu-mei, L. I. (2009). Bioremediation of Oil Spills in Cold Environments : A Review. *Pedosphere: An International Journal*, *19*(3), 371–381. https://doi.org/10.1016/S1002-0160(09)60128-4

Sleep, B. E., & Mcclure, P. D. (2001). The effect of temperature on adsorption of organic compounds to soils. *Canadian Geotechnical Journal*, *38*(1), 46–52. https://doi.org/10.1139/cgj-38-1-46

Soltani, M., Kashkooli, F. M., Dehghani-Sanij, A. R., Kazemi, A. R., Bordbar, N., Farshchi, M. J., Elmi, M., Gharali, K., & Dusseault, M. B. (2019). A comprehensive study of geothermal heating and cooling systems. *Sustainable Cities and Society*, *44*, 793–818. https://doi.org/10.1016/j.scs.2018.09.036

Sommer, W., Drijver, B., Verburg, R., Slenders, H., Vries, E. De, Leusbrock, I., & Grotenhuis, T. (2013). Combining shallow geothermal energy and groundwater remediation. *European Geothermal Congress*, *3-7 June*.

Staffell, I., Brett, D., Brandon, N., & Hawkes, A. (2012). A review of domestic heat pumps. *Energy & Environmental Science*, *5*(11), 9291–9306. https://doi.org/10.1039/C2EE22653G

Stempvoort, D. Van, & Biggar, K. (2008). Potential for bioremediation of petroleum hydrocarbons in groundwater under cold climate conditions : A review. *Cold Regions Science and Technology*, *53*, 16–41. https://doi.org/10.1016/j.coldregions.2007.06.009

Suarez, M. P., & Rifai, H. S. (1999). Biodegradation Rates for Fuel Hydrocarbons and Chlorinated Solvents in Groundwater. *Bioremediation Journal*, *3*(4), 337–362. https://doi.org/https://doi.org/10.1080/10889869991219433

The Engineering ToolBox - Volumetric or Cubic Thermal Expansion. (2020). https://www.engineeringtoolbox.com/volumetric-temperature-expansion-d_315.html

The Enginnering Toolbox - Specific Heat of some common Substances. (2020). https://www.engineeringtoolbox.com/specific-heat-capacity-d_391.html

The Enginnering Toolbox - Water - Thermal Conductivity. (2020). https://www.engineeringtoolbox.com/water-liquid-gas-thermal-conductivity-temperature-pressure-d_2012.html

Tolooiyan, A., & Hemmingway, P. (2014). A preliminary study of the effect of groundwater flow on the thermal front created by borehole heat exchangers. *International Journal of Low-Carbon Technologies*, *9*, 284–295. https://doi.org/10.1093/ijlct/cts077

Wang, Y., Qin, C., & Witarsa, F. (2018). Clarifying configurations of reaction rate constant for first-order and Monod-type kinetics : A comparative manner and a pursuit of parametric definition. *Waste Management*, *77*, 22–29. https://doi.org/10.1016/j.wasman.2018.04.040

Yang, H., Cui, P., & Fang, Z. (2010). Vertical-borehole ground-coupled heat pumps : A review of models and systems. *Applied Energy*, *87*(1), 16–27. https://doi.org/10.1016/j.apenergy.2009.04.038

Yuan, T., Ding, Y., Zhang, Q., Zhu, N., Yang, K., & He, Q. (2017). Thermodynamic and economic analysis for ground-source heat pump system coupled with borehole free cooling. *Energy and Buildings*, *155*, 185–197. https://doi.org/10.1016/j.enbuild.2017.09.018